THE UNIVERSITY OF CHICAGO

SEARCHES FOR NEUTRAL HIGGS BOSONS IN $q\bar{q}\tau^+\tau^-$ FINAL STATES USING THE OPAL DETECTOR AT LEP

A DISSERTATION SUBMITTED TO
THE FACULTY OF THE DIVISION OF THE PHYSICAL SCIENCES
IN CANDIDACY FOR THE DEGREE OF
DOCTOR OF PHILOSOPHY

DEPARTMENT OF PHYSICS

BY
JAMES ANDREW HOCKER

CHICAGO, ILLINOIS
DECEMBER 2000

ABSTRACT

Searches for neutral Higgs bosons have been performed with the OPAL detector at LEP. Approximately 170 pb^{-1} of $\mathrm{e}^+\mathrm{e}^-$ collision data at $\sqrt{s} \approx 189$ GeV have been used to search for the SM process $\mathrm{e}^+\mathrm{e}^- \to \mathrm{H}^0\mathrm{Z}^0$ as well as for the processes $\mathrm{e}^+\mathrm{e}^- \to \mathrm{h}^0\mathrm{Z}^0$ and $\mathrm{e}^+\mathrm{e}^- \to \mathrm{h}^0\mathrm{A}^0$ which occur in extended Higgs theories. The searches are sensitive to final states containing quarks and tau leptons, for which an artificial neural network for the identification of tau leptons was designed. The results have been combined with OPAL searches for other final states to obtain a 95% confidence level lower limit on the SM Higgs boson mass of 91.0 GeV/c^2. In a constrained MSSM scenario, the limits $m_{\mathrm{h}} > 74.8$ GeV/c^2 and $m_{\mathrm{A}} > 76.5$ GeV/c^2 are obtained at 95% CL assuming $\tan\beta > 1$, and values of $\tan\beta$ between 0.72 and 2.19 are excluded at 95% CL for the case of zero scalar top mixing. The parameter spaces of the MSSM and general Type II Two Higgs Doublet Models are explored in detailed scans, and in addition, limits on the production of Higgs-like bosons outside the context of specific models are obtained.

ACKNOWLEDGEMENTS

Where to begin? I am indebted to many, many people for providing me with a rewarding graduate school experience, but none more so than my advisor, Mark Oreglia. I believe it was a unique opportunity to work with someone who at the same time was carrying out his own Higgs research, as he proved an invaluable source of expertise. I am also grateful for his encouragement, camaraderie, and the careful tabs he kept on my work as it progressed.

It was also my privilege to work very closely with Doug Glenzinski, who provided excellent guidance and criticism every step of the way as the research progressed. The amount of work that he did to help make the present analysis one of the highest quality cannot be overstated.

The Chicago OPAL group in its many incarnations always seems to be an incredible pool of talent, and I have learned a great deal from Hal Evans, André Turcot, Alain Bellerive, Robin Coxe, Eric Torrence, Richard Teuscher, and Frank Merritt. I especially want to thank Jim Pilcher and Kelby Anderson for the opportunity to do some work with the ATLAS TileCal electronics, and for their accepting many a panicky transatlantic phone call as I was learning my way around the system.

It was an unforgettable experience working with the lively (if sleep-deprived) OPAL Higgs group. I am grateful for all the hard work done by Sijbrand de Jong, Klaus Desch, Satoru "URGENT!" Yamashita, Tom Junk, Gail Hanson, Peter Bock, Peter Igo-Kemenes, Markus Schumacher, Thorsten Kuhl, Amit Klier, Anthony Faust, Arnulf Quadt, Jenny Böhme, Pamela Ferrari, and Daniel Zer-Zion. I especially want to thank Isamu Nakamura, whose initial studies of the Higgs tau channel provided an excellent starting point for my research, and who has provided many invaluable services to the Higgs group over the years.

The entire OPAL collaboration has earned my gratitude and admiration for building and running a great detector, and talking shop over lunch and/or coffee with

some of them proved to be enjoyable and educational. I especially want to thank OPAL's über-secretary Mette Stuwe for her countless services as a translator, ski guide, bureaucracy-smasher, and general crisis-resolver.

On a different note, I thank everyone in the Geneva Softball League for giving me something to do with my summers. Our Sunday afternoon games, barbecues, booze-ups, and trips to Lyon are among my fondest memories of my time abroad. Maximum respect goes out to Jim Loftis and Ali Banki for good times spent in Geneva's Irish pubs, nightclubs, and movie theaters.

Finally, I wish to thank my parents Jim and Joan and my sister Jennifer for their unlimited love and support during my graduate school years and all the ones preceding.

TABLE OF CONTENTS

APPENDICES

LIST OF FIGURES

LIST OF TABLES

CHAPTER 1
INTRODUCTION

One of the Standard Model's greatest success stories has been the unification of the electromagnetic force and weak nuclear force within the framework of one underlying gauge theory. It is actually quite remarkable that the interactions describing such apparently unrelated phenomena (for example, the electromagnetic process of a traveling light wave and the weak process of nuclear β-decay) can be realized as different manifestations of one overall "electroweak" interaction. Yet James Clerk Maxwell's unified picture of the electromagnetic force accomplished the same thing in 1883, providing a connection between the seemingly disparate worlds of electric currents and bar magnets. In fact, unification of forces is such a beloved concept that many feel that electroweak unification is just the next step in the process begun by Maxwell, and that eventually we will be able to also incorporate the strong nuclear force, and possibly even gravity, into some Grand Unified Theory, or "GUT."

However, like all the best theories, electroweak theory contains more than just aesthetic and theoretical appeal; it is also borne out by experiment. At the time of its introduction it predicted new interactions (weak neutral currents) which were subsequently observed. It predicted new particles (the $W^{\pm}$ and Z^0 bosons) with enormous (for the time) masses, which were eventually found. In recent years, all its accessible predictions have been scrutinized by experiment (with sometimes ruthless precision) and it has shown itself to be entirely self-consistent.

There is, however, one ingredient still missing in this theory, and that ingredient is the mechanism by which the electroweak symmetry is broken. This thesis presents an attempt to fill in this fundamental gap via a search for a Higgs boson, the existence of which is a consequence of the spontaneously broken symmetry. In this chapter, the theoretical underpinnings of several types of Higgs mechanisms will be described, so as to motivate the experimental approaches taken in the remainder of the thesis.

1.1 The GWS Electroweak Theory

By the 1940s, electromagnetism already had a successful relativistic formulation in the language of quantized fields, known as quantum electrodynamics (QED). QED describes electromagnetic interactions via the coupling of a massless vector field A_μ (identified with the photon) to electric charge e. By contrast, Fermi's original theory of the weak β-decay process was a point-like four-fermion interaction characterized by a coupling constant G_F (the Fermi constant). This could be viewed as the interaction of the charged vector currents $\bar{p}(x)\gamma_\mu n(x)$ and $\bar{e}(x)\gamma_\nu \nu(x)$. As more weak processes were studied and phenomena such as parity violation became evident, the "$V-A$" theory became the paradigmatic weak interaction model; here the interactions of fermion fields are described by a current $\bar{\psi}(x)\gamma_\mu(c_V+c_A\gamma_5)\psi(x)$ (in the case of electron and neutrino fields, $c_V = 1$ and $c_A = -1$).

Although the $V-A$ theory provided a framework within which observable weak processes could be adequately described, it was clear that it was incomplete. It suffered from badly divergent high-energy behavior, predicting, for example, neutrino scattering cross sections that violated unitarity limits. The solution for the systematic cancelling of these divergences came from the work of Glashow, Weinberg, and Salam in the 1960s [1, 2, 3], which provided the unified electroweak model which stands today.

1.1.1 GWS Basics

In the GWS theory, the gauge bosons come in a SU(2) isovector triplet ($\mathbf{W}_\mu$, three components) coupling to weak isospin T, and a U(1) isosinglet B_μ coupling to weak hypercharge Y, defined as $Y = Q - T^3$ where Q is the electric charge and T^3 is the third component of weak isospin. The Standard Model fermions (see Table 1.1) are assigned to weak isodoublets ($T = 1/2$) and isosinglets ($T = 0$):

$$\begin{pmatrix} \nu_L \\ \mathrm{e}_L \end{pmatrix}, \begin{pmatrix} \mathrm{e}_R \end{pmatrix}, \begin{pmatrix} \mathrm{u}_L \\ \mathrm{d}_L \end{pmatrix}, \begin{pmatrix} \mathrm{u}_R \end{pmatrix}, \begin{pmatrix} \mathrm{d}_R \end{pmatrix}$$

	Generation		
Quarks	u	c	t
	d	s	b
Leptons	ν_{e}	ν_μ	ν_τ
	e^-	μ^-	τ^-
Gauge bosons	γ, Z^0, $\mathrm{W}^\pm$, g		

Table 1.1: The Standard Model particles.

where the upper (lower) component of the doublet has $T^3 = +1/2$ $(-1/2)$. The isospin assignments for the second- and third-generation fermions are identical.

The interaction Lagrangian density is

$$\mathcal{L} = g\mathbf{J}_\mu \cdot \mathbf{W}_\mu + g' J^Y_\mu B_\mu \tag{1.1}$$

where $\mathbf{J}_\mu$ and J^Y_μ are the isospin and hypercharge currents of the fermions. From the definition of hypercharge J^Y_μ can be written as $J^{\mathrm{EM}}_\mu - J^3_\mu$, where J^{EM}_μ is the electromagnetic current.

The physical bosons of the theory are constructed by creating the isospin raising and lowering operators from W^1_μ and W^2_μ,

$$W^\pm_\mu = (W^1_\mu \pm iW^2_\mu)/\sqrt{2} \tag{1.2}$$

and two orthogonal states from W^3_μ and B_μ,

$$Z_\mu = W^3_\mu \cos\theta_W - B_\mu \sin\theta_W \tag{1.3}$$

$$A_\mu = W^3_\mu \sin\theta_W + B_\mu \cos\theta_W \tag{1.4}$$

where $g'/g = \tan\theta_W$. Rewriting Equation 1.1 in terms of these bosons gives

$$\mathcal{L} = \frac{g}{\sqrt{2}}(J^-_\mu W^+_\mu + J^+_\mu W^-_\mu) + \frac{g}{\cos\theta_W}(J^3_\mu - \sin^2\theta_W J^{\mathrm{EM}}_\mu)Z_\mu + g\sin\theta_W J^{\mathrm{EM}}_\mu A_\mu \tag{1.5}$$

where $J_\mu^\pm = J_\mu^1 \pm J_\mu^2$. Note that the last term in Equation 1.5 is the familiar photon coupling to an electromagnetic current, allowing the identification of $g \sin\theta_W$ with e. Writing out the currents explicitly,

$$J_\mu^\pm = \bar{\psi}_L \gamma_\mu \sigma^\pm \psi_L \tag{1.6}$$

$$J_\mu^3 = \bar{\psi}_L \gamma_\mu \sigma^3 \psi_L \tag{1.7}$$

$$J_\mu^{\mathrm{EM}} = \bar{\psi} \gamma_\mu Q \psi \tag{1.8}$$

where the σ's are the Pauli spin matrices acting in weak isospin space.

1.1.2 Experimental Successes of the GWS Model

As mentioned before, the GWS model makes some significant and testable predictions. Here some of the most important experimental confirmations of those predictions are discussed, in a somewhat historical order.

Observation of Weak Neutral Currents

The Z_μ term in Equation 1.5 gives rise to a weak neutral current, which was a phenomenon absent from the $V-A$ theory. A weak neutral current can mediate a process such as $\nu_\mu(\bar{\nu}_\mu) + \mathrm{N} \rightarrow \nu_\mu(\bar{\nu}_\mu) + \text{hadrons}$. This type of reaction was observed in the Gargamelle bubble chamber at CERN in 1973, where the ratio of neutral- to charged-current events was measured. These measurements can be used to determine $\sin^2\theta_W$, although the limited precision of this first experiment only allowed the statement "in the range 0.3 to 0.4" [4]. The more important result was the establishment of the existence of weak neutral currents, as these are the key to cancelling the divergent parts of the $V-A$ theory.

Discovery of the $\mathrm{W}^\pm$ and Z^0 Bosons

The GWS theory not only predicts the existence of the $\mathrm{W}^\pm$ and Z^0 bosons, it predicts their masses in terms of G_F, the electromagnetic coupling, and θ_W. If one examines

the first term in Equation 1.5, makes a connection with the old $V - A$ theory, and includes a propagator of $1/m_{\mathrm{W}}^2$ for the W boson, one finds

$$m_{\mathrm{W}} = \left(\frac{g^2\sqrt{2}}{8G_F} \right)^{1/2} = \left(\frac{e^2\sqrt{2}}{8G_F \sin^2\theta_W} \right)^{1/2} \tag{1.9}$$

By using Equations 1.3 and 1.4 and the empirical fact that the photon is massless, one finds

$$m_{\mathrm{Z}} = \frac{m_{\mathrm{W}}}{\cos\theta_W} \tag{1.10}$$

By 1983 $\sin^2\theta_W$ had been measured fairly well (0.23 ± 0.01) and therefore the predicted masses of the $\mathrm{W}^{\pm}$ and Z^0 stood at about 83 and 94 GeV/c^2, respectively. By studying high-energy ($\sqrt{s} = 540$ GeV) proton-antiproton annihilations at CERN's Sp$\bar{\mathrm{p}}$S collider, the UA1 and UA2 collaborations were able to observe the $\mathrm{W}^{\pm}$ through its decay into a high-energy charged lepton and neutrino [5, 6]. This discovery was quickly followed by observations of the decay of the Z^0 into a pair of charged leptons [7, 8]. The experiments' final measurements of the $\mathrm{W}^{\pm}$ and Z^0 masses were 81 and 94 GeV/c^2, respectively, in good agreement (within theoretical and experimental uncertainties) with the predicted values.

Precision Measurements at the Z^0 Resonance

The GWS theory was really put to the test with the advent of the "Z factories," $\mathrm{e}^+\mathrm{e}^-$ colliders tuned to a center-of-mass energy at the Z^0 resonance. The four detectors at CERN's circular LEP collider (OPAL, ALEPH, DELPHI, and L3) collected a total of 16 million Z^0 bosons from 1989 to 1995, while the SLD detector at the Stanford Linear Accelerator Center (SLAC) collected over 500,000 Z^0 bosons from 1992 to 1998 with the added bonus of a partially polarized electron beam. These high-statistics data samples allowed high-precision measurements of various characteristics of the Z^0 (mass, width, etc.) and properties of the angular distributions of its decay products (*e.g.* forward-backward asymmetries, and additionally left-right asymmetries at SLD). Precision calculations of these quantities can be made in the GWS theory,

and comparison between theory and experiment yields excellent agreement. This is summarized in Figure 1.1, where the difference between the measured and predicted values divided by the experimental uncertainty (the "pull") is shown for a number of measurements.

1.2 The Standard Model Higgs Mechanism

The electroweak theory as presented above, for all its successes, is incomplete, as any theory with massive bosons is not gauge invariant. To see this, note that the complete Lagrangian will contain terms like $m_A^2 A_\mu A^\mu$, which is not invariant under a general gauge transformation $A_\mu \rightarrow A_\mu - \partial_\mu \chi(x)$ unless $m_A^2 = 0$. The founding fathers of GWS knew this, of course, and their solution was to invoke a mechanism developed by Peter Higgs [9], wherein a scalar field with a non-vanishing vacuum expectation value (VEV) is inserted into a theory with massless gauge bosons. After suitable algebraic transformations on the Lagrangian, the gauge bosons acquire mass as we shall now demonstrate.

Consider a complex scalar SU(2) doublet field $\phi(x)$, with VEV

$$\langle \phi \rangle = \frac{1}{\sqrt{2}} \begin{pmatrix} 0 \\ v \end{pmatrix} \tag{1.11}$$

A Lagrangian leading to this VEV is

$$\mathcal{L} = |D_\mu \phi|^2 + \mu^2 \phi^\dagger \phi - \lambda (\phi^\dagger \phi)^2 \tag{1.12}$$

as the minimum of the potential occurs at $v = \sqrt{\mu^2/\lambda}$. The $\mathrm{SU(2)} \otimes \mathrm{U(1)}$ covariant derivative appearing in Equation 1.12 is

$$D_\mu = \partial_\mu + ig \frac{\boldsymbol{\sigma} \cdot \mathbf{W}_\mu}{2} + ig' \frac{Y}{2} B_\mu \tag{1.13}$$

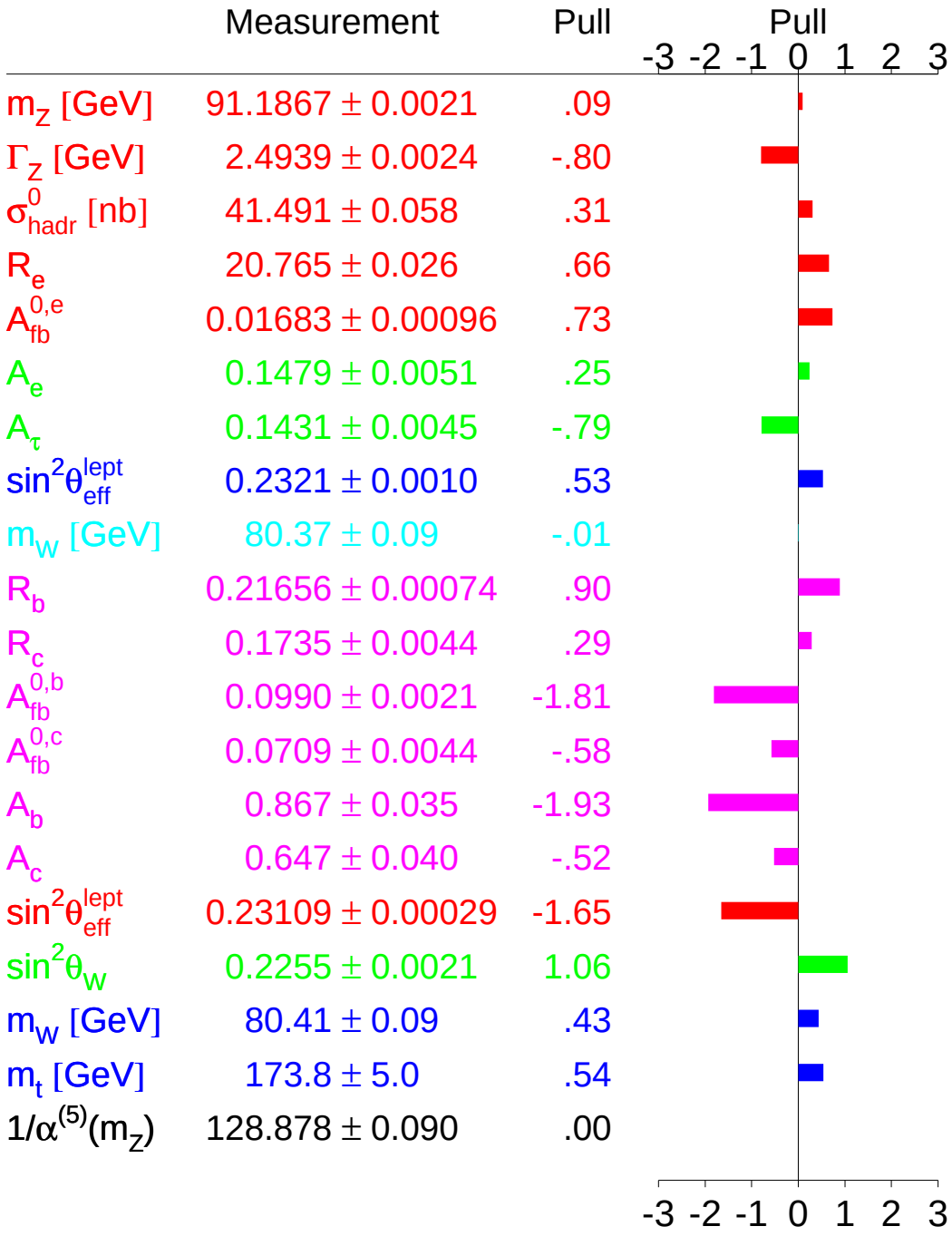

Figure 1.1: The pull ($x_{\rm theo} - x_{\rm meas}$ divided by $\sigma_{\rm meas}$) for various electroweak observables.

Expanding $\phi(x)$ about its minimum

$$\phi(x) = \frac{1}{\sqrt{2}} \begin{pmatrix} 0 \\ v + h(x) \end{pmatrix} \tag{1.14}$$

where $h(x)$ is a real-valued field, we can rewrite Equation 1.12 making use of Equations 1.2–1.4 as

$$\mathcal{L} = \frac{1}{2}(\partial_\mu h)^2 + 2 \cdot \frac{1}{2}\left(\frac{gv}{2}\right)^2 W_\mu^+ W^{\mu-} + \frac{1}{2}\left(\frac{gv}{2\cos\theta_W}\right)^2 Z_\mu Z^\mu - \lambda v^2 h^2 + \ldots \tag{1.15}$$

We see that the SU(2) $\otimes$ U(1) symmetry has been broken by the new vacuum, resulting in $\mathrm{W}^\pm$ and Z^0 bosons with masses $gv/2$ and $gv/(2\cos\theta_W)$, respectively, and *a new scalar boson with mass* $\sqrt{2\lambda v^2}$, called the "Higgs boson," or H^0. Note that although the value of v can be determined from the known W mass ($v = 246\ \mathrm{GeV}/c^2$), λ is unspecified, and thus the Higgs mass is undetermined.

An additional attractive feature of the Higgs mechanism is that it provides a way to generate masses for the quarks and leptons. Taking the electron for a concrete example, we note that a mass term in the Lagrangian such as $-m_\mathrm{e}(\bar{e}_L e_R + \bar{e}_R e_L)$ is again not gauge invariant, since e_L and e_R belong to different representations of SU(2) and have different U(1) hypercharges. However, by including a Yukawa-like coupling to the scalar SU(2) doublet ϕ, we can write a mass term like

$$\Delta\mathcal{L}_e = -\lambda_e \bar{L}_L \cdot \phi e_R + \mathrm{h.c.} \tag{1.16}$$

that *is* gauge invariant, since the SU(2) indices of L_L (the lepton SU(2) doublet) contract with ϕ and the hypercharges of the fields sum to zero. At the minimum of the potential, then,

$$\Delta\mathcal{L}_e = -\frac{\lambda_e}{\sqrt{2}} v \bar{e}_L \cdot e_R + \mathrm{h.c.} \tag{1.17}$$

giving an electron mass ($m_\mathrm{e} = \lambda_e v/\sqrt{2}$) characterized by the Higgs VEV v and the new dimensionless coupling λ_e. The mechanism is similar for the quarks, and absent for the neutrinos due to the absence of ν_R. Note that the Higgs mechanism does

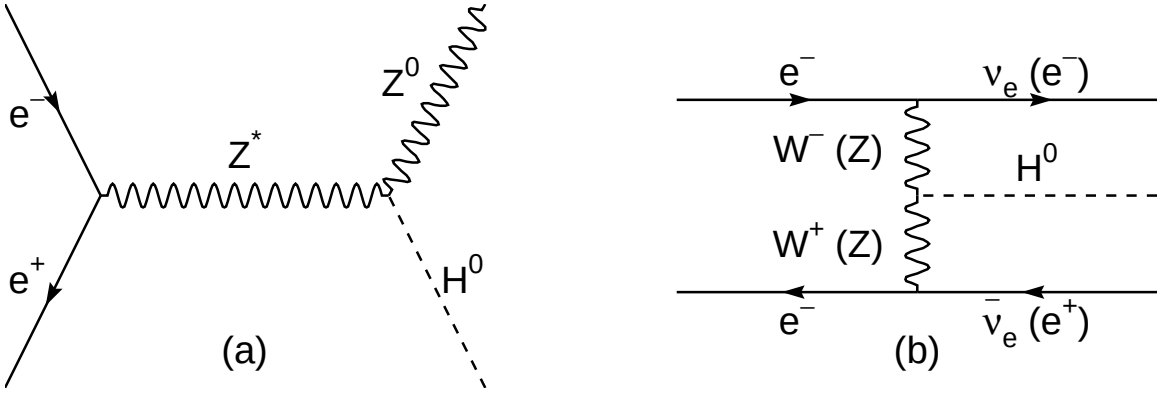

Figure 1.2: Feynman diagrams for SM Higgs production at LEP2 via (a) Higgs-strahlung and (b) vector boson fusion.

not explain the *values* of the fermion masses (the arbitrary masses have just been replaced with arbitrary λ couplings), but it does make it possible for them to have masses at all.

1.3 The Standard Model Higgs Boson

Equation 1.15 shows just a few terms in the complete Standard Model Lagrangian involving the Higgs boson. When written out in full, the Feynman rules and Higgs couplings can be determined and used to calculate useful quantities like Higgs cross sections, branching ratios, etc. in terms of one free parameter, m_{H}. This is done for example in [10], and some relevant results will be presented here. The guiding principle when constructing Higgs boson phenomenology is that the coupling strength of the Higgs to another particle is proportional to that particle's mass.

1.3.1 SM Higgs Production at LEP2

Figure 1.2 shows the two mechanisms for producing a Standard Model Higgs boson at LEP2. The diagram in Figure 1.2a is called "Higgsstrahlung;" the virtual Z from an $\mathrm{e^+e^-}$ annihilation "radiates" a Higgs and subsequently goes on-shell. One sees that the mass of a Higgs produced in this manner is limited by kinematics to $\sqrt{s} - m_{\mathrm{Z}}$. Figure 1.2b shows the "vector boson fusion" process, wherein the Higgs is produced

via the fusion of two W's (Z's), leading to a Higgs produced in association with a $\nu_e\bar{\nu}_e$ (e^+e^-) pair. Below the aforementioned kinematic limit, the cross section for the fusion process is smaller than that for Higgsstrahlung by over an order of magnitude; thus we do not pursue it further.

The tree-level cross section for the Higgsstrahlung process can be written as

$$\sigma(e^+e^- \to H^0Z^0) = \frac{G_F^2 m_Z^4}{96\pi s}(a_e^2 + v_e^2)\frac{\lambda + 12m_Z^2/s}{(1 - m_Z^2/s)^2}\sqrt{\lambda} \tag{1.18}$$

where a_e and v_e are the axial and vector couplings of the electron (-1 and $-1 + 4\sin^2\theta_W$, respectively). The Higgs mass enters into this formula through the two-particle phase space factor λ:

$$\lambda = \left(1 - \frac{m_H^2 + m_Z^2}{s}\right)^2 - \frac{4m_H^2 m_Z^2}{s^2} \tag{1.19}$$

The cross section as a function of m_H is shown in Figure 1.3 for three representative LEP2 center-of-mass energies. It should be noted that the cross sections for typical SM processes at LEP2 (QCD, four-fermion production, etc.) can be two orders of magnitude larger than the Higgsstrahlung cross section.

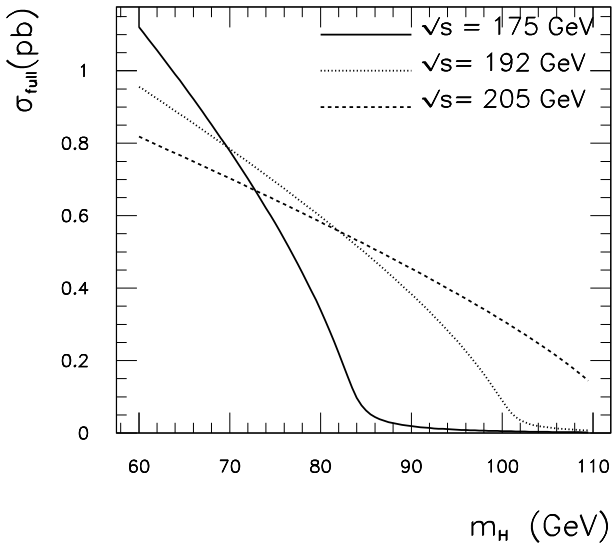

Figure 1.3: The SM Higgsstrahlung cross section as a function of m_H for three representative LEP2 center-of-mass energies.

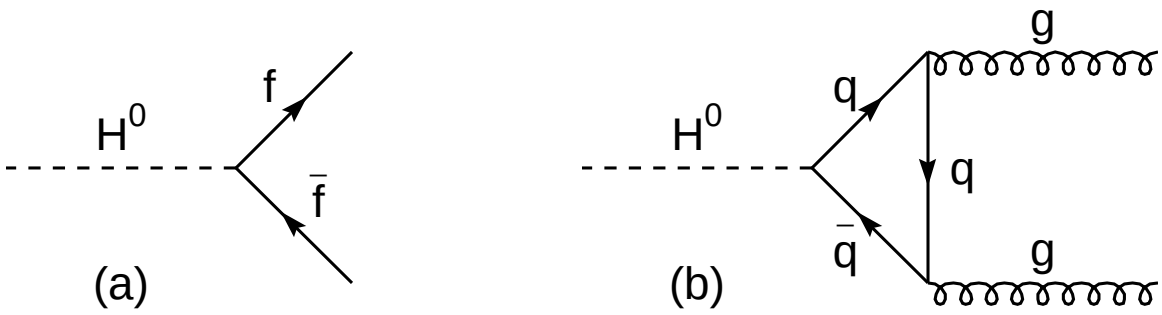

Figure 1.4: Diagrams for the two dominant SM Higgs decay types at LEP2.

1.3.2 SM Higgs Decays

Figure 1.4 shows diagrams for the main decay modes for Higgs bosons in the LEP2 mass range of interest. The partial width for a decay into a fermion-antifermion pair (Figure 1.4a) is given at tree level by:

$$\Gamma(\mathrm{H}^0 \to f\bar{f}) = \frac{N_c G_F m_f^2 m_\mathrm{H}}{4\pi\sqrt{2}} \left(1 - \frac{4m_f^2}{m_\mathrm{H}^2}\right)^{3/2} \tag{1.20}$$

where N_c is a color factor (1 for leptons, 3 for quarks). Note the factor of m_f^2, indicating the preferential coupling of H^0 to high-mass particles. Due to confinement, quark masses are not well-defined quantities and therefore Equation 1.20 needs to be modified by the leading-log QCD calculation for the quark mass.

Figure 1.4b shows the decay of a Higgs into a pair of gluons through a virtual quark loop. Again due to the preferential coupling to high mass, top quark loops provide the dominant contribution and the tree-level partial width is (for $2m_\mathrm{t} > m_\mathrm{H}$):

$$\Gamma(\mathrm{H}^0 \to gg) = \frac{\alpha_s^2 G_F m_\mathrm{H}^3}{16\pi^3\sqrt{2}} \left| \frac{4m_\mathrm{t}^2}{m_\mathrm{H}^2} \left\{ 1 + \left[1 - \frac{4m_\mathrm{t}^2}{m_\mathrm{H}^2}\right] \left[\sin^{-1}\left(\frac{m_\mathrm{H}}{2m_\mathrm{t}}\right)\right]^2 \right\} \right|^2 \tag{1.21}$$

Figure 1.5 shows the SM Higgs branching ratios as a function of m_H. As b quarks are the heaviest decay products kinematically available to Higgs bosons at LEP2,

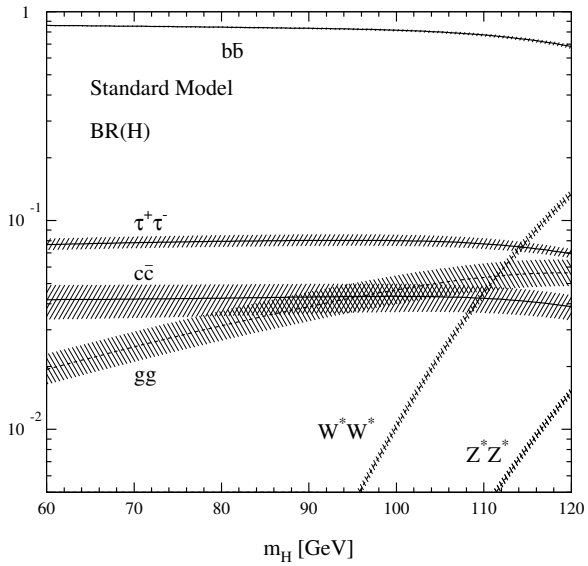

Figure 1.5: SM Higgs branching ratios as a function of m_{H}. The bands represent the theoretical uncertainty.

they dominate the branching ratio at about 85%. The next largest branching ratio is into tau leptons (the next heaviest particle) at about 7%. Therefore these two decay modes together account for over 90% of all SM Higgs decays at LEP2.

1.3.3 SM Higgs Final State Topologies

Since the Higgs decays predominantly to b quarks, SM Higgs searches at LEP2 are split into four topologies based essentially on the decay of the associated Z^0. These four topologies are shown pictorially in Figure 1.6 and discussed briefly below.

1. **"4-jet."** This topology has the largest signal rate (about 60% of the total H^0Z^0 cross section), due to the 70% $Z^0 \to q\bar{q}$ branching ratio. It is characterized by four energetic hadron jets, two of which are expected to carry b-flavor from the Higgs decay. This channel has a substantial background from SM QCD four-jet production.

2. **"Missing energy."** This channel is based on the decay of the Z^0 into a pair of neutrinos, resulting in a substantial amount of undetected ("missing") energy in addition to the two Higgs b jets. It has the second-largest signal rate (about

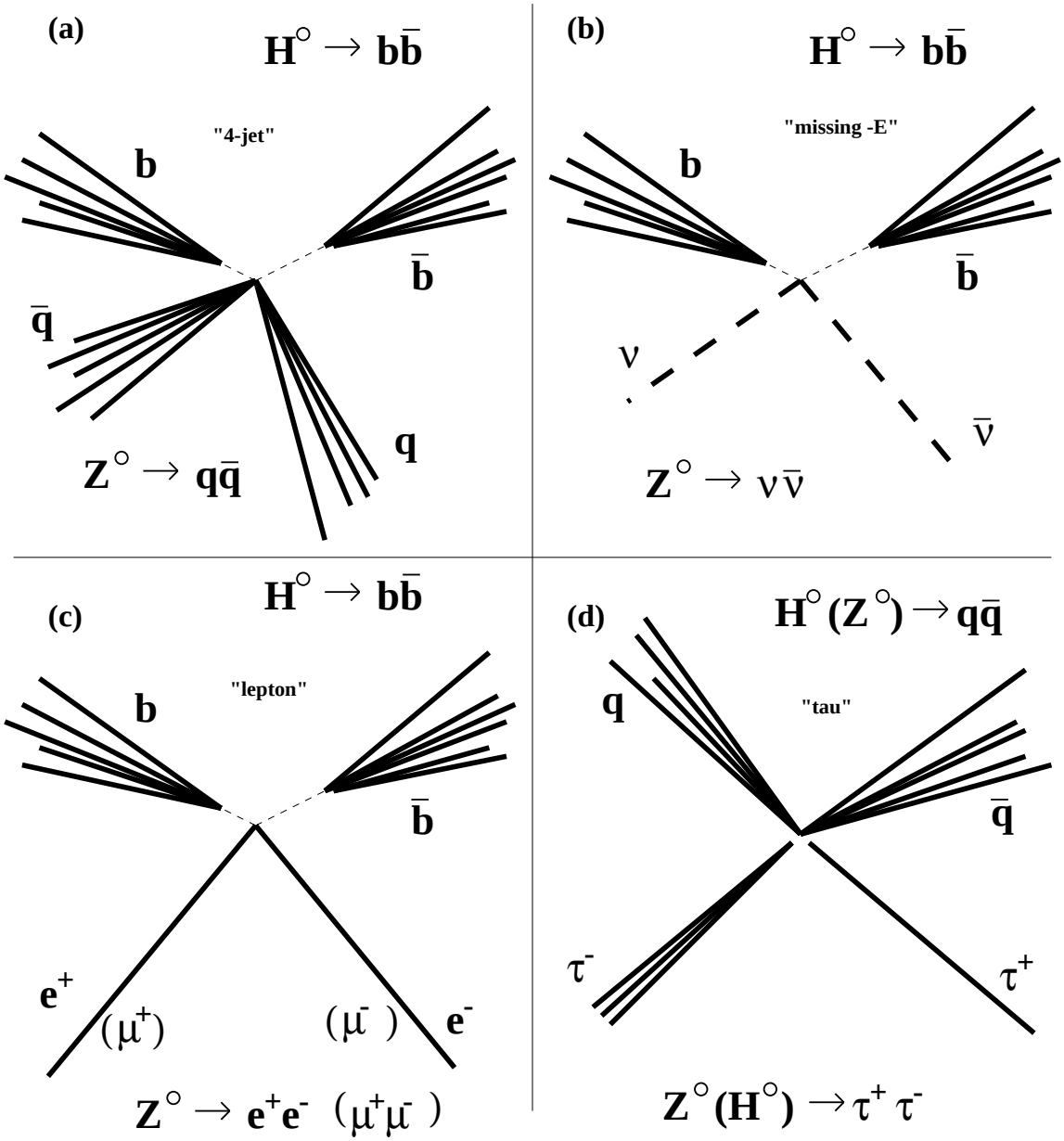

Figure 1.6: Pictorial representations of the (a) 4-jet, (b) missing energy, (c) lepton, and (d) tau channel SM Higgs search topologies.

18%) and less background than the 4-jet channel; however, determining the Higgs mass via its recoil off the missing energy requires detailed understanding of the detector acceptance.

3. **"Lepton."** This channel corresponds to decays of the Z^0 into an electron or muon pair in association with the $H^0 \to b\bar{b}$ decay. Its small branching fraction (about 6%) is somewhat compensated by having very little background and excellent resolution on the Higgs mass.

4. **"Tau."** The tau channel, which is the focus of this thesis, is an interesting one because it gives "two for the price of one." In addition to the canonical $H^0 \to b\bar{b}$, $Z^0 \to \tau^+\tau^-$ process, it contains the topologically similar $H^0 \to \tau^+\tau^-$, $Z^0 \to q\bar{q}$ process. All together, the tau channel accounts for about 8% of the total H^0Z^0 cross section in the minimal SM Higgs scenario.

Collectively, the four channels cover approximately 90% of SM Higgs production at LEP2.

1.3.4 Theoretical Constraints on the SM Higgs Mass

As noted before, the Higgs mass is a free parameter of the SM, and it is worthwhile to ask what sort of bounds can be placed on m_H from purely theoretical considerations. Recall that m_H^2 is proportional to the quartic Higgs coupling λ; since this coupling grows with rising energy Q an upper bound on m_H follows from requiring the SM to be valid up to some scale Λ. Specifically, the requirement is that $\sqrt{2}\lambda(\Lambda)/4\pi \leq 1$, so that Λ characterizes the scale at which the system becomes strongly interacting (this is essentially where λ develops a Landau pole). The one-loop renormalization group equation for λ is

$$\frac{d\lambda}{dt} = \frac{1}{16\pi^2}(12\lambda^2 + 6\lambda h_t^2 - 3h_t^4) + \text{EW contributions} \tag{1.22}$$

where $t = \ln(Q^2/\Lambda^2)$ and h_t is the top-Higgs Yukawa coupling. Note that the first two terms drive λ to its perturbative limit. The third term drives λ negative and a lower

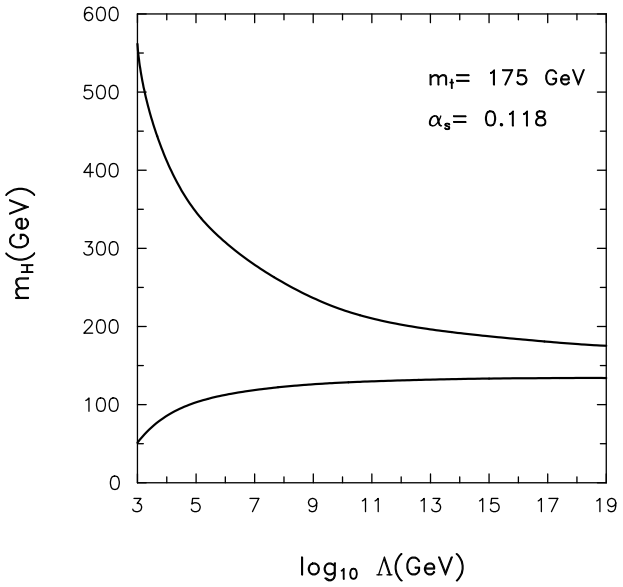

Figure 1.7: Upper and lower bounds on the SM Higgs mass from theoretical considerations of strong interaction and vacuum stability [11]. Λ denotes the scale at which particles become strongly interacting.

bound on m_{H} can be set by demanding stability of the EW vacuum, *i.e.* the bound is the lowest Higgs mass for which $\lambda \geq 0$ for any scale below Λ. Figure 1.7 shows these upper and lower bounds as a function of Λ; one can see that with $m_{\mathrm{t}} = 175$ GeV/c^2 a discovery of the Higgs at LEP2 would imply the existence of new physics at scales on the order of a few to 100 TeV.

1.4 Two Higgs Doublet Models

The Higgs mechanism described in the previous section is "minimal" in the sense that the introduction of one scalar doublet in the theory is sufficient to break the SU(2) ⊗ U(1) symmetry. However, as there currently exist no experimental data on the symmetry-breaking sector of the Standard Model, it is worthwhile to investigate more complex Higgs mechanisms.

There are actually a multitude of ways to effect the Higgs mechanism using any number of Higgs singlets, doublets, triplets, etc. However, they are all subject to two important constraints. The first concerns the so-called "ρ parameter." This

parameter, defined as

$$\rho = \frac{m_{\mathrm{W}}^2}{m_{\mathrm{Z}}^2 \cos^2 \theta_W} \tag{1.23}$$

is sensitive to the content of the Higgs sector of the theory and has been revealed by precise measurements of m_{W}, m_{Z}, and θ_W to be extremely close to unity. In the minimal Standard Model Higgs scenario ρ is automatically equal to 1 (hence its suppression in Equation 1.10); in fact, this holds true for any model which contains only Higgs doublets or singlets. More complicated representations can also yield $\rho = 1$, but only after a fine tuning of the parameters of the Higgs potentials.

The second constraint concerns the severe experimental limits on flavor-changing neutral currents (FCNC's). The absence of tree-level FCNC's is again automatic in the minimal Standard Model Higgs mechanism. In more complicated models, one can generally avoid the problem by arranging parameters such that the Higgses are heavy enough (~ 1 TeV/c^2) that FCNC's mediated by Higgs exchange are sufficiently suppressed to be consistent with experimental limits. However, a more elegant solution is based on a theorem by Glashow and Weinberg [12] which states that in models with more than one Higgs doublet, tree-level FCNC's will be absent if fermions of a given electric charge couple to no more than one doublet.

Thus the above two constraints lead one to favor a model with two Higgs doublets over more complicated models; to sum up,

1. It is the simplest possible extension of the minimal Standard Model Higgs mechanism (just add one doublet).

2. The constraint $\rho = 1$ is satisfied automatically at tree level.

3. Tree-level FCNC's are automatically absent if the condition of Glashow and Weinberg is satisfied.

A final point in favor of a two-Higgs-doublet model (henceforth referred to as 2HDM) is that it is the minimal form of EW symmetry breaking that can also accommodate supersymmetry (SUSY). The discussion of this point will be postponed until the discussion of the Minimal Supersymmetric Standard Model (MSSM) in Section 1.5.

1.4.1 2HDM Basics

For two $Y = 1/2$, $\mathrm{SU}(2)_L$ doublets ϕ_1 and ϕ_2, the most general potential that spontaneously breaks $\mathrm{SU}(2) \otimes \mathrm{U}(1)$ as required is given by

$$\begin{aligned} V(\phi_1, \phi_2) &= \lambda_1(\phi_1^\dagger\phi_1 - v_1^2)^2 + \lambda_2(\phi_2^\dagger\phi_2 - v_2^2)^2 + \\ &\quad \lambda_3[(\phi_1^\dagger\phi_1 - v_1^2)^2 + (\phi_2^\dagger\phi_2 - v_2^2)]^2 + \\ &\quad \lambda_4[(\phi_1^\dagger\phi_1)(\phi_2^\dagger\phi_2) - (\phi_1^\dagger\phi_2)(\phi_2^\dagger\phi_1)] + \\ &\quad \lambda_5[\mathrm{Re}(\phi_1^\dagger\phi_2) - v_1 v_2 \cos\xi]^2 + \\ &\quad \lambda_6[\mathrm{Im}(\phi_1^\dagger\phi_2) - v_1 v_2 \sin\xi]^2 \end{aligned} \tag{1.24}$$

where the λ_i's are real and positive. The Higgs fields acquire VEV's at the minimum of the potential given by

$$\langle\phi_1\rangle = \begin{pmatrix} 0 \\ v_1 \end{pmatrix}, \qquad \langle\phi_2\rangle = \begin{pmatrix} 0 \\ v_2 e^{i\xi} \end{pmatrix} \tag{1.25}$$

The parameter ξ controls the amount of CP violation in the Higgs sector; for this analysis it is set to zero.

To determine the physical spectrum of the theory, it is easiest to employ the real basis

$$\phi_1 \equiv \begin{pmatrix} \phi_1^+ \\ \phi_1^0 \end{pmatrix} = \frac{1}{\sqrt{2}} \begin{pmatrix} \phi_1 + i\phi_2 \\ \phi_3 + i\phi_4 \end{pmatrix} \rightarrow \begin{pmatrix} \phi_1 \\ \phi_2 \\ \phi_3 \\ \phi_4 \end{pmatrix} \tag{1.26}$$

$$\phi_2 \equiv \begin{pmatrix} \phi_2^+ \\ \phi_2^0 \end{pmatrix} = \frac{1}{\sqrt{2}} \begin{pmatrix} \phi_5 + i\phi_6 \\ \phi_7 + i\phi_8 \end{pmatrix} \rightarrow \begin{pmatrix} \phi_5 \\ \phi_6 \\ \phi_7 \\ \phi_8 \end{pmatrix} \tag{1.27}$$

The Higgs boson mass matrix is determined by evaluating

$$M_{ij}^2 = \frac{\partial^2 V}{\partial\phi_i \partial\phi_j} \tag{1.28}$$

at the minimum of the potential, where $\langle\phi_3\rangle = v_1$, $\langle\phi_7\rangle = v_2$, and all other $\langle\phi_i\rangle = 0$. The mass matrix separates into a series of 2×2 matrices, which are easily diagonalized to find the physical Higgs states as follows.

Making the definition $\tan\beta \equiv v_2/v_1$, we find there is a charged sector given by

$$H^\pm = -\phi_1^\pm \sin\beta + \phi_2^\pm \cos\beta \tag{1.29}$$

where $\phi_i^- \equiv \phi_i^{+*}$. The corresponding mass-squared eigenvalues are $m_{\mathrm{H}^\pm}^2 = \lambda_4(v_1^2+v_2^2)$. This thesis is concerned with neutral Higgs bosons and therefore we do not pursue charged Higgses further. The neutral CP-odd sector of the theory contains

$$A^0 = \sqrt{2}(-\mathrm{Im}\ \phi_1^0 \sin\beta + \mathrm{Im}\ \phi_2^0 \cos\beta) \tag{1.30}$$

with $m_{\mathrm{A}}^2 = \lambda_6(v_1^2+v_2^2)$. The neutral CP-even sector contains two Higgs bosons which mix through the following mass-squared matrix:

$$\mathcal{M} = \begin{pmatrix} 4v_1^2(\lambda_1+\lambda_3)+v_2^2\lambda_5 & (4\lambda_3+\lambda_5)v_1v_2 \\ (4\lambda_3+\lambda_5)v_1v_2 & 4v_2^2(\lambda_2+\lambda_3)+v_1^2\lambda_5 \end{pmatrix} \tag{1.31}$$

Defining a mixing angle α as

$$\sin 2\alpha = \frac{2\mathcal{M}_{12}}{\sqrt{(\mathcal{M}_{11}-\mathcal{M}_{22})^2+4\mathcal{M}_{12}^2}},\ \cos 2\alpha = \frac{\mathcal{M}_{11}-\mathcal{M}_{22}}{\sqrt{(\mathcal{M}_{11}-\mathcal{M}_{22})^2+4\mathcal{M}_{12}^2}} \tag{1.32}$$

the neutral CP-even physical Higgs states are

$$H^0 = \sqrt{2}[(\mathrm{Re}\ \phi_1^0 - v_1)\cos\alpha + (\mathrm{Re}\ \phi_2^0 - v_2)\sin\alpha] \tag{1.33}$$

and

$$h^0 = \sqrt{2}[(-\mathrm{Re}\ \phi_1^0 - v_1)\sin\alpha + (\mathrm{Re}\ \phi_2^0 - v_2)\cos\alpha] \tag{1.34}$$

with masses

$$m^2_{\mathrm{H}^0,\mathrm{h}^0} = \frac{1}{2}\left[\mathcal{M}_{11} + \mathcal{M}_{22} \pm \sqrt{(\mathcal{M}_{11} - \mathcal{M}_{22})^2 + 4\mathcal{M}^2_{12}}\right] \tag{1.35}$$

where $m_{\mathrm{H}^0} > m_{\mathrm{h}}$ by definition.

The quantity $v_1^2 + v_2^2$ is fixed by the W mass ($m_{\mathrm{W}} = g(v_1^2 + v_2^2)/2$), but the λ_i's are arbitrary. Therefore this model has six free parameters, namely $m_{\mathrm{H}^\pm}$, m_{A}, m_{h}, m_{H^0}, $\tan\beta$, and α.

1.4.2 2HDM Phenomenology

The Feynman rules for a 2HDM can be found in [10]; the important results concern the couplings of the Higgs bosons to the vector bosons and fermions of the Standard Model, which can be expressed as the Standard Model Higgs couplings rescaled by factors depending on α and β. In particular, the scaling factors for vector boson couplings are

$$h^0VV \propto \sin(\beta - \alpha), \qquad\qquad H^0VV \propto \cos(\beta - \alpha) \tag{1.36}$$

The Higgs-fermion couplings depend on how the condition for avoiding tree-level FCNC's mentioned in Section 1.4 is met. 2HDM's generally fall into one of two types according to how this condition is satisfied. The first (Type I) couples ϕ_1 to gauge bosons and ϕ_2 to quarks and leptons exclusively. The second (Type II) couples the down-type fermions to ϕ_1 and the up-type fermions to ϕ_2 exclusively. For this discussion we concentrate on a Type II 2HDM since this is the type required in the MSSM, as will be shown. In a Type II 2HDM, the couplings of the SM Higgs to up- and down-type fermions (represented here with a generic u and d) are rescaled according to the factors:

$$\begin{aligned} H^0 u\bar{u} &\propto \frac{\sin\alpha}{\sin\beta} & H^0 d\bar{d} &\propto \frac{\cos\alpha}{\cos\beta} \\ h^0 u\bar{u} &\propto \frac{\cos\alpha}{\sin\beta} & h^0 d\bar{d} &\propto \frac{-\sin\alpha}{\cos\beta} \\ A^0 u\bar{u} &\propto \cot\beta & A^0 d\bar{d} &\propto \tan\beta \end{aligned} \tag{1.37}$$

Finally, there are a new set of couplings in a 2HDM involving more than one Higgs boson. Two that are relevant here are

$$g_{h^0A^0Z} = \frac{g}{2\cos\theta_W}\cos(\beta-\alpha), \qquad g_{H^0A^0Z} = \frac{g}{2\sin\theta_W}\sin(\beta-\alpha) \tag{1.38}$$

With these couplings in hand, the phenomenology of a Type II 2HDM is easily constructed. Since h^0 and H^0 play essentially equivalent roles and h^0, being lighter, is more easily accessible by experiment, we restrict ourselves to discussion of h^0 when either can appear. First of all, the nominal Higgsstrahlung production process of Figure 1.2a (with H^0 replaced by h^0) is supplemented by a new possible production mechanism (by virtue of the new couplings of Equation 1.38) shown in Figure 1.8. The cross section for this new "pair-production" process is given at tree level by

$$\sigma(e^+e^- \to h^0A^0) = \cos^2(\beta-\alpha)\bar{\lambda}\sigma_{HZ}^{SM} \tag{1.39}$$

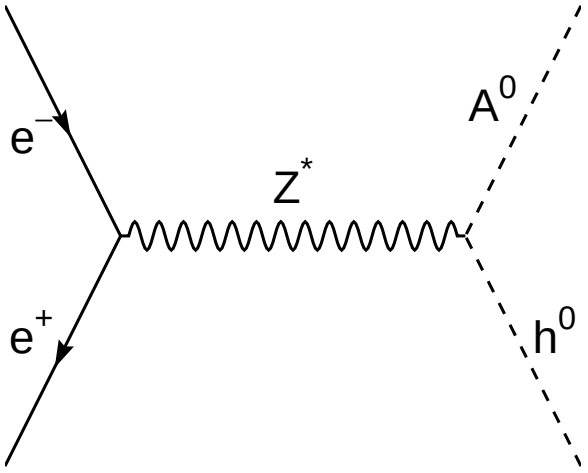

Figure 1.8: The h^0A^0 pair-production process.

where $\bar{\lambda}$, defined as

$$\bar{\lambda} = \frac{\lambda_{\mathrm{Ah}}^{3/2}}{[(12m_{\mathrm{Z}}^2/s) + \lambda_{\mathrm{Zh}}]\sqrt{\lambda_{\mathrm{Zh}}}} \tag{1.40}$$

accounts for the correct suppression of the p-wave cross section near threshold (λ_{ij} is the phase space factor given by Equation 1.19 for $ij = \mathrm{ZH}$). By virtue of the couplings of Equation 1.36, one sees that the cross section for Higgsstrahlung is simply suppressed by a factor of $\sin^2(\beta - \alpha)$:

$$\sigma(\mathrm{e^+e^-} \to \mathrm{h^0Z^0}) = \sin^2(\beta - \alpha)\sigma_{\mathrm{HZ}}^{\mathrm{SM}} \tag{1.41}$$

Note that the $\cos^2(\beta - \alpha)$ and $\sin^2(\beta - \alpha)$ factors occurring in Equations 1.39 and 1.41 indicate a complementarity between the two production mechanisms.

Higgs decays in a Type II 2HDM can be determined from the pattern of SM Higgs decays bearing in mind the altered couplings listed in Equation 1.37. It is worthwhile to recall that α and $\tan\beta$ are free parameters, and therefore the rule of thumb that a Higgs decays predominantly to $\mathrm{b\bar{b}}$ and $\tau^+\tau^-$ pairs does not necessarily hold. For suitable choices of α and $\tan\beta$, the $\mathrm{b\bar{b}}$ and $\tau^+\tau^-$ branching ratios can be heavily suppressed, compensated by an enhancement of the branching ratios into $\mathrm{c\bar{c}}$ (and gg, via the enhanced coupling to $\mathrm{t\bar{t}}$). If, for the moment, we assume that $\mathrm{b\bar{b}}$ and $\tau^+\tau^-$ decays are not suppressed, we recover for the Higgsstrahlung process the same search topologies listed in Section 1.3.3. For the pair-production process, we have new topologies with four heavy final-state fermions, the two dominant ones being $\mathrm{h^0A^0} \to \mathrm{b\bar{b}b\bar{b}}$ and $\mathrm{h^0A^0} \to \mathrm{b\bar{b}}\tau^+\tau^-(\tau^+\tau^-\mathrm{b\bar{b}})$.

1.5 Supersymmetry and the MSSM

In the previous sections we have seen how the Higgs boson rounds out the Standard Model by signalling the mechanism of electroweak symmetry breaking. Ironically enough, it is the Higgs boson that also brings out the manifest incompleteness of the Standard Model at high energies. The problem lies in the radiative corrections to the Higgs mass-squared and goes by the name of the "hierarchy problem." If a fermion

couples to the Higgs with a strength λ_f (cf. Equation 1.16) then the contribution to the Higgs mass-squared from a diagram containing a fermion bubble is

$$\Delta m_{\mathrm{H}}^2 = \frac{|\lambda_f|^2}{16\pi^2}\left(2\Lambda_{\mathrm{UV}}^2 - 6m_f^2 \ln\frac{\Lambda_{\mathrm{UV}}}{m_f} + \dots\right) \tag{1.42}$$

where Λ_{UV} is an ultraviolet momentum cutoff used to regulate the loop integral, to be interpreted as the energy scale at which new physics enters to alter the high-energy behavior of the theory. If the Standard Model is the "true" theory up to the Planck scale M_P, where gravity must enter the game, then the correction to m_{H}^2 is on the order of $(10^{18}\ \mathrm{GeV})^2$. This should be compared with the "natural" value of the Higgs mass, which should be roughly the order of the electroweak symmetry-breaking scale set by the Higgs VEV, *i.e.* $m_{\mathrm{H}}^2 \sim (10^2\ \mathrm{GeV})^2$. For the Higgs to retain its natural mass, then, there must be a mass-squared counterterm that cancels the fermion-induced Δm_{H}^2 to roughly one part in 10^{16}! This ultrafine tuning of parameters is of course technically possible, but is profoundly unnatural and displeasing. It is worthwhile to note that this quadratic divergence is a feature only of corrections to scalar mass-squareds.

If the theory also contains massive scalar particles, each with its own Higgs coupling λ_S, then there will be another contribution to Δm_{H}^2 from loops involving scalars given by

$$\Delta m_{\mathrm{H}}^2 = \frac{|\lambda_S|^2}{16\pi^2}\left(-2\Lambda_{\mathrm{UV}}^2 + 4m_S^2 \ln\frac{\Lambda_{\mathrm{UV}}}{m_S} + \dots\right) \tag{1.43}$$

The relative minus sign between Equations 1.42 and 1.43 is the well-known result of Fermi statistics. The implication is clear; if there exist scalar "partners" to the Standard Model fermions (in the sense of having the same Higgs couplings), the quadratically divergent corrections to m_{H}^2 cancel. If this cancellation is to hold to all orders in perturbation theory it must be the result of a symmetry relating particles of different spin; symmetries of this type are called supersymmetries.

The MSSM has no additional fields beyond the supersymmetric partners of the Standard Model particles. The SM fermions and their spin-0 partners are arranged in chiral supermultiplets, whereas the SM gauge bosons and their spin-1/2 partners are arranged in gauge supermultiplets. This is illustrated in Table 1.2. Supersymmet-

Chiral supermultiplets			
superfield	spin-0 component	spin-1/2 component	SU(3), SU(2), U(1) representation
$\hat{Q}$	$(\tilde{u}_L, \tilde{d}_L)$	(u_L, d_L)	($\mathbf{3}$, $\mathbf{2}$, 1/6)
$\hat{U}$	$\tilde{u}_R^*$	$u_R^\dagger$	($\bar{\mathbf{3}}$, $\mathbf{1}$, -2/3)
$\hat{D}$	$\tilde{d}_R^*$	$d_R^\dagger$	($\bar{\mathbf{3}}$, $\mathbf{1}$, 1/3)
$\hat{L}$	$(\tilde{\nu}, \tilde{e}_L)$	(ν, e_L)	($\mathbf{1}$, $\mathbf{2}$, -1/2)
$\hat{E}$	$\tilde{e}_R^*$	$e_R^\dagger$	($\mathbf{1}$, $\mathbf{1}$, 1)
$\hat{H}_1$	(H_1^+, H_1^0)	$(\tilde{H}_1^+, \tilde{H}_1^0)$	($\mathbf{1}$, $\mathbf{2}$, -1/2)
$\hat{H}_2$	(H_2^0, H_2^-)	$(\tilde{H}_2^0, \tilde{H}_2^-)$	($\mathbf{1}$, $\mathbf{2}$, 1/2)
Gauge supermultiplets			
	spin-1/2 component	spin-1 component	SU(3), SU(2), U(1) representation
	$\tilde{g}$	g	($\mathbf{8}$, $\mathbf{1}$, 0)
	$\tilde{W}^\pm, \tilde{W}^0$	$W^\pm, W^0$	($\mathbf{1}$, $\mathbf{3}$, 0)
	$\tilde{B}^0$	B^0	($\mathbf{1}$, $\mathbf{1}$, 0)

Table 1.2: Supermultiplets of the MSSM. Similar multiplets exist for the second and third generation of quarks and leptons.

ric fields are conventionally denoted by putting a tilde over their SM partner field. Scalar partners of SM fermions are named by adding the prefix "s-" to the SM name, whereas fermionic partners of SM bosons get the suffix "-ino." For example, the supersymmetric partner of the tau (τ) is the stau ($\tilde{\tau}$) and the supersymmetric partner of the gluon (g) is the gluino ($\tilde{\text{g}}$).

1.5.1 The MSSM Higgs Sector

Since the Higgs is a spin-0 weak isodoublet, its fermionic superpartner (the "higgsino") is also an isodoublet with weak hypercharge $Y = 1/2$ or $Y = -1/2$. Note that the SM fermions satisfy the condition for having a theory free of triangle gauge anomalies, namely $\text{Tr}[T_3^2 Y]$=0. The higgsino will spoil this balance unless there is a second Higgs doublet (and hence a second higgsino) with opposite weak hypercharge. The necessity for a second doublet also arises when considering the Higgs-fermion interactions,

obtained from the superpotential

$$W = \epsilon_{ij}(\lambda_1 \hat{H}_1^i \hat{L}^j \hat{E} + \lambda_2 \hat{H}_1^i \hat{Q}^j \hat{D} + \lambda_3 \hat{H}_2^j \hat{Q}^i \hat{U} + \mu \hat{H}_1^i \hat{H}_2^j) \tag{1.44}$$

where i and j are SU(2) indices and $\epsilon_{12} = -\epsilon_{21} = 1,\ \epsilon_{11} = \epsilon_{22} = 0$. Note the appearance of $\hat{H}_2$ in the third term, which generates mass for the up-type quarks. A term like $\lambda_3 \hat{H}_1^i \hat{Q}^j \hat{U}$ is prohibited due to gauge invariance (note $\sum Y \neq 0$). In the one-Higgs-doublet minimal Standard Model this problem is circumvented by using H_1^* to generate the up-type masses, but a general feature of supersymmetric theories is that no conjugate scalar fields can appear in the superpotential. Therefore, we see that the MSSM requires two Higgs doublets to keep the theory anomaly-free, and furthermore, it requires one doublet to couple to down-type fermions and the other to up-type fermions. Thus the MSSM Higgs sector is a 2HDM of Type II, as advertised in Section 1.4. This means the general Type II 2HDM results already given can be applied to the MSSM.

The supersymmetry constraints that make Equation 1.44 the most general MSSM superpotential allow the establishment of relationships between the six free parameters of a general 2HDM. The Higgs potential can be derived from the superpotential via

$$V(A_i) = \frac{1}{2}(D^a D^a + D'^2) + F_i^* F_i \tag{1.45}$$

where $F_i = \partial W / \partial A_i$, $D^a = g A_i^* \sigma_{ij}^a A_j / 2$, and $D' = g' Y A_i^* A_i / 2$ (A_i generically represents all scalar fields in the theory). The result is

$$V(H_1, H_2) = |\mu|^2 |H_1|^2 + |\mu|^2 |H_2|^2 + \frac{g^2 + g'^2}{8}\left(|H_1|^2 - |H_2|^2\right)^2 + \frac{g^2}{2}|H_1 H_2|^2 \tag{1.46}$$

where only the last term in Equation 1.44 has been considered; due to the vanishing VEV's for the quark and lepton fields, the corresponding superpotential terms make no contribution to the Higgs mass-squared matrix.

Equation 1.46 holds for the case of unbroken supersymmetry. However, supersymmetry is obviously a broken symmetry; if the superpartner masses were degenerate with the SM fermions they would have been discovered by now. Therefore the full

Higgs potential contains the soft supersymmetry-breaking terms

$$V_{\text{soft}} = m_1^2|H_1|^2 + m_2^2|H_2|^2 - m_{12}^2\epsilon_{ij}(H_1^i H_2^j + \text{h.c.}) \tag{1.47}$$

By comparing $V + V_{\text{soft}}$ with Equation 1.24, the following relations are found:

$$\begin{aligned}
\lambda_2 &= \lambda_1 \\
\lambda_3 &= \frac{1}{8}(g^2 + g'^2) - \lambda_1 \\
\lambda_4 &= 2\lambda_1 - \frac{1}{2}g'^2 \\
\lambda_5 &= \lambda_6 = 2\lambda_1 - \frac{1}{2}(g^2 + g'^2) \\
m_1^2 &= -|\mu|^2 + 2\lambda_1 v_2^2 - \frac{1}{2}m_{\text{Z}}^2 \\
m_2^2 &= -|\mu|^2 + 2\lambda_1 v_1^2 - \frac{1}{2}m_{\text{Z}}^2 \\
m_{12}^2 &= \frac{1}{2}v_1 v_2(4\lambda_1 - g^2 - g'^2)
\end{aligned} \tag{1.48}$$

Using these results in the mass eigenvalue and mixing angle formulas given in Section 1.4.1 and letting m_{A} and $\tan\beta$ be the free parameters, one finds:

$$m_{\text{H}^\pm}^2 = m_{\text{A}}^2 + m_{\text{W}}^2 \tag{1.49}$$

$$m_{\text{H}^0,\text{h}^0}^2 = \frac{1}{2}\left[m_{\text{A}}^2 + m_{\text{Z}}^2 \pm \sqrt{(m_{\text{A}}^2 + m_{\text{Z}}^2)^2 - 4m_{\text{Z}}^2 m_{\text{A}}^2\cos^2 2\beta}\right] \tag{1.50}$$

$$\tan 2\alpha = \tan 2\beta\left(\frac{m_{\text{H}^0}^2 + m_{\text{h}}^2}{m_{\text{A}}^2 - m_{\text{Z}}^2}\right) \tag{1.51}$$

These tree-level mass relations make a striking prediction, namely that the mass of the lightest CP-even neutral Higgs boson should be less than m_{Z}, guaranteeing a discovery at LEP or LEP2. However, this upper bound weakens when radiative corrections are taken into account.

1.5.2 Radiative Corrections to the MSSM Higgs Sector

Radiative corrections up to leading two-loop order for the Higgs masses and mixing angles have been approached in a number of ways, such as renormalization-group improvement of the one-loop effective potential [13, 14], two-loop effective potential calculations [15, 16], and full Feynman-diagrammatic approaches [17, 18]. Each comes with its own set of simplifying assumptions, renormalization schemes, etc.; the results of the various approaches have been compared (for example, in [19]) and have been found to agree quite well. The reader is referred to the sources for the details; we quote some relevant general results here.

The upper bound on $m_{\rm h}$ is always obtained when $m_{\rm A} \gg m_{\rm Z}$, in which case the effective potential approach gives a convenient analytical expression for $m_{\rm h}$:

$$\begin{aligned} m_{\rm h}^2 &= m_{\rm Z}^2 \cos^2 2\beta + \frac{3\alpha}{4\pi \sin^2\theta_W} \frac{m_{\rm t}^4}{m_{\rm W}^2} \left[\ln \frac{m_{\tilde{\rm t}_1}^2 m_{\tilde{\rm t}_2}^2}{m_{\rm t}^2} + \right. \\ &\quad \left(\frac{m_{\tilde{\rm t}_2}^2 - m_{\tilde{\rm t}_1}^2}{4m_{\rm t}^2} \sin^2 2\theta_{\tilde{\rm t}} \right)^2 \left(2 - \frac{m_{\tilde{\rm t}_2}^2 + m_{\tilde{\rm t}_1}^2}{(m_{\tilde{\rm t}_2}^2 - m_{\tilde{\rm t}_1}^2)} \ln \frac{m_{\tilde{\rm t}_2}^2}{m_{\tilde{\rm t}_1}^2} \right) + \\ &\quad \left. \frac{m_{\tilde{\rm t}_2}^2 - m_{\tilde{\rm t}_1}^2}{2m_{\rm t}^2} \sin^2 2\theta_{\tilde{\rm t}} \ln \frac{m_{\tilde{\rm t}_2}^2}{m_{\tilde{\rm t}_1}^2} \right] \end{aligned} \tag{1.52}$$

The stop masses $m_{\tilde{\rm t}_1}$ and $m_{\tilde{\rm t}_2}$ are obtained by diagonalizing the following mass-squared matrix in the $(\tilde{\rm t}_L, \tilde{\rm t}_R)$ basis:

$$\begin{pmatrix} m_{\tilde{\rm t}_L}^2 + m_{\rm t}^2 + \cos 2\beta(\frac{1}{2} - \frac{2}{3}\sin^2\theta_W) m_{\rm Z}^2 & m_{\rm t}(A_t - \mu \cot\beta) \\ m_{\rm t}(A_t - \mu\cot\beta) & m_{\tilde{\rm t}_R}^2 + m_{\rm t}^2 - \frac{1}{3}\cos 2\beta \sin^2\theta_W m_{\rm Z}^2 \end{pmatrix}$$

where A_t is the trilinear Higgs-stop coupling. The stop-mixing angle $\theta_{\tilde{\rm t}}$ is defined as

$$\sin 2\theta_{\tilde{\rm t}} = \frac{2m_{\rm t}(A_t - \mu \cot\beta)}{m_{\tilde{\rm t}_2}^2 m_{\tilde{\rm t}_1}^2} \tag{1.53}$$

From Equation 1.52 it is seen that $m_{\rm h}$ depends crucially on the top mass, the stop masses, and the mixing in the stop sector (in addition to the tree-level dependence on $m_{\rm A}$ and $\tan\beta$). The stop masses and mixing will depend on the mechanism of

electroweak symmetry breaking, which is a matter that is only open to speculation at this time. With no organizing principle, a completely general MSSM contains 105 free parameters determining the masses, mixing angles, and phases of the SUSY particles. In order to reduce this parameter space to make some actual predictions, one typically works within the "supergravity-inspired" constrained MSSM (CMSSM). In this scenario the entire low-energy behavior of the MSSM can be described by specifying five parameters at the GUT scale:[1]

1. A common gaugino mass $m_{1/2}$
2. A common sfermion mass m_0
3. A common trilinear Higgs-sfermion coupling A
4. The SUSY Higgs mass parameter μ (see Equation 1.44)
5. The Higgs VEV ratio $\tan\beta$

The renormalization group equations are then used to determine the spectrum of the MSSM at the electroweak scale.

Typically when calculating Higgs masses one assumes the stops and sbottoms have a similar mass m_{SUSY} (also called m_{S}), or one can specify the masses of the left-up, right-up, and right-down squarks separately with m_Q, m_U, and m_D. Stop mixing is usually parameterized with $X_t = A_t - \mu\cot\beta$. Figures 1.9 and 1.10 show m_{h} for various values of these quantities in the CMSSM. One can see that the upper bound on m_{h} shifts to about 135 GeV/c^2 when radiative corrections are taken into account, and that this upper bound is realized for large values of $\tan\beta$, m_{A}, and stop mixing.

1.5.3 MSSM Higgs Phenomenology

The couplings of the MSSM Higgses to fermions and gauge bosons can still be expressed with the α- and β-dependent rescaling factors of a general Type II 2HDM

[1]One of the most intriguing features of SUSY is that the extra particle content leads to a unification of the running gauge coupling constants at an energy scale $Q \sim 10^{16}$ GeV, called the GUT scale.

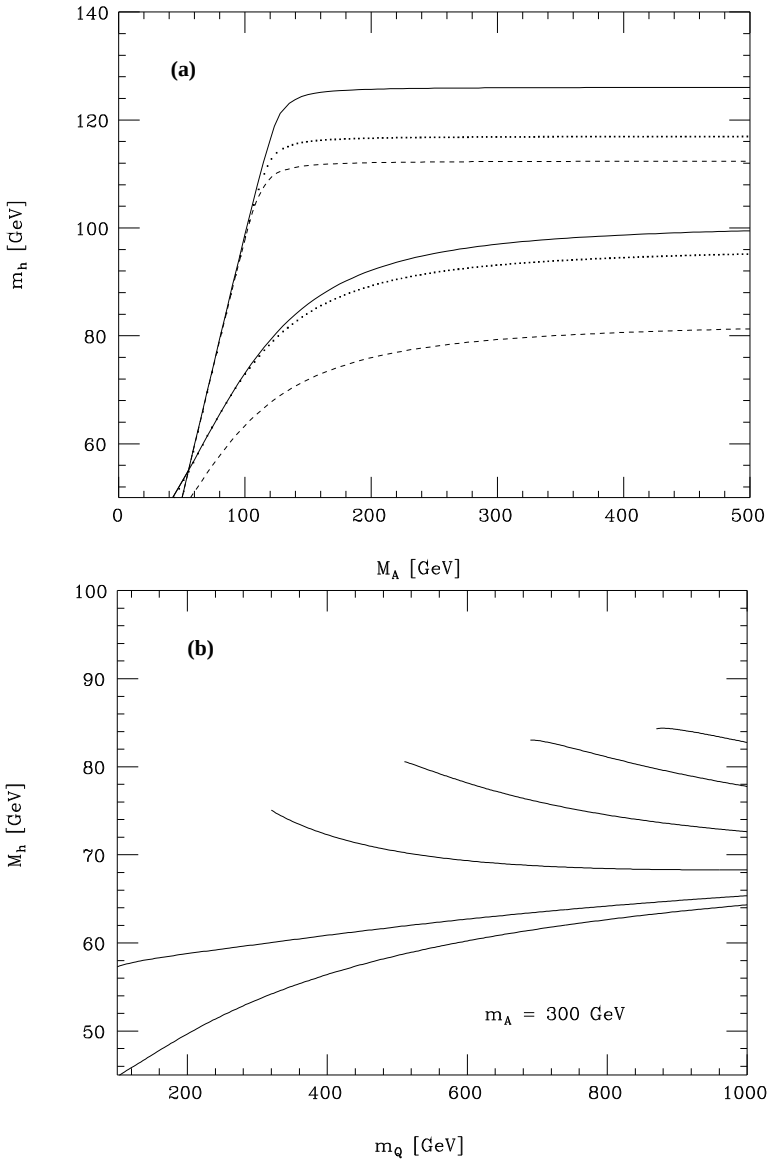

Figure 1.9: $m_{\rm h}$ as a function of $m_{\rm A}$ is shown in (a) for $m_{\rm SUSY} = 1$ TeV/c^2. The dashed, dotted, and solid lines are for minimal, intermediate, and maximal stop mixing, respectively. The lower (upper) set of curves are obtained for $\tan\beta = 1.6$ (15). $m_{\rm h}$ as a function of m_Q is shown in (b) for $\tan\beta = 1.6$, $\mu = A_b = 0$, $m_U = m_D = 1$ TeV/c^2, and $m_{\rm A} = 300$ GeV/c^2. The different curves, starting from the lowest one and working up, are for $A_t = 0$, 0.2, 0.4, 0.6, 0.8, and 1 TeV/c^2. Both plots use $m_{\rm t} = 175$ GeV/c^2 [20].

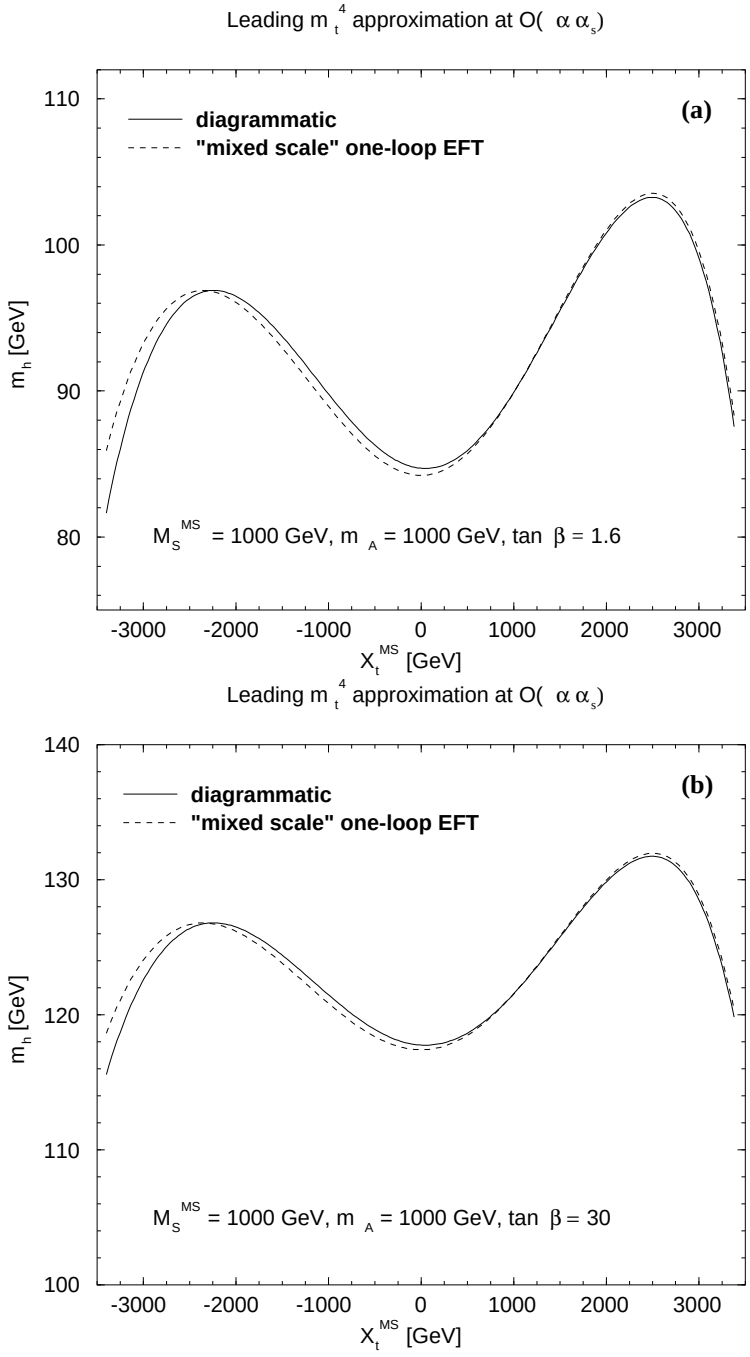

Figure 1.10: $m_{\rm h}$ as a function of the stop-mixing parameter X_t for (a) $\tan\beta = 1.6$ and (b) $\tan\beta = 30$. Results are shown for both the effective potential calculation (dotted line) and the two-loop Feynman diagrammatic approach (solid line) [19].

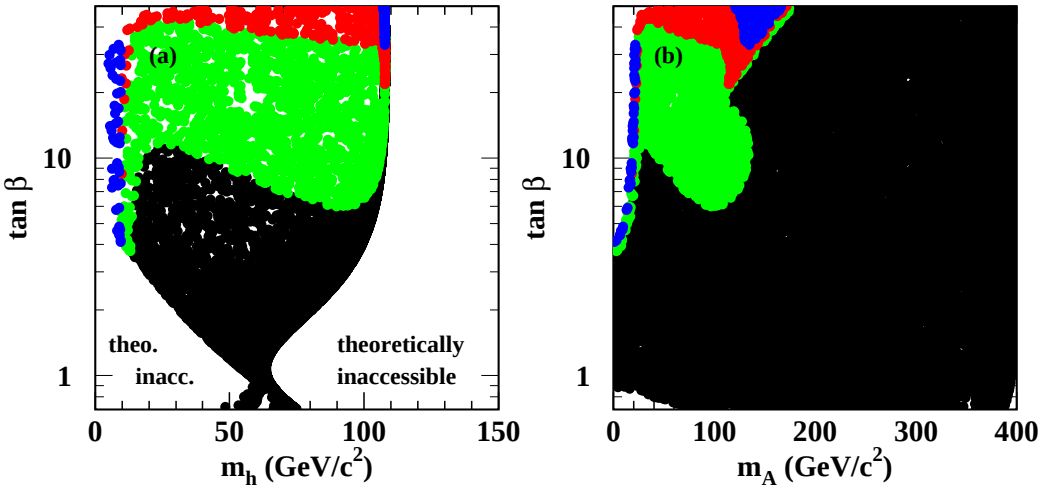

Figure 1.11: BR($h^0 \to \tau^+\tau^-$) for a particular set of MSSM parameters (see footnote) in the (a) (m_h, $\tan\beta$) projection and (b) (m_A, $\tan\beta$) projection. The black area corresponds to BR < 0.1, the green (light grey) area to $0.1 <$ BR < 0.2, the red (medium grey) area to $0.2 <$ BR < 0.3, and the blue (dark grey) area to BR > 0.3. The small white patches are due to the granularity of the scan over m_A and $\tan\beta$.

given in Section 1.4.2. Recall, however, that α is no longer a free parameter. In practice α is determined via Equation 1.32 after computing the radiative corrections to the quartic Higgs self-couplings of Equation 1.24. Therefore the phenomenology of the MSSM Higgs sector, like the Higgs masses, will depend on SUSY-breaking parameters; we therefore conclude with some general "rules of thumb" for the MSSM Higgses.

Branching ratios for the h^0 and A^0 are typically similar to the SM Higgs branching ratios. However, it is interesting to note that some regions of the CMSSM parameter space correspond to significantly larger $h^0 \to \tau^+\tau^-$ branching ratios. This is shown in Figure 1.11; for a particular choice of parameters[2] BR($h^0 \to \tau^+\tau^-$) can be as large as 50% for large values of $\tan\beta$.

[2] $m_{\mathrm{SUSY}} = 400$ GeV/c^2, $\mu = 1$ TeV/c^2, M_2 (the SU(2) gaugino mass parameter) $= 400$ GeV/c^2, $m_{\tilde{g}} = 200$ GeV/c^2, $X_t = -300$ GeV/c^2, $A_b = A_t$

Following the discussion of Section 1.4.2, the two main production mechanisms for neutral MSSM Higgs bosons are Higgsstrahlung (h^0Z^0) and pair-production (h^0A^0), which exhibit a degree of complementarity. In the MSSM, the Higgsstrahlung process dominates for small (~ 1.5) values of $\tan\beta$. In the limit of large m_A, in fact, the couplings of the h^0 are nearly identical to those of H^0_{SM} and the phenomenology is entirely SM-like. For large (~ 30) values of $\tan\beta$ and a kinematically accessible A^0, the pair-production process dominates and over most of the MSSM parameter space the h^0 and A^0 have SM-like decays. This leads to the production of $b\bar{b}b\bar{b}$ and $b\bar{b}\tau^+\tau^-$ final states, thus motivating search topologies similar to the SM tau and 4-jet channels.

CHAPTER 2
THE OPAL DETECTOR AT LEP

In this chapter the experimental set-up used to search for Higgs bosons is described, along with the data samples used for this thesis. Many items in this chapter are described in detail elsewhere; the reader will be referred to these sources whenever appropriate.

2.1 The LEP Collider

CERN's Large Electron-Positron (LEP) collider [21] is a 27 km underground e^+e^- storage ring straddling the French border near Geneva, Switzerland. Its construction and commissioning was completed in 1989, which was followed by several years of data-taking at center-of-mass energies ($\sqrt{s}$) at and around the Z^0 resonance, allowing for high-precision tests of the Standard Model (cf. Section 1.1.2). The LEP1 era (as it was called in retrospect) was followed by an upgrade to center-of-mass energies near 133 GeV (LEP1.5) in 1995, and then to $\sqrt{s} = 161$ GeV in 1996, beginning the LEP2 era. Since 1996 the LEP energy has been increased each year, ultimately to 209 GeV in 2000, its last operating year. Here the machine's 1998 configuration ($\sqrt{s} = 189$ GeV) will be described, as this provided the bulk of the data used in this thesis.

2.1.1 Injection into LEP

As a cost-saving measure, CERN's older accelerator complex is used as a LEP injection system, the scheme of which is shown in Figure 2.1. Electrons are provided by pulses from an electron gun and accelerated in the LEP Injection Linacs (LIL). In this phase the electrons are first brought to 200 MeV by a linear accelerator, at which point some are brought into collision with a tungsten target to produce positrons

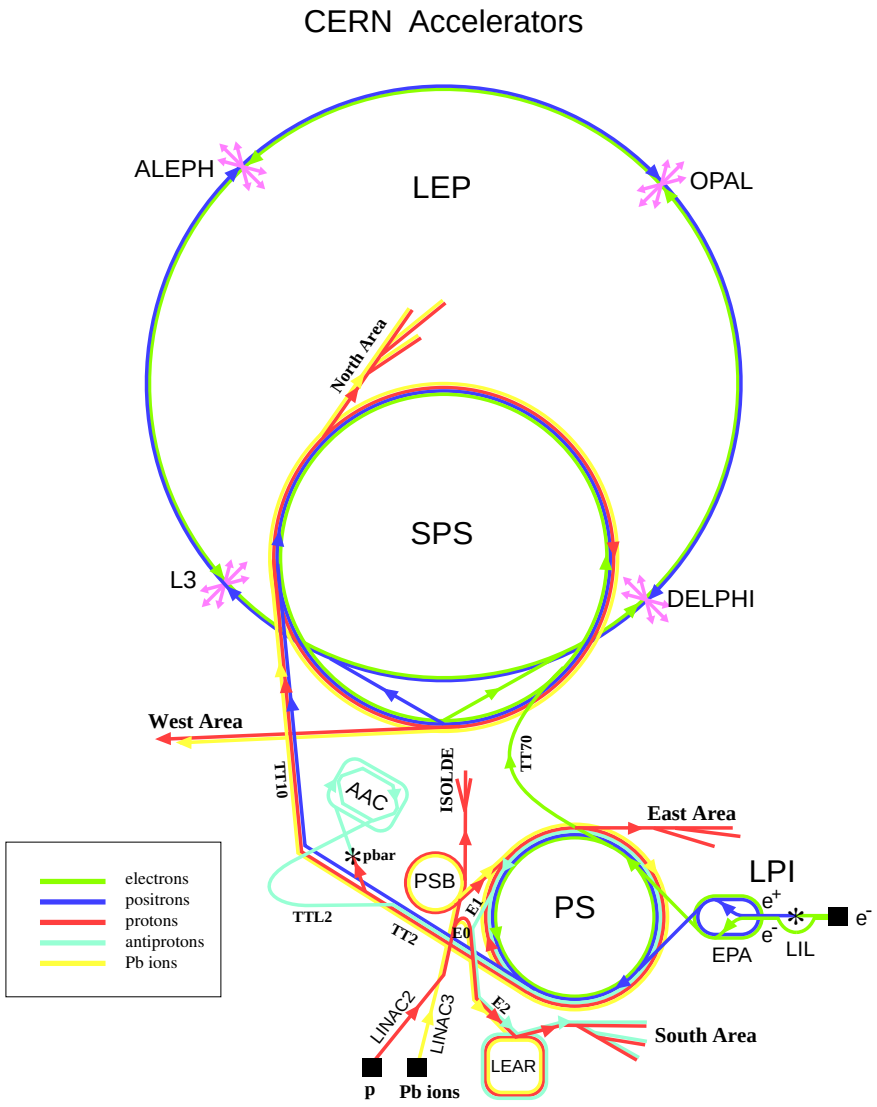

Figure 2.1: The CERN accelerator complex.

via pair-production. The electrons and positrons are then brought to 600 MeV by a second linear accelerator and stored in the Electron-Positron Accumulator (EPA).

The leptons in the EPA are then injected into CERN's Proton Synchrotron (PS), a 628 m circular accelerator operating here as a 3.5 GeV e^+e^- synchrotron. The next phase of injection is into the Super Proton Synchrotron (SPS), another circular accelerator 6 km long, which brings the electrons and positrons to 22 GeV for injection into LEP.

2.1.2 Acceleration and Collision in LEP

In 1998 the LEP accelerating system consisted of 272 superconducting RF cavities (256 were niobium-coated copper, 16 were pure niobium) and 48 conventional copper RF cavities. The superconducting cavities typically operated with field gradients of 6 MV/m, with a total RF voltage of 2870 MV per revolution. Dipole magnets are used to bend the electron and positron beams into their circular trajectories within an evacuated beam pipe, with beam focusing provided by quadrupole and sextupole magnets. The 22 GeV electrons and positrons from the SPS are injected into LEP as four "bunches" each, which are then accelerated to a physics energy of 94.5 GeV per beam. At the four LEP interaction points (housing the LEP detectors) the beams are then squeezed by means of superconducting quadrupole magnets into a spot with transverse dimensions of about 20 μm and 110 μm in the vertical and horizontal planes, respectively. This allows for peak instantaneous luminosities of about 10^{32} cm^{-2} s^{-1}.

2.2 The OPAL Detector

OPAL[1] is a large general-purpose particle detector with nearly complete 4π solid angle coverage. It provides charged-particle tracking, electromagnetic and hadronic calorimetry, and muon detection via an integrated system of subdetectors, shown in Figure 2.2. Here the subdetectors most relevant to the Higgs search are described;

[1]Omni-Purpose Apparatus at LEP

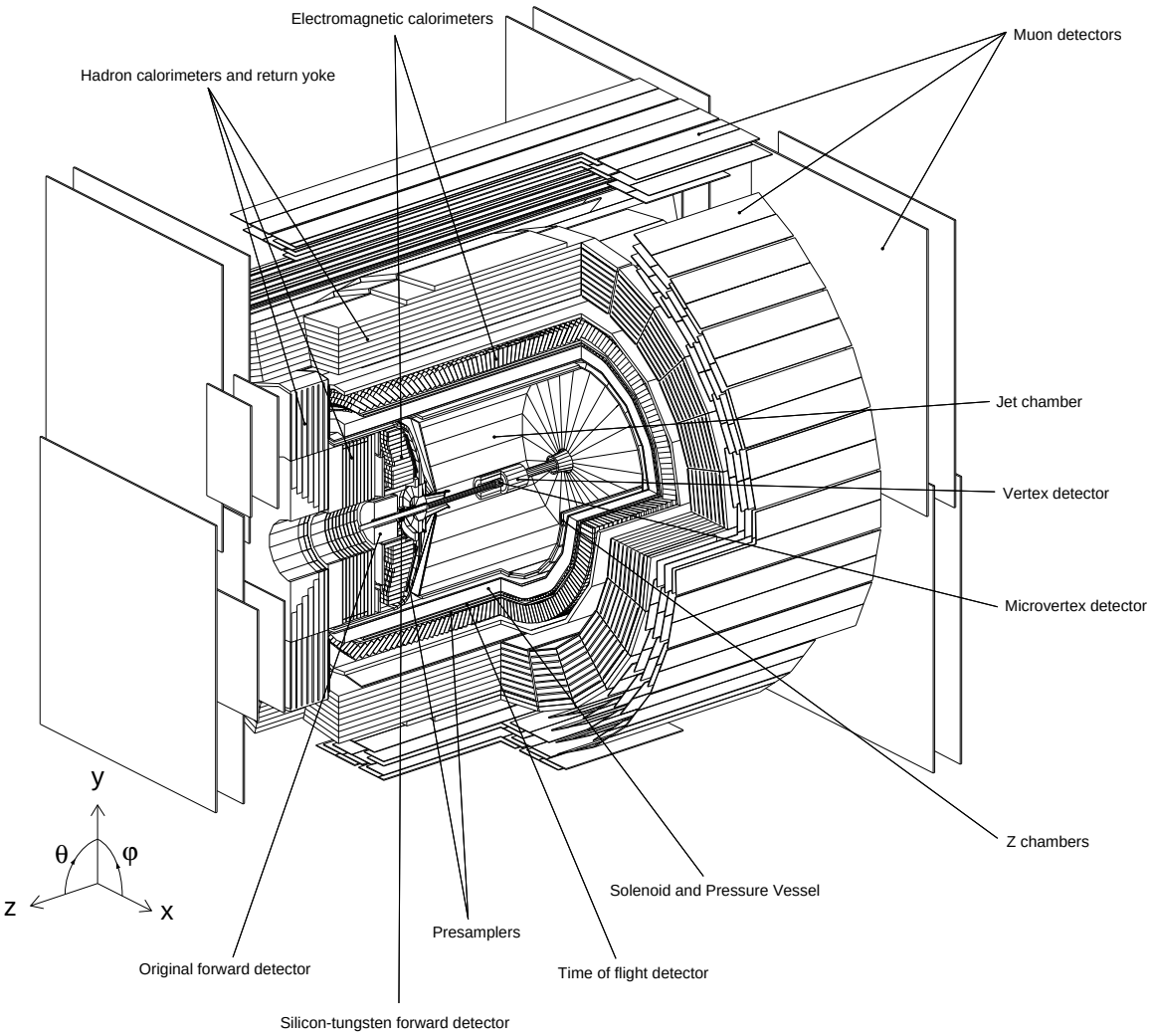

Figure 2.2: The OPAL detector.

for a complete description of OPAL, see [22].

2.2.1 The Silicon Microvertex Detector

Due to the relatively long lifetimes of B hadrons (typically about 1.5 ps), one can efficiently identify the b-quark jets in Higgs decay by searching for secondary vertices significantly displaced from the interaction point (or "primary vertex"). This requires precision tracking of charged particles, and therefore one of the most important sub-detectors for the Higgs search is the silicon microvertex detector, or SI.

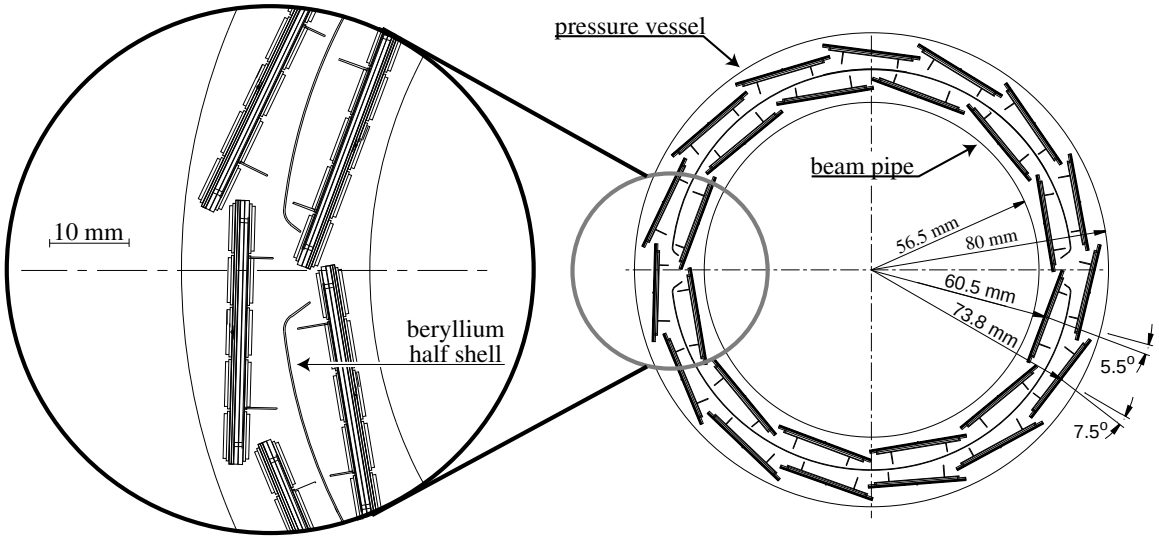

Figure 2.3: End-on view of the silicon microvertex detector showing the two-layer ladder configuration. The important radial dimensions are indicated. The magnified view on the left provides more structural details and illustrates the tight mechanical tolerances.

The microvertex detector was first installed in 1991 and upgraded to its present configuration in 1995 [23]. It consists of two concentric layers of "ladders" arranged in the space between the the beam pipe and wire chamber pressure vessel as shown in Figure 2.3. Each ladder consists of five pairs of back-to-back 60×33 mm^2 single-sided FoxFET silicon-strip wafers [24], with the inner (outer) wafer oriented for z (ϕ) coordinate readout.[2] The length of the ladders provides two-layer coverage for $|\cos\theta| < 0.89$; the azimuthal active acceptance is 97%.

When a charged particle traverses the detector, the charge collected on a strip is read out as a SI "hit," with typical signal-to-noise ratios of about 20–30:1. The detector operates at a high efficiency; 97% of minimum ionizing particles traversing the active area of the SI ladders have at least one hit in SI matched to their reconstructed tracks in the central wire chambers. Figure 2.4 shows the two-SI-hit matching efficiency for $e^+e^- \to \mu^+\mu^-$ events, which is seen to be 93% for nearly the entire $\cos\theta$

[2]OPAL uses a right-handed coordinate system where the $+z$ direction is along the electron beam and where $+x$ points to the center of the LEP ring. The polar angle, θ, is defined with respect to the $+z$ direction and the azimuthal angle, ϕ, with respect to the horizontal, $+x$ direction.

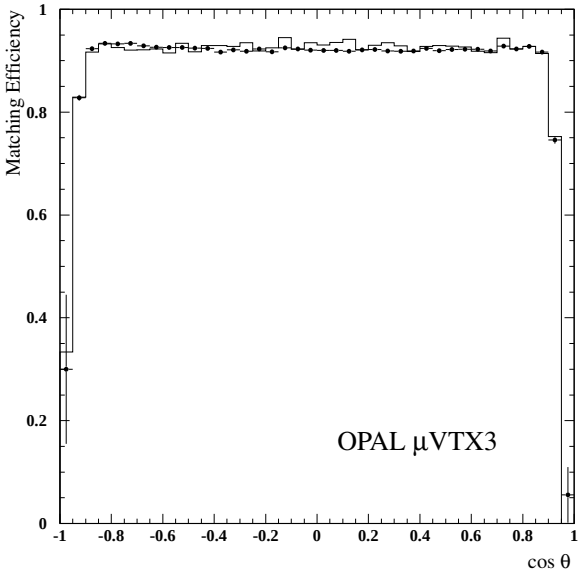

Figure 2.4: Efficiency for two SI hits to match to tracks in the central wire chambers as a function of $\cos\theta$ for $e^+e^- \to \mu^+\mu^-$ events. The points are the experimental data and the histogram is the efficiency predicted from simulation.

range.

A precise knowledge of the detector alignment is crucial in order to obtain the best possible hit position resolution. Alignment constants, both global (position of SI with respect to OPAL) and local (position of ladders and wafers with respect to each other), are determined using LEP2 charged particle tracks. The constants are adjusted iteratively to minimize the residuals of the SI hits to fitted tracks. In this way the ultimate position uncertainty due to alignment is estimated to be about 8 to 10 μm in ϕ and 10 to 12 μm in z. The implication of this for physics is shown in Figure 2.5, where distributions of d_0 and z_0, the track impact parameters with respect to the primary vertex in $r-\phi$ and z, respectively, are shown for $e^+e^- \to e^+e^-(\mu^+\mu^-)$ events. The resolution is 18 μm on d_0 and 24 μm on z_0.

2.2.2 The Central Tracking System

The charged particle tracking system in OPAL is divided into (working outward from the silicon detector) a small central vertex detector, a large-volume jet chamber, and

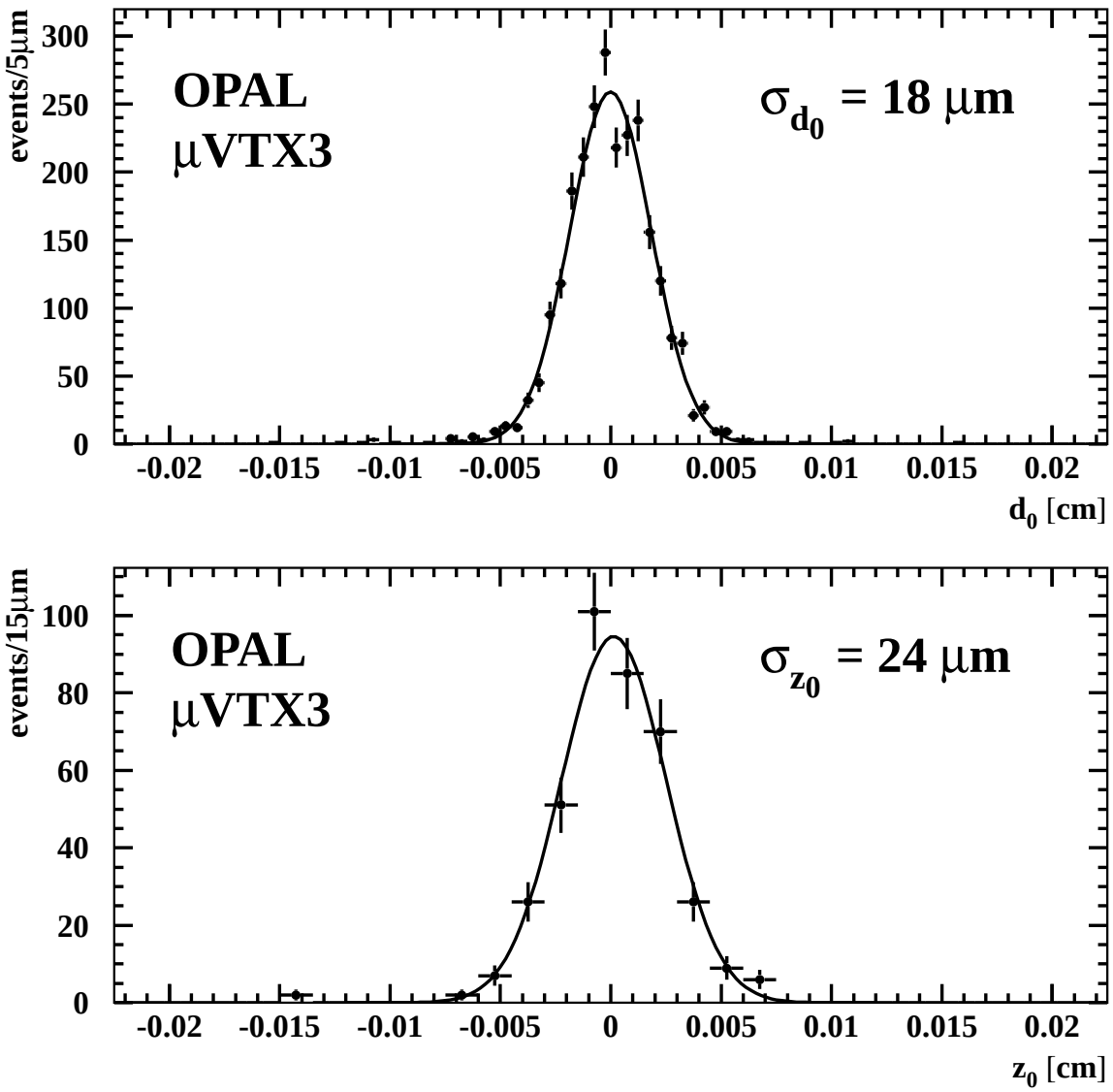

Figure 2.5: Impact parameter distributions in the plane perpendicular to the beam axis (d_0) and in the direction of the beam axis (z_0) for $e^+e^- \to e^+e^-(\mu^+\mu^-)$ events. The points are the experimental data and the curve is a Gaussian fit.

a set of z-chambers (see Figure 2.2). The system operates within a 0.435 T magnetic field (provided by a surrounding conventional solenoid magnet) to measure particles' momenta and electric-charge signs. All three detectors are of the drift-chamber type and share a common argon/methane/isobutane gas mixture at a pressure of 4 bar.

The Central Vertex Detector (CV)

The original intent of the CV was to provide precision tracking, with spatial resolutions of about 50 μm. However, the addition of the silicon microvertex detector "in front" of the CV superseded this function, and now the CV's *raison d'être* is to provide intermediate tracking points between the main jet chamber and the silicon, ensuring the high matching efficiency seen in Figure 2.4.

The 1-m-long CV has a cylindrical two-layer structure consisting of an inner axial layer (extending from $r = 88$ mm to $r = 175$ mm) and an outer stereo layer ($r = 175$ mm to $r = 235$ mm). Each layer consists of 36 cells in ϕ, defined by alternating radial planes of cathode and anode wires. The axial-layer anode planes contain 12 sense wires running parallel to the beam direction with a radial spacing of 5.3 mm, whereas the stereo-layer anode planes contain 6 sense wires at a stereo angle of 4° with a 5 mm spacing. Thus a maximum of 18 CV hits can be used to interpolate between jet chamber tracks and silicon hits.

The Central Jet Chamber (CJ)

The main particle tracker is the 4-m-long cylindrical central jet chamber, with an outer (inner) diameter of 3.7 (0.5) m. The CJ volume is divided into 24 sectors in ϕ, each containing one radial plane of 159 anode sense wires and bounded on each side by planes of cathode wires. The potential difference between the cathode and anode planes varies radially from 2.4 kV to 24 kV and the maximum drift distance to the sense wires varies from 3 cm at the innermost wire to 25 cm at the outermost wire.

The maximum of 159 possible tracking points covers the range $43° < \theta < 137°$, and at least 8 points per track are obtained over 98% of the full 4π solid angle. For each point an $r - \phi$ position is determined from the wire position and the drift time,

and the amount of collected charge is sampled at each wire to provide a measurement of the dE/dx loss for the particle as it traverses the chamber gas.

A circle fit in $r-\phi$ determines the radius of curvature of the reconstructed track and therefore the magnitude of the charged-particle p_T. The direction of curvature determines the sign of electric charge. In the central region of the detector, the momentum resolution (driven by the radius-of-curvature uncertainty) can be described by

$$\frac{\sigma_p}{p} \approx \frac{\sigma_{p_T}}{p_T} = \sqrt{0.02^2 + (0.0015 p_T)^2} \tag{2.1}$$

with p_T in GeV/c.

The Central Z Chambers (CZ)

The jet-chamber design of the CJ does not allow for any precise measurement of the z coordinate of a sense-wire hit; the best that can be done is a rough estimate based on the ratio of the amounts of charge collected at both ends of the wire ("charge division"). The CZ serves to make up for this by surrounding the CJ with 24 planar drift chambers of length 4 m, width 50 cm, and thickness 59 mm, each containing eight anode sense planes. Each plane consists of six sense wires running along the ϕ direction at increasing radii. This allows for a drift-time measurement of the z coordinate with a resolution of about 1 mm, along with a rough charge-division measurement of the ϕ coordinate to facilitate matching with the CJ track. An accurate measurement of z is important because the invariant mass reconstructed from an ensemble of particles is quite sensitive to the polar angles of the particles.

2.2.3 Calorimetry

Outside the solenoid coil is the OPAL calorimetry system. An electromagnetic calorimeter and presampler provide energy measurements for electrons, positrons and photons; strongly-interacting particles continue on and are absorbed in a hadronic calorimeter.

The Electromagnetic Calorimeter (EB and EE)

The electromagnetic calorimeter is divided into three detectors, the barrel calorimeter (EB), which covers $|\cos\theta| < 0.82$, and two endcap calorimeters (EE) covering $0.81 < |\cos\theta| < 0.98$. Both detectors use a large array of lead-glass blocks of cross-sectional area $\approx 10 \times 10$ cm^2 and are 24.6 radiation lengths long. The EB blocks are arranged in a projective geometry such that their long axes point approximately to the interaction region, thus keeping electromagnetic showers contained in a minimum number of blocks. Endcap blocks are arranged parallel to the beam due to space constraints. The light produced in the lead glass by the electromagnetic shower is collected by phototubes and phototriodes and translated into an energy deposition via calibration studies performed in an electron test beam. The excellent intrinsic energy resolution of the lead glass ($\sigma_E/E \approx 5\%/\sqrt{E}$) is degraded somewhat by the presence of about two radiation lengths of material in front of the calorimeter (mostly due to the solenoid coil), but this can be recovered somewhat by the use of shower presamplers in between the coil and calorimeter. The summed energies of adjacent lead glass blocks are reconstructed as calorimeter "clusters" offline.

The Hadronic Calorimeter (HB, HE, and HP)

The iron of the magnetic flux return yoke provides 4 or more interaction lengths of material over 97% of the full solid angle. Gaps in between the layers of iron are instrumented with limited streamer tubes and high-gain multiwire chambers with pad and strip readout. The layers of pads form calorimeter towers with a linear energy response calibrated in a pion test beam. The energy resolution is $\sigma_E/E \approx 120\%/\sqrt{E}$, limited mostly by the 2.2 interaction lengths of material in front of the calorimeter. The calorimeter is divided into barrel (HB), endcap (HE), and poletip (HP) detectors, but the differences between them are largely geometrical.

2.2.4 Muon Detectors

The outermost set of detectors in OPAL is used for muon identification. As a particle must traverse about 1.3 m of iron equivalent over most of the solid angle to reach the muon detectors, in general only muons will not be absorbed in transit. The muon detectors consist of 4 layers of wire chambers in the barrel region (MB, $|\cos\theta| < 0.68$) and two layers of streamer tubes in the endcap region (ME, $0.67 < |\cos\theta| < 0.98$). Muon identification relies on extrapolating hits in the muon chambers back to the track in the central tracking system with the aid of strip hits in the hadron calorimeter. For isolated muons above 3 GeV and within the 93% of solid angle covered by the muon detectors, the identification efficiency is nearly 100%. The probability of a 5 GeV pion being misidentified as muon (either by traversing the hadron calorimeter without interacting, or by secondary particles from a hadron interaction escaping the calorimeter) is less than 1%.

2.2.5 The Silicon-Tungsten Luminometer

To determine the absolute amounts of Higgs signal and background events expected the luminosity delivered to OPAL must be determined. This is done by using two small cylindrical electromagnetic calorimeters encircling the beam pipe at approximately ± 2.5 m from the nominal interaction point. The calorimeters are composed of 19 layers of silicon sampling wafers interleaved with 18 layers of tungsten plates. This silicon-tungsten calorimeter (SW) has an angular acceptance extending from 25 to 58 mrad and is therefore well-suited for detecting low-angle Bhabha scattering ($e^+e^- \to e^+e^-$, mostly via the t-channel exchange of a photon). By counting the number of beam-energy electrons seen in SW and dividing by the Bhabha cross section corrected for detector acceptance, the luminosity can be determined to better than 0.1%.[3]

[3]Such fantastic precision is of course not necessary for a search; the SW was designed to improve the precision of the Z^0 lineshape measurement at LEP1.

Years	$\sqrt{s}$ (GeV)	Total luminosity (pb^{-1})
1989-95	$\approx m_{\mathrm{Z}}$	170
1995, 1997	130, 136	11
1996	161	10
1996	172	10
1997	183	57
1998	189	187

Table 2.1: OPAL data samples.

2.3 Data Samples

Table 2.1 shows the amount and type of data collected by OPAL since its turn-on in 1989. The results of this thesis are based on 168.7 pb^{-1} collected at $\sqrt{s} = 189$ GeV in 1998.[4] As will be discussed in Chapter 5, however, data taken at lower $\sqrt{s}$ are useful to extend the reach of the Higgs search.

The SM processes which provide the background to Higgs searches are simulated using a number of Monte Carlo generators, with typically more than 50 times the statistics of the collected data. The generators used are PYTHIA [25], BHWIDE [26], and KORALZ [27] for the two-fermion processes $(\mathrm{Z}/\gamma)^* \to \mathrm{q\bar{q}}(\gamma)$, $(\mathrm{Z}/\gamma)^* \to \mathrm{e^+e^-}(\gamma)$, and $(\mathrm{Z}/\gamma)^* \to \mu^+\mu^-(\gamma), \tau^+\tau^-(\gamma)$ respectively, grc4f [28] for four-fermion processes, and PHOJET [29], HERWIG [30], and Vermaseren [31] for hadronic and leptonic two-photon processes ($\gamma\gamma$). The hadronization process is simulated with JETSET [25] with parameters described in [32]. The cluster fragmentation model in HERWIG is used to study the uncertainties due to fragmentation and hadronization. EXCALIBUR [33] is used as a cross-check of the grc4f prediction of the four-fermion background. Higgs production is modelled using the HZHA [34] generator for a wide range of Higgs masses, with 1000 events per mass point.

For each Monte Carlo sample, the detector response to the generated particles is simulated in full detail by GEANT [35]. As an example of the reliability of the

[4]This is less than the 1998 collected luminosity shown in Table 2.1 because only the subset of data in which all the subdetectors described in this chapter were fully operational was used.

SM background Monte Carlo predictions, Figures 2.6 and 2.7 show comparisons with data for two- and four-fermion processes, respectively. Figure 2.6 shows distributions of $\sqrt{s'}$, the effective center-of-mass energy of the e^+e^- system after radiation of one or more photons from the incoming electron and/or positron (called "initial-state radiation" or ISR). Figure 2.7 shows the reconstructed $W^{\pm}$ mass in four W^+W^- decay channels, including the contributions from non-W^+W^- events. In both figures data and MC are seen to agree very well.

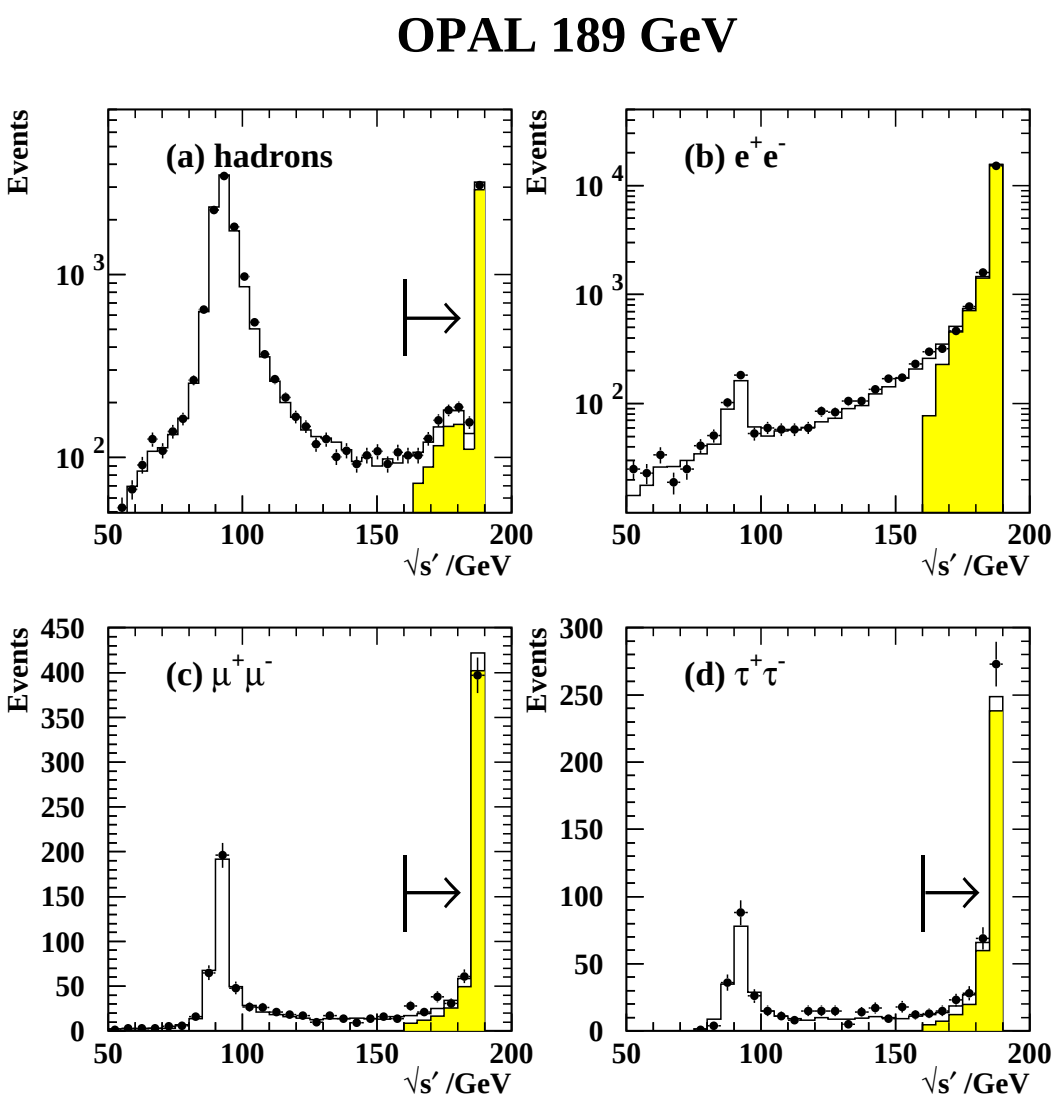

Figure 2.6: Distributions of the effective center-of-mass energy $\sqrt{s'}$ in two-fermion events for (a) hadronic events, (b) electron pairs, (c) muon pairs, and (d) tau pairs. The points are data and the histograms are MC predictions. The shaded histograms in (a), (c), and (d) represent the contribution from events with $s'/s > 0.7225$, also indicated by the arrows. The shaded histogram in (b) is the contribution from e^+e^- pairs with an acollinearity angle greater than 10°.

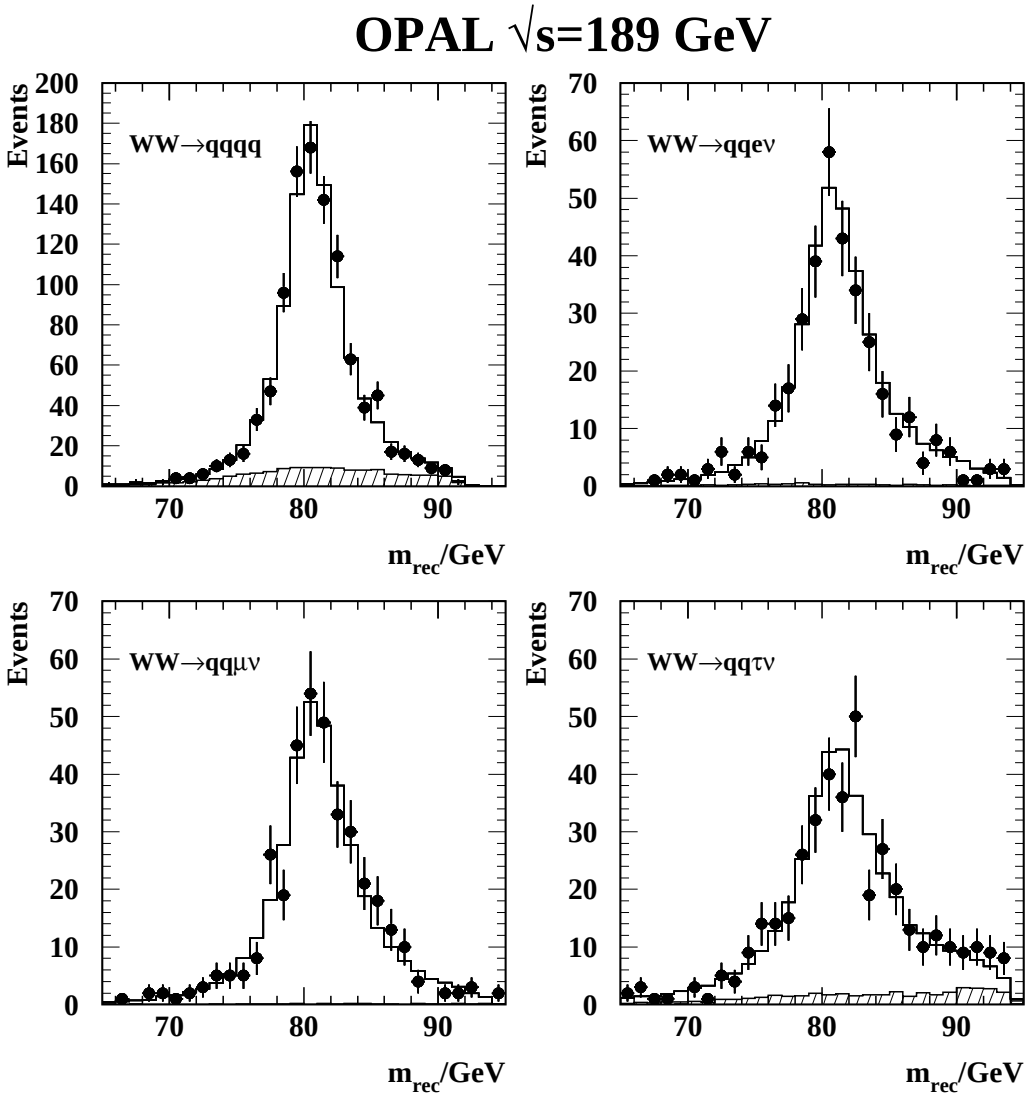

Figure 2.7: Distribution of the $W^{\pm}$ mass reconstructed in four W^+W^- decay channels. The points are data and the histograms are the MC predictions. The shaded histograms represent the contribution from non-W^+W^- events.

CHAPTER 3
THE TAU ID NEURAL NETWORK

The two tau leptons in the $q\bar{q}\tau^+\tau^-$ final state provide a distinctive signature for neutral Higgs boson production. Additionally, taus produced in association with hadron jets make up an important subset of more general search topologies at LEP2. Some examples include charged Higgs boson production ($e^+e^- \to H^+H^- \to q\bar{q}'\tau\nu_\tau$) and stau production ($e^+e^- \to \tilde{\tau}^+\tilde{\tau}^- \to \tau^+\tilde{\chi}_1^0\tau^-\tilde{\chi}_1^0$) with subsequent R-parity violating $\tilde{\chi}_1^0 \to \ell qq$ decays. Bearing this in mind, the tau identification algorithm described in this chapter was designed to be generically applicable to any search for topologies with *high-energy taus* ($E_\tau \gtrsim 10$ GeV) in *high-multiplicity environments*.

Before discussing the tau ID itself, it is useful to first review some tau decay properties in order to understand the approach taken. The tau lifetime is approximately 290 fs, meaning that the tau decays well before it reaches the inner radius of the OPAL tracking system. Therefore what is actually observed in the detector are the visible tau decay products. The most important tau decay modes are listed in Table 3.1 along with their branching ratios. Nearly all tau decays can be classified as either "one-prong" or "three-prong," referring to the number of charged particles in the decay and hence the number of tracks seen in the detector. Furthermore, the one-prong decays can be subclassified as either "hadronic," where the charged particle is a pion or kaon, or "leptonic," where the charged particle is an electron or muon.

In addition to the one- or three-track topology, tau decays are characterized by the presence of at least one neutrino, which escapes OPAL undetected and gives rise to missing energy. Finally we note that except for the first decay listed in Table 3.1, taus undergo many-body decays, resulting in softer momentum spectra for the final-state particles.

Searching for taus produced in association with jets presents a particular challenge because the hadronic system can result in one- or three-track clusters that can fake

decay mode	branching ratio
"One-prong"	84.7%
$\tau^{\pm} \to h^{\pm}\nu_{\tau}$	11.8%
$\tau^{\pm} \to h^{\pm}X^{0}\nu_{\tau}$	36.9%
$\tau^{\pm} \to \ell^{\pm}\nu_{\ell}\nu_{\tau}$	35.2%
"Three-prong"	15.2%
$\tau^{\pm} \to h^{\pm}h^{\pm}h^{\mp}\nu_{\tau}$	10.0%
$\tau^{\pm} \to h^{\pm}h^{\pm}h^{\mp}X^{0}\nu_{\tau}$	5.2%

Table 3.1: Tau decay modes and branching ratios (from [36]). $h^{\pm}$ refers to either $\pi^{\pm}$ or $K^{\pm}$, X^{0} refers to any number (> 0) of neutral hadrons, and ℓ refers to either an electron or muon.

a tau. For example, a stray jet fragmentation track may fake a one-prong tau, or a low-multiplicity jet from gluon radiation may fake a three-prong tau. The main handle for realizing these as fakes is that they will tend to be less isolated from the hadronic system than real taus. In addition, jet fragmentation tracks arise from charged particles that are typically less energetic than the decay products of a high-energy tau.

In order to maintain high efficiency, no attempt is made to separate leptonically decaying taus from prompt electrons or muons. This distinction is better made within the context of a specific event topology where, for example, the amount and direction of missing momentum may be used to signify the presence of a leptonically decaying tau.

3.1 An Aside — Artificial Neural Networks

Artificial neural networks (ANN's) are becoming increasingly common in HEP applications due to their powerful feature-recognition abilities. They were inspired by the manner in which biological systems (such as the human brain) use networks of interconnected neurons to learn how to solve problems. ANN's have an advantage over other multivariate techniques (such as likelihoods) in that they are able to account for correlations between input variables. In this section the basics behind the type of ANN used in this work are described; it is by no means an exhaustive discussion of

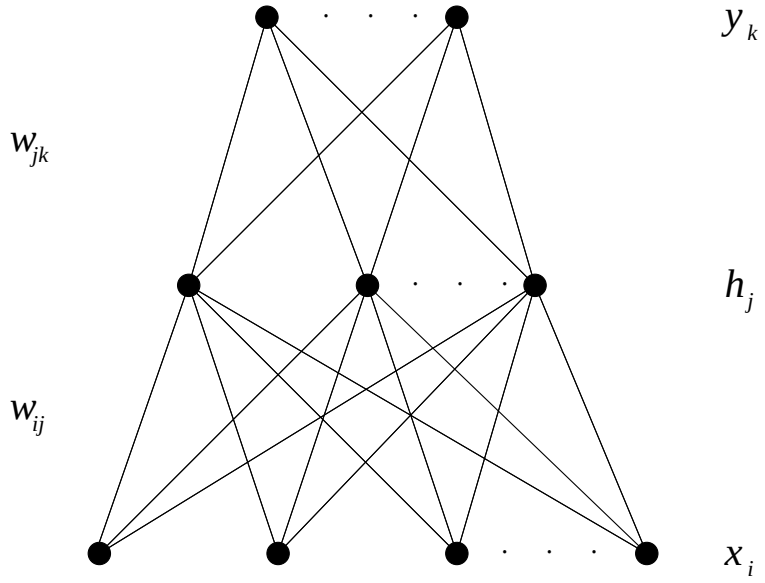

Figure 3.1: The feed-forward multilayer perceptron.

ANN theory, for which the reader is directed to [37] and references therein.

3.1.1 Feed-Forward Multilayer Perceptrons

The goal in feature recognition is to find a function $F(x_1, x_2, \ldots) = F(\vec{x})$ that maps a set of input variables $\vec{x}$ to a feature quantity y (for our purposes, call y "tauness"). Figure 3.1 shows schematically how this mapping is done via an architecture called a *multilayer perceptron*. The basic units (the black dots) are called "neurons" or "nodes" which can take on values between 0 and 1. The nodes are arranged in layers, the bottom being the "input layer," the top being the "output layer,"[1] and the middle being the "hidden layer." A node is connected to another node in the layer above it via a weight w. The mapping function sought is

$$y = F(\vec{x}) = g\left[\frac{1}{T}\sum_{j=0} w_j g\left(\frac{1}{T}\sum_{i=0} w_{ij}x_i\right)\right] \qquad (x_0 = 1) \tag{3.1}$$

[1]Figure 3.1 shows two (or more) output nodes. Since we are only concerned with describing one feature of the data (the "tauness"), one output node suffices for our purposes.

where g is a neuron "activation function" of the sigmoid form

$$g(z) = \frac{1}{2}(1 + \tanh z) \tag{3.2}$$

The parameter T (the "temperature") sets the gain of the activation function.

The hidden layer ensures the non-linearity of the mapping, as can be seen in Equation 3.1. This enables the ANN to handle problems that are not linearly separable, such as the "exclusive OR." The weights w are to be fitted to the input data and adjusted to provide the most accurate mapping.

3.1.2 Back-Propagation Updating

Training the ANN is done by providing it with a set of input patterns $\vec{x}^{(p)}$, each with a target output $t^{(p)}$ (here t would be 1 for an input pattern taken from a real tau, and 0 for a pattern taken from a fake tau). The weights w are determined by minimizing an error measure:

$$E = \frac{1}{2N_p}\sum_{p=1}^{N_p}[y^{(p)} - t^{(p)}]^2 \tag{3.3}$$

This error measure is minimized iteratively by a gradient-descent method; specifically, the weights are updated after each iteration i (called an "epoch") by the *back-propagation* learning rule:

$$w_{i+1} = w_i + \Delta w_i \tag{3.4}$$

where

$$\Delta w_i = -\eta\frac{\partial E_i}{\partial w} \tag{3.5}$$

where η is a learning rate parameter (< 1). In the above two equations w is meant to represent the whole array of weights w_{ij}.

Training proceeds by repeatedly presenting the ANN with the input patterns and updating the weights until the global minimum is reached and $\Delta w_i \approx 0$. The number of iterations this requires depends on the complexity of the problem. After training, then, the ANN has found the best mapping to the feature y for the given input patterns and is ready to classify patterns it has never "seen."

3.2 Selection of Tau Candidates

The first step in the tau identification process is to select tau candidates to input to the ANN. We begin by selecting good-quality tracks and calorimeter clusters; tracks were required to satisfy the following criteria:

- $N_{\text{CJ hits}} \geq 20$, *i.e.*, the number of central jet chamber sense wires registering a hit for the track (maximum 159)
- $N_{\text{CJ hits}} \geq \frac{1}{2} {N^{\text{exp}}_{\text{CJ hits}}}^2$
- $p_T > 120$ MeV/c
- $p < E_{\text{beam}} + 6E_{\text{beam}}\sqrt{(0.02)^2 + (0.0015E_{\text{beam}})^2}$, *i.e.*, E_{beam}+ six times the expected resolution on this energy
- $\chi^2_{r\phi} < 999$, where $\chi^2_{r\phi}$ is the χ^2 of the track fit in the $r-\phi$ plane
- $\chi^2_{sz} < 999$, where χ^2_{sz} is the χ^2 of the track fit in the $s-z$ plane (s is the arc length along the track)
- $|d_0| < 2.5$ cm
- $|z_0| < 30$ cm (track fit constrained to primary vertex in z)
- $|z_0| < 999$ cm (track fit unconstrained)
- $|\cos\theta| < 0.962$

These criteria serve to get rid of tracks from cosmic rays and interactions of the incoming electron and/or positron with residual gas molecules within the beam pipe, with a negligible effect on tracks from real e^+e^- annihilations. Calorimeter clusters were required to have raw energies exceeding 100, 250, and 600 MeV for the EM barrel, EM endcaps, and hadron calorimeters respectively, and EM endcap clusters were required to contain at least two lead-glass blocks.

[2]The number of CJ hits expected on a track depends on the track's position in the CJ fiducial volume.

Next an energy-flow correction algorithm [38] was applied to realize tracks and clusters as charged and neutral particles without double-counting. The charged particles were then considered one-by-one in decreasing order of momentum as tau "seeds" and classified as belonging to one of the three following categories:

1. **One-prong candidates.** The seed particle had $p > 2$ GeV/c and there were no other charged particles within 10°.

2. **Three-prong candidates.** There were exactly two other charged particles within 10° of the seed. The magnitude of the total momentum of the seed particle and its two "sister" particles was required to be greater than 2 GeV/c, and the total charge was required to be ± 1.

3. **Non-candidates.** The seed particle did not fall into either of the above two categories.

Tracks consistent with e^+e^- production from photon conversion were excluded in the classification process. A final requirement placed on the tau candidates was that none of the tracks used to form the candidate could belong to a candidate found previously in the event. This prevents double- or triple-counting three-prong candidates, and it gives preference to higher-momentum seeds when the possibility of "prong-sharing" between candidates arises.

The choice of a 10° cone to define the tau can be motivated by an investigation of the tau decay kinematics. At an intermediate stage, the decay can be treated as the two-body decay $\tau \to W^* \nu_\tau$. The maximum angle between the W^* and the original tau flight direction is

$$\theta_{\max} \approx \tan^{-1} \frac{1}{\beta\gamma} = \tan^{-1} \frac{m_\tau}{p_\tau} \tag{3.6}$$

where β and γ describe the boost from the tau rest frame to the lab frame. $\theta_{\max} = 10°$ corresponds to $p_\tau = 10$ GeV/c, so a 10° cone gives good containment for high-energy taus. This was empirically confirmed by an independent study of $W^+W^- \to q\bar{q}'\tau\nu_\tau$ events [39] wherein a 10° cone offered the best compromise between containment of the tau decay products and contamination from the rest of the event.

3.3 Neural Network Inputs

Around each candidate an annular cone of 30° half-angle was drawn concentric with and excluding the 10° narrow cone. This serves to define the isolation environment of the candidate. Two artificial neural networks for the two types of tau decays were developed and are henceforth referred to as the "one-prong net" and the "three-prong net." There is freedom in choosing the variables input to the neural networks; it perhaps goes without saying that the input variables should provide some degree of signal/background separation individually. One should also keep in mind that since the networks will be trained using simulated data, the input variables should be well-modelled in the Monte Carlo. Here the following variables were chosen to strike a balance between these two considerations:

- **One-prong net inputs**

    1. The invariant mass of all particles in the narrow cone.
    2. The total energy of all particles in the narrow cone.
    3. The ratio of the total energy in the annular cone to the total energy in the narrow cone.
    4. The number of particles with energy greater than 750 MeV in the annular cone. The energy cut is made to circumvent the problem of mismodelling of the calorimeter response to low-energy particles.
    5. The total energy of all charged particles in the annular cone.

- **Three-prong net inputs**

    1. The invariant mass in the narrow cone, as above.
    2. The annular/narrow cone energy ratio, as above.
    3. The number of particles with energy greater than 750 MeV in the annular cone, as above.
    4. The angle between the seed track and the furthest sister track.

Distributions of these variables for multihadronic events[3] taken in 1997 at $\sqrt{s} = 183$ GeV are shown, along with the Monte Carlo simulation, in Figure 3.2 for the one-prong net and in Figure 3.3 for the three-prong net. All the inputs are clearly modelled very well. The comparison was repeated for data taken in 1996 to verify the stability of the modelling.

3.4 Network Training

To train the networks, signal taus were taken from a sample of simulated h^0A^0 decays to $b\bar{b}\tau^+\tau^-$ and $\tau^+\tau^-b\bar{b}$ generated at $\sqrt{s} = 184$ GeV. The masses of the Higgs bosons in these samples ranged from 20 to 170 GeV/c^2, so the networks could be trained on a wide variety of tau momenta. The candidate-finding algorithm of Section 3.2 had an efficiency of 77% (60%) for one-prong (three-prong) taus in the signal sample.[4] In total about 45,000 (5,700) signal taus were used to train the one-prong (three-prong) network.

Fake taus were taken from a sample of simulated $(Z/\gamma)^* \to q\bar{q}(\gamma)$ decays at $\sqrt{s} = 183$ GeV. Approximately 1.1 (1.2) tau candidates were found per event, leading to a total training sample of about 39,000 (43,000) fake one-prong (three-prong) taus. Distributions of the input variables for signal and fakes are shown in Figure 3.4 for the one-prong net and in Figure 3.5 for the three-prong net.

The one- and three-prong nets are feed-forward neural networks with standard back-propagation updating as described in Section 3.1, implemented in the JETNET 3.1 package [40]. They both have a three-layer architecture (one input, one hidden, and one output). The number of nodes in each layer is 5:7:1 for the one-prong net and 4:5:1 for the three-prong net. There are no strict rules for how many hidden nodes should be used, so the networks were trained multiple times, varying the number of hidden nodes, and the configuration yielding the best performance (as defined by the

[3]Multihadronic events comprise four-fermion processes such as $qq\ell\ell$ as well as the more abundant $(Z/\gamma)^* \to q\bar{q}$ events.

[4]Three-prong candidates were required to have all three tracks matched to the real generated charged tau decay products in order to have 100% track purity in the training sample.

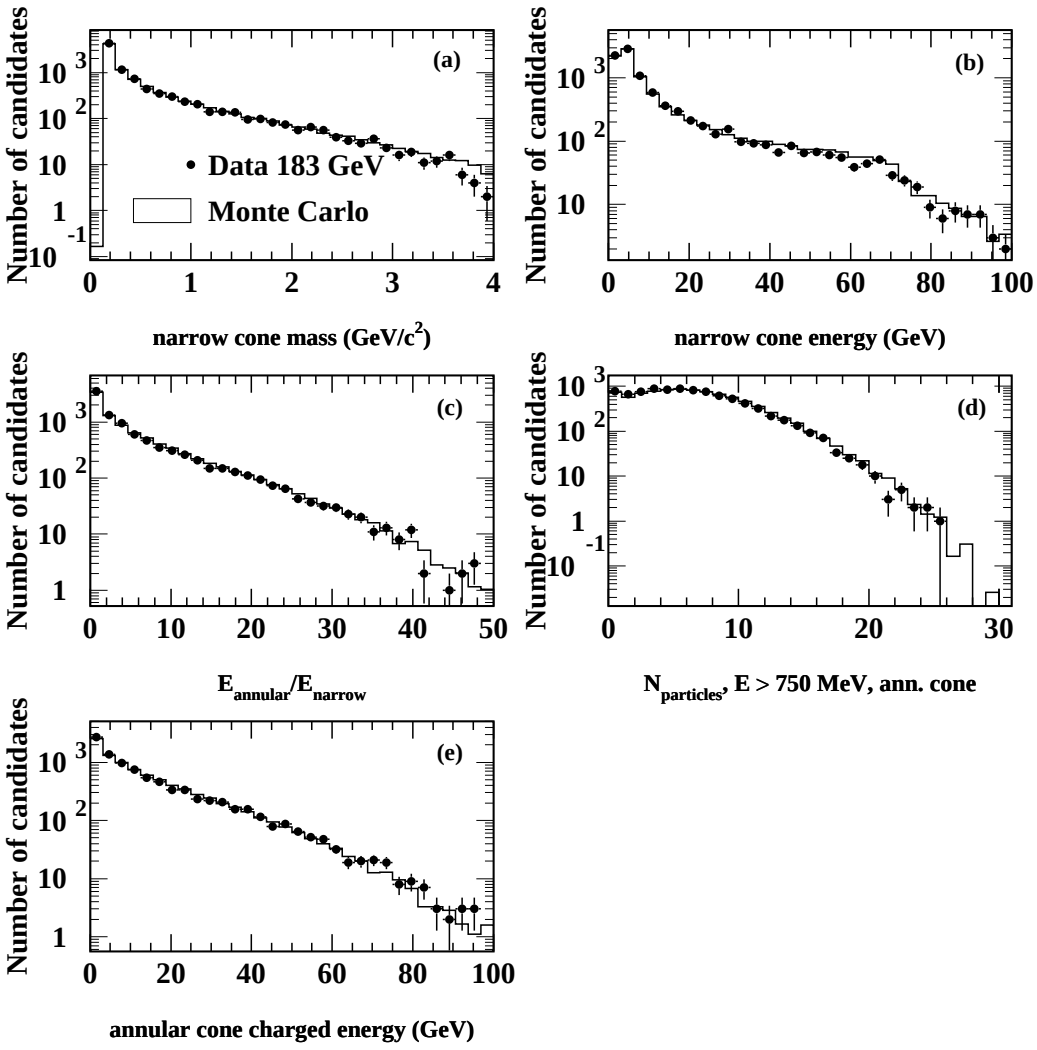

Figure 3.2: Distributions of the inputs to the one-prong net for real (points) and simulated (histogram) multihadrons at $\sqrt{s} = 183$ GeV. The Monte Carlo is normalized to the same number of one-prong tau candidates as the data.

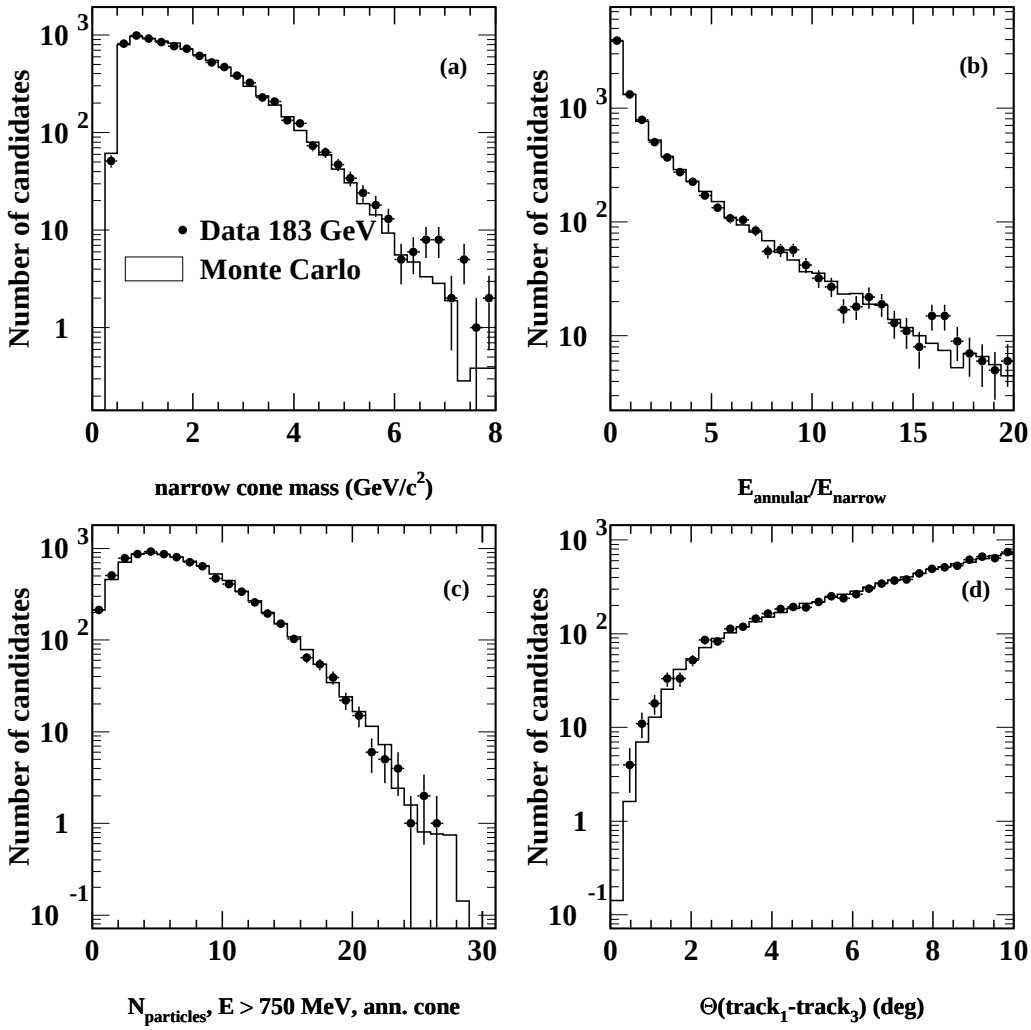

Figure 3.3: Distributions of the inputs to the three-prong net for real (points) and simulated (histogram) multihadrons at $\sqrt{s} = 183$ GeV. The Monte Carlo is normalized to the same number of three-prong tau candidates as the data.

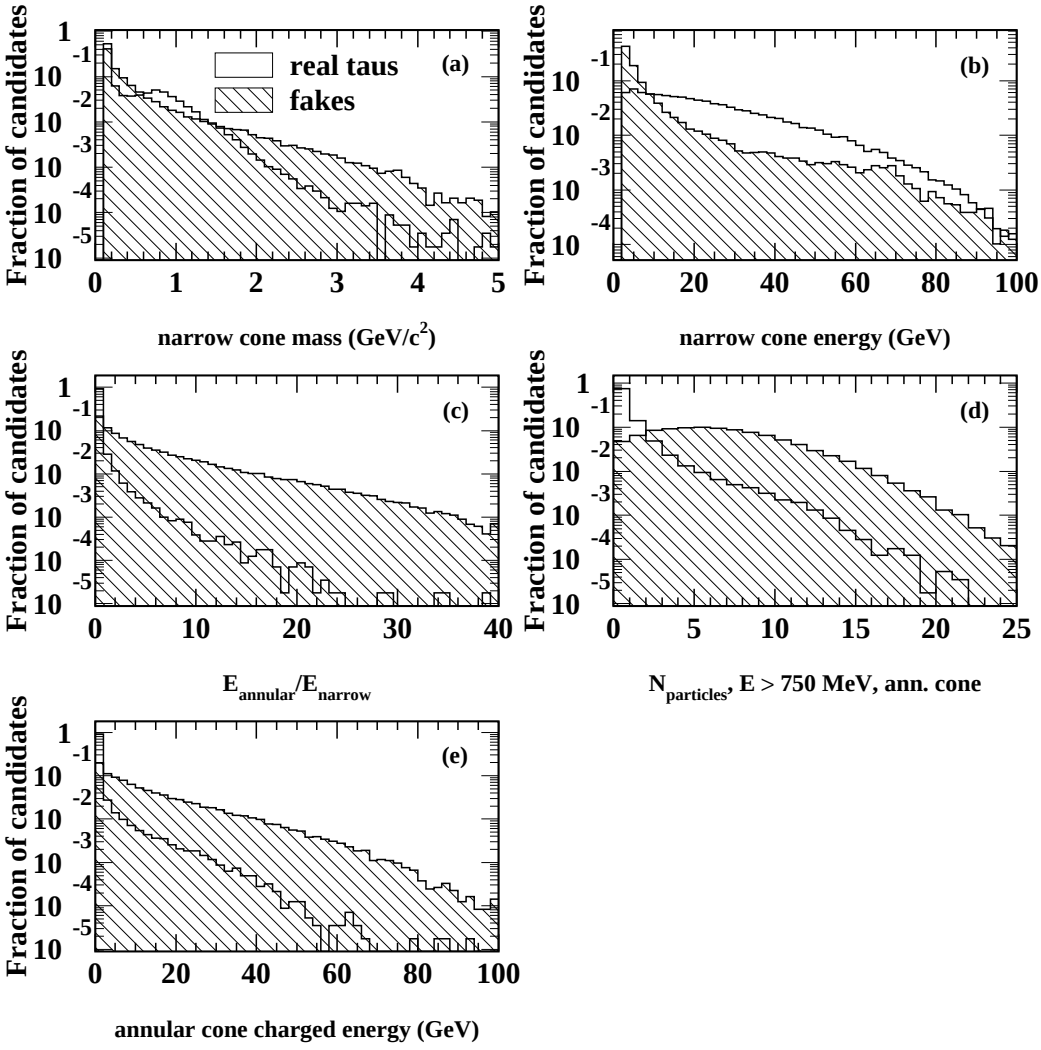

Figure 3.4: Distributions of the inputs to the one-prong net for signal taus (open histograms) and fakes (hatched histograms) used to train the network. The histograms are normalized to unity.

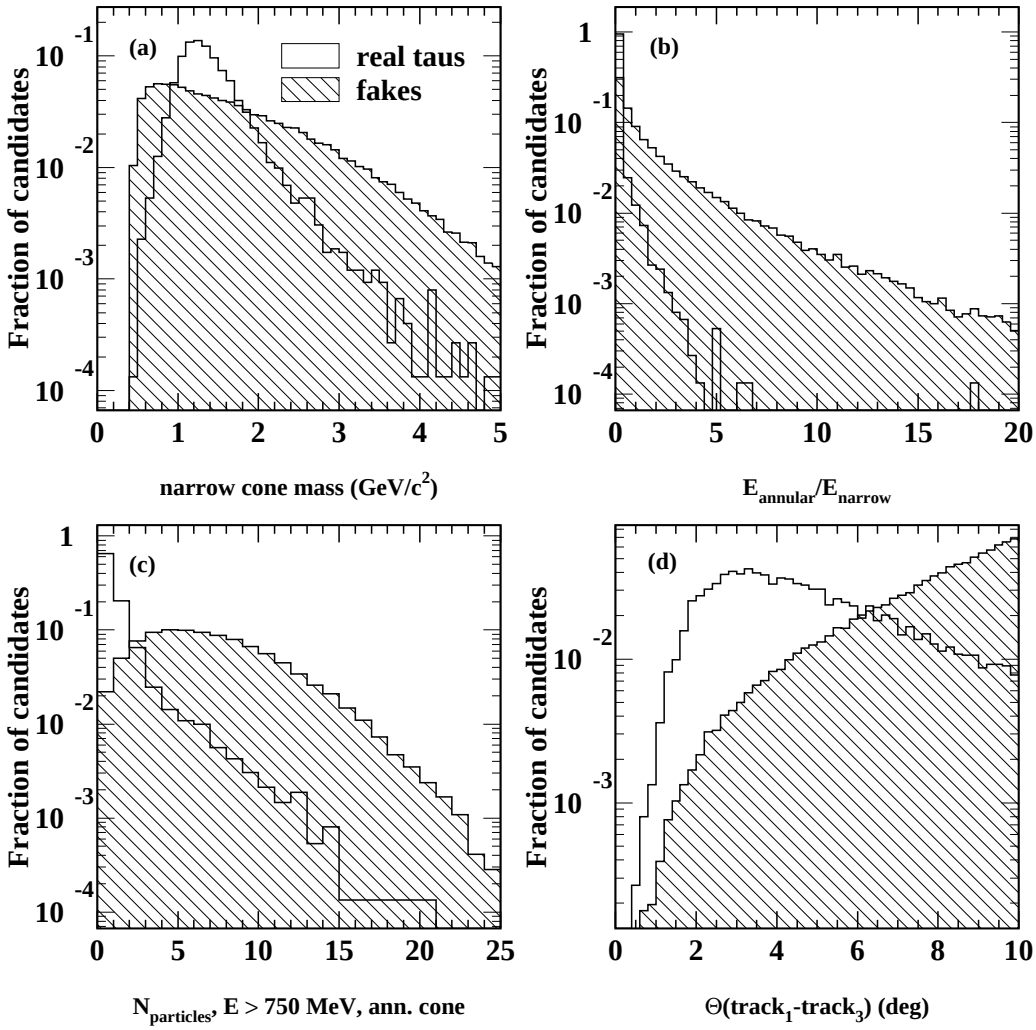

Figure 3.5: Distributions of the inputs to the three-prong net for signal taus (open histograms) and fakes (hatched histograms) used to train the network. The histograms are normalized to unity.

figure of merit described below) was chosen as the final one. In addition, the number of hidden layers is also a free parameter, but conventional wisdom states that one hidden layer is sufficient for all but the most complex problems.

To evaluate the performances of the networks the "inverse correlation integral," which measures the separation of signal (real taus) and background (fakes), is used as a figure of merit:

$$F = \alpha_s \alpha_b \int_0^1 \frac{[f_s(x) - f_b(x)]^2}{\alpha_s f_s(x) + \alpha_b f_b(x)} dx \tag{3.7}$$

Here x is the output of the neural network ($0 < x < 1$), $f(x)$ is the distribution of the network output for signal or background as denoted by the subscript, and α_s is the fraction of the sample that is signal ($\alpha_b = 1 - \alpha_s$). Values of F close to 1 indicate nearly complete separation, whereas values near zero indicate almost no separation.

The results of the network training are shown in Figure 3.6. A small sample of signal and fake taus (the "testing sample") is held in reserve to test the performance of the networks on a sample independent from that used to train the networks (the "training sample"). The top plots show the figures of merit F for the training and testing samples after each training epoch. It can be seen that the networks "learn" quickly, as F plateaus after just a few epochs. There is a danger that if one trains over too many epochs, a network "overlearns" the training sample and can no longer generalize to an arbitrary data set. This would be seen as a continuation of the plateau for the training sample, but accompanied by a decrease in F for the testing sample. Figures 3.6a and 3.6b give no indications of overlearning.

Figures 3.6c and 3.6d show the distributions of the network output for real taus and fakes in the testing sample. These are the distributions from which F is calculated. One can see a good separation between signal and background in these distributions, which will be quantified in a physics context in the next section. A small bump at 0.7 can be seen in the one-prong network output distribution for fake taus. This corresponds to a real corner of the five-dimensional input space where the background is somewhat signal-like, and is seen in both data and Monte Carlo. With the inclusion of more input variables, the additional correlations could be used to massage the bump away at the cost of a more complex network.

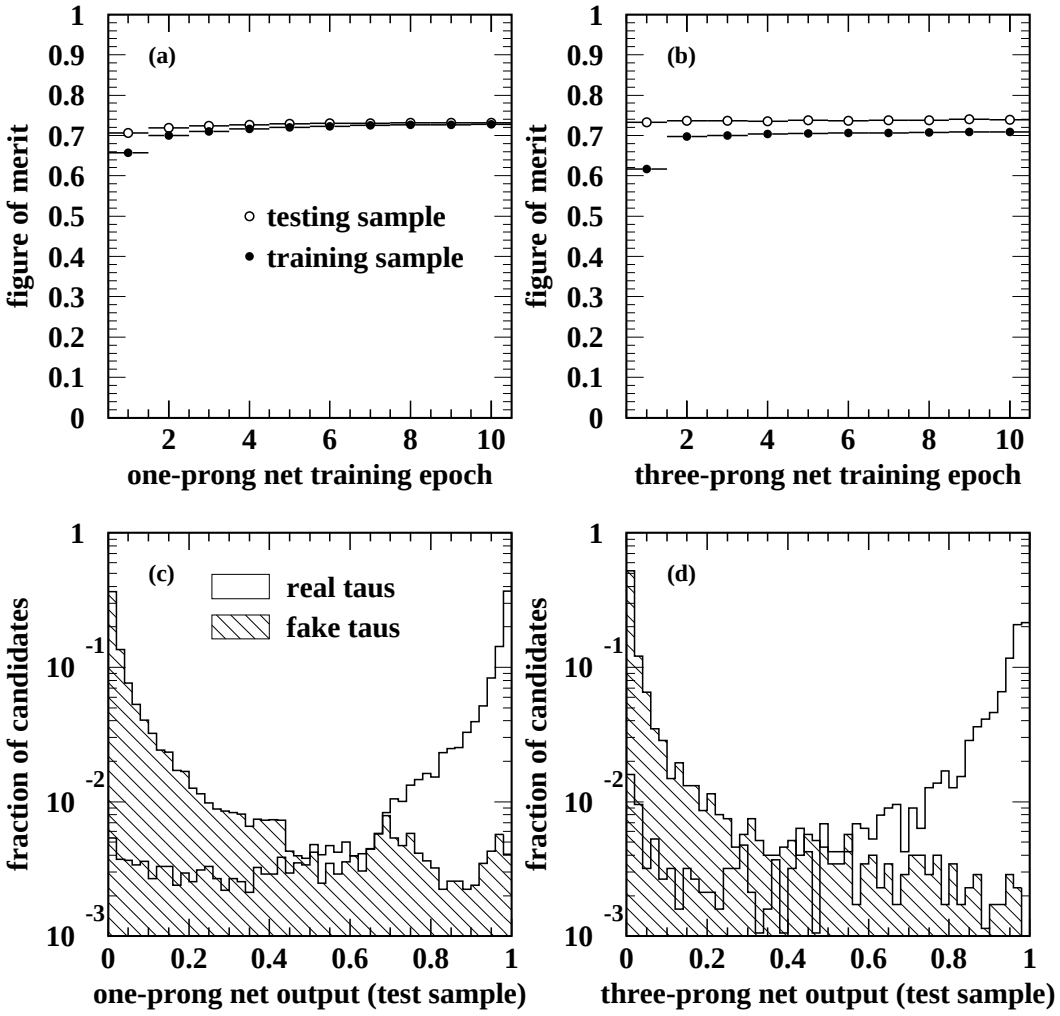

Figure 3.6: Results of the network training. Plots (a) and (c) are for the one-prong net; plots (b) and (d) are for the three-prong net.

3.5 Performance

To evaluate the performance of the tau-ID ANN, two different types of data samples were collected. The first was a sample of $Z^0 \to q\bar{q}$ events, both real and simulated, taken at LEP1, where $\sqrt{s} \approx m_Z$. These events provide a nearly tau-free sample of hadron jets with energies similar to those comprising a large background source at LEP2.[5] From these samples, the probability of the ANN to wrongly identify a tau could be parameterized as

$$\text{fake rate} = \frac{\text{number of ``taus'' found}}{\text{number of } q\bar{q} \text{ events}} \tag{3.8}$$

The other figure of merit with which to judge the ANN's performance is the efficiency, defined as

$$\epsilon = \frac{\text{number of true taus found}}{\text{number of true taus generated}} \tag{3.9}$$

Recall that the objective of the ANN was to identify taus in the challenging high-multiplicity environment. Finding a high-statistics, unbiased source of "taus+jets" events with which to test the ANN turns out to be more difficult than obtaining the copious, fairly unambiguous source of fake taus provided by $Z^0 \to q\bar{q}$ events. The solution is to again turn to LEP1, where a high-purity, high-statistics sample of $Z^0 \to \tau^+\tau^-$ events exists. To simulate the high multiplicity environment, the reconstructed tracks and calorimeter clusters from one hemisphere of a $Z^0 \to \tau^+\tau^-$ event were added to a LEP1 $Z^0 \to q\bar{q}$ event, resulting in a so-called "mixed event" topologically similar to a $q\bar{q}\tau\nu_\tau$ event with an effective center-of-mass energy of $2m_Z$. This procedure was done for both real and simulated events. The caveat here is that the taus in these events are monoenergetic ($E_\tau = m_Z/2$); however, as the Higgs masses of current interest are near m_Z, taus from Higgs decays will carry similar energies.

The efficiency as a function of the ANN cut is shown in Figure 3.7a for the mixed

[5]The majority of $q\bar{q}$ production at LEP2 energies is due to "radiative return" to the Z^0, where the quark pair is accompanied by hard, low-angle photon emission from the initial e^+e^- state (cf. Figure 2.6), resulting in an effective center-of-mass energy of m_Z.

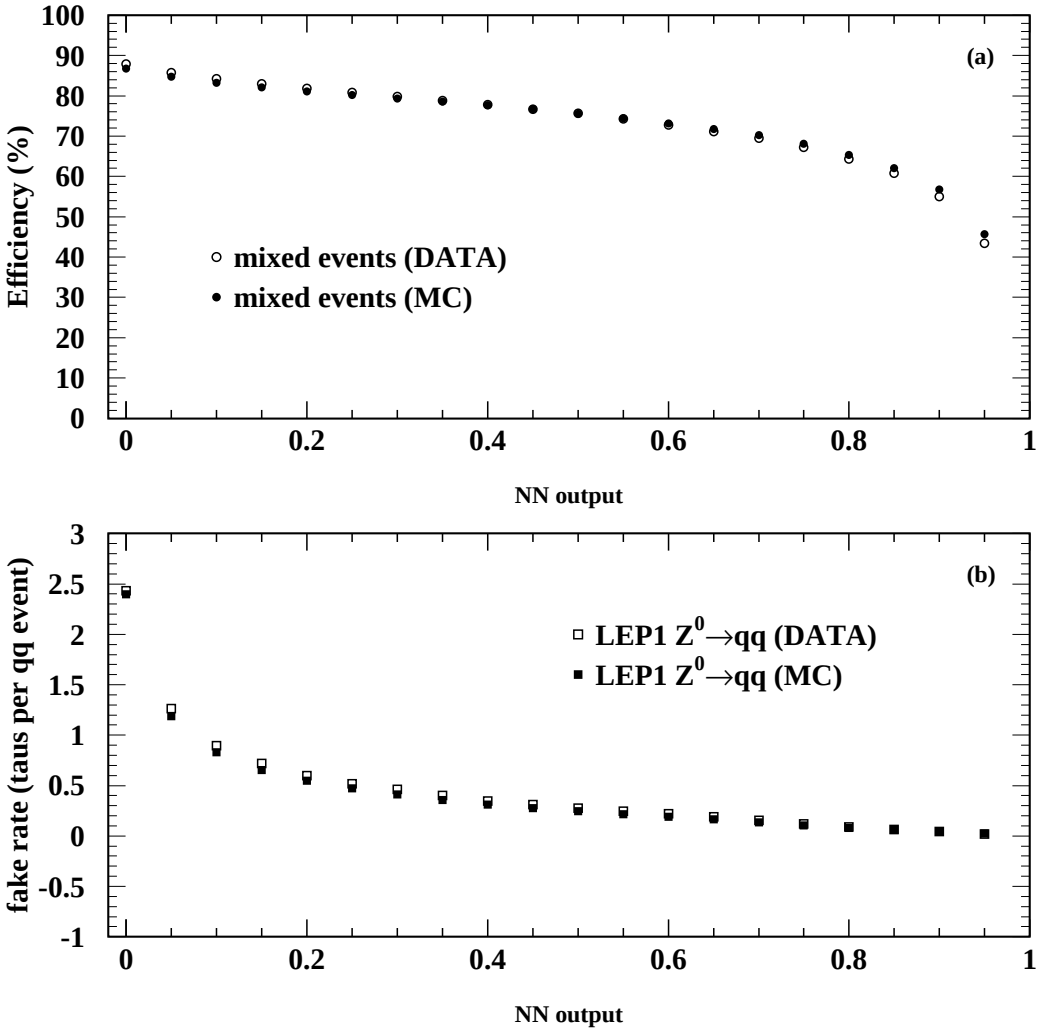

Figure 3.7: The (a) efficiency and (b) fake rate of the ANN as a function of the ANN output.

samples. To make the efficiencies indicative of the kinds of numbers one could expect in a search, the following "typical" cuts were applied to the mixed events:

1. $N_{\text{tracks}} > 5$
2. $\cos\theta_{\text{miss}} < 0.95$
3. $\text{R}_{\text{vis}} < 1$, where R_{vis} is the total visible energy divided by $\sqrt{s}$
4. $\text{R}_{\text{miss}} > 0.07$, where R_{miss} is the total missing momentum divided by $\sqrt{s}$
5. At least one tau candidate in the event

For a cut on the ANN output at 0.75, the neural network has an efficiency of about 67%. A softer cut at 0.5 gives an efficiency of 76%. At these two example operating points, the fake rate is only 0.1 (hard cut) and 0.3 (soft cut) fakes found per $\text{q}\bar{\text{q}}$ event. The fake rate as a function of the ANN output is shown in Figure 3.7b.

It is useful to know how the efficiency depends on the energy and direction of the tau. One expects a lower efficiency for lower-energy taus, due to the softer momentum spectrum of the visible decay products. This will affect the probability that the charged decay products meet the requirements of Section 3.2 to be found as a candidate, as well as the ANN output itself, since the visible energy of the tau is an input to the ANN. One also expects a lower efficiency at large polar angles due to losses in tracking acceptance.

Since the taus in the mixed samples are monoenergetic, the energy- and direction-dependence of the efficiency was studied using a sample of $\text{H}^0\text{Z}^0 \rightarrow \tau^+\tau^-\text{q}\bar{\text{q}}$ events in which the taus range over momenta from 2 to 80 GeV/c, with a mean momentum of 43.2 GeV/c. They are uniformly distributed over all $|\cos\theta| < 0.9$.

The candidate-finding efficiency (i.e., the probability that the tau meets the requirements of Section 3.2) is shown as a function of p_τ and $|\cos\theta_\tau|$ in Figure 3.8. It is seen that this efficiency is flat for all $|cos\theta_\tau| < 0.8$ and falls rapidly beyond that. The candidate-finding efficiency is at least 85% for all $p_\tau > 20$ GeV/c and drops to about 55% at $p_\tau \approx 7.5$ GeV/c.

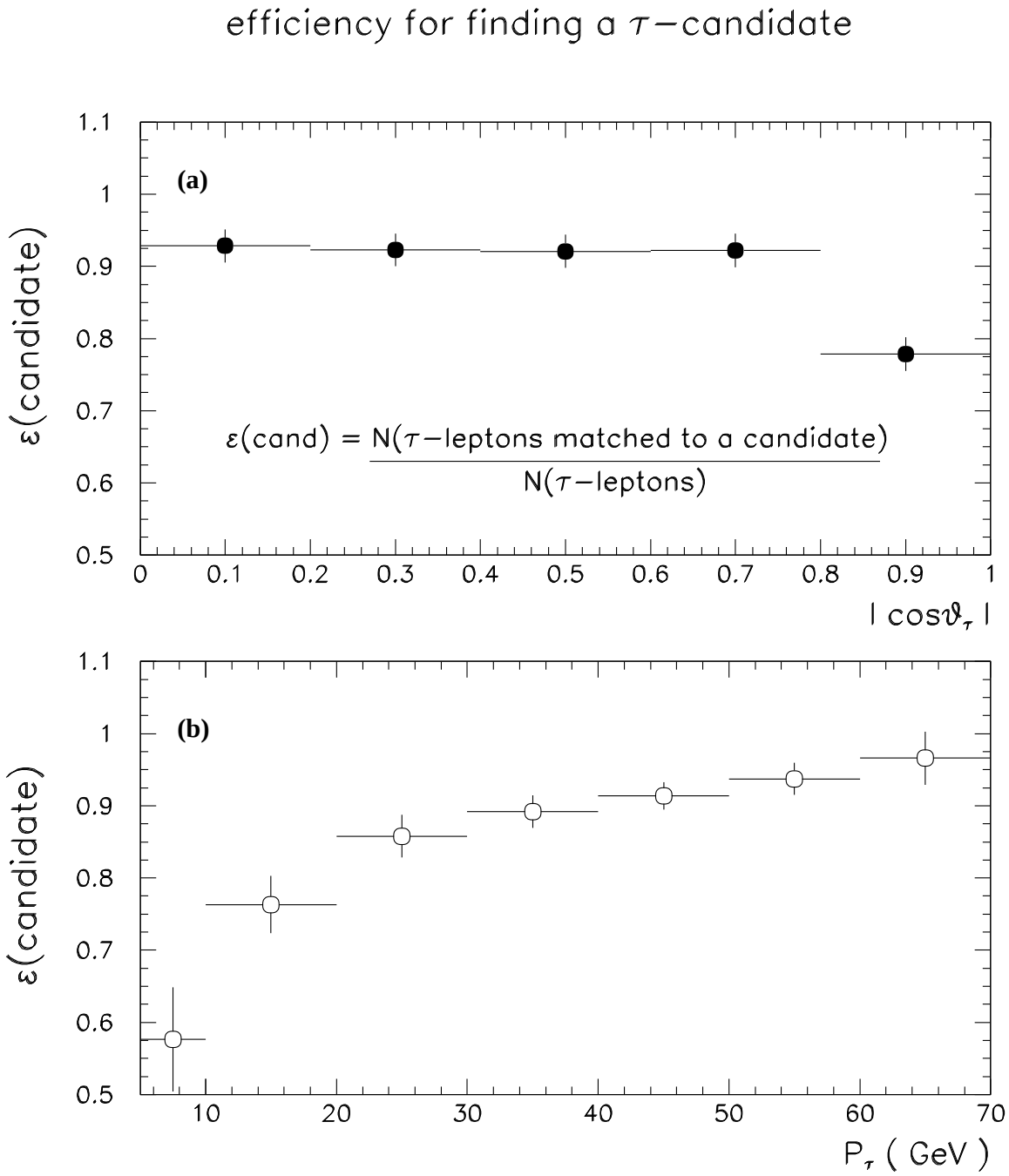

Figure 3.8: The efficiency for a tau meeting the requirements to be a candidate (cf. Section 3.2) as a function of (a) $|\cos\theta_\tau|$ and (b) p_τ.

The top plot of Figure 3.9 shows the distribution of the ANN output for three different ranges of $|\cos\theta_\tau|$. It is seen that the ANN is fairly insensitive to the tau direction. The total tau-finding efficiency as a function of $|\cos\theta_\tau|$ is shown in the bottom plot of Figure 3.9 for two different cuts on the ANN output. It is again flat until the candidate-finding efficiency loss kicks in at $|\cos\theta_\tau| > 0.8$.

The results of a similar study of the ANN efficiency's dependence on p_τ is shown in Figure 3.10. The top plot in Figure 3.10 shows that the ANN itself is sensitive to p_τ, which, along with the candidate-finding efficiency's dependence on p_τ, causes the roll-off in total efficiency at low p_τ seen in the bottom plot of Figure 3.10. In any event, the total efficiency for all $p_\tau > 20$ GeV/c is at least 64% (75%) for a cut on the ANN output at 0.75 (0.5).

3.6 Systematic Uncertainty Studies

The real and simulated LEP1 mixed events described in Section 3.5 provide a convenient "control sample" with which to analyze the systematic uncertainties on the efficiency associated with the modelling of real tau leptons. To assess the uncertainty on the fake rate due to the modelling of fake taus, the real and simulated LEP1 $Z^0 \to q\bar{q}$ samples are used.

3.6.1 Efficiency Systematics

The ratios of efficiencies (data/MC) were determined for two different cuts (0.5 and 0.75) on the ANN output, using the same number of real and simulated mixed events. These ratios were checked for dependence on

1. the tau charge ($q_\tau = \pm 1$)
2. the total energy of the visible tau decay products ($E_\tau^{\rm vis}$)
3. the direction of the visible tau decay products ($|\cos\theta_\tau^{\rm vis}|$)

The efficiency ratios in different bins of these quantities are listed in Table 3.2. The overall efficiency ratio for a cut on the ANN output of 0.5 (0.75) is 1.01 ± 0.022

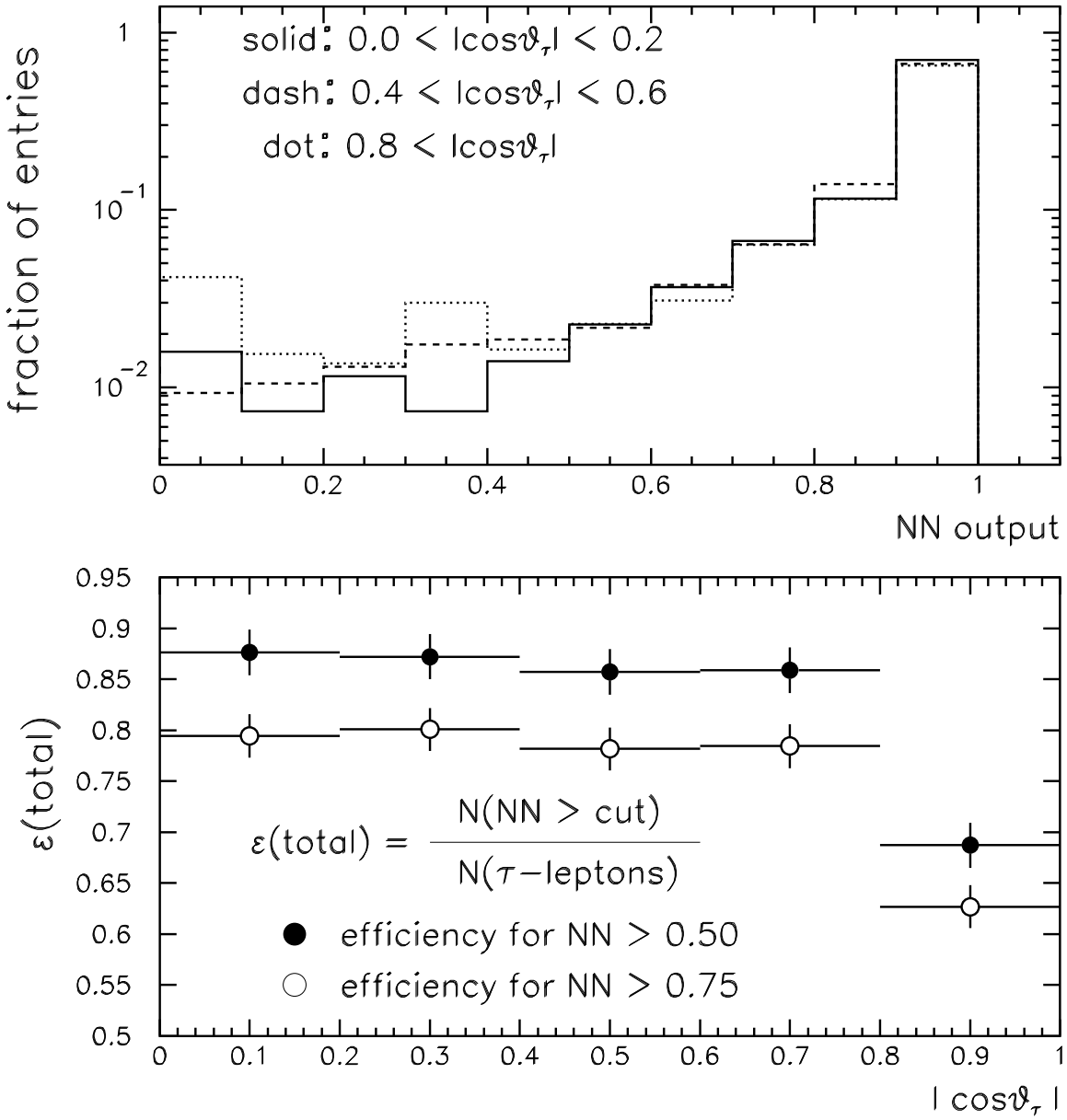

Figure 3.9: The distribution of the ANN output for three ranges of $|\cos\theta_\tau|$ (top plot) and the total tau-finding efficiency as a function of $|\cos\theta_\tau|$ for two different cuts on the ANN output (bottom plot).

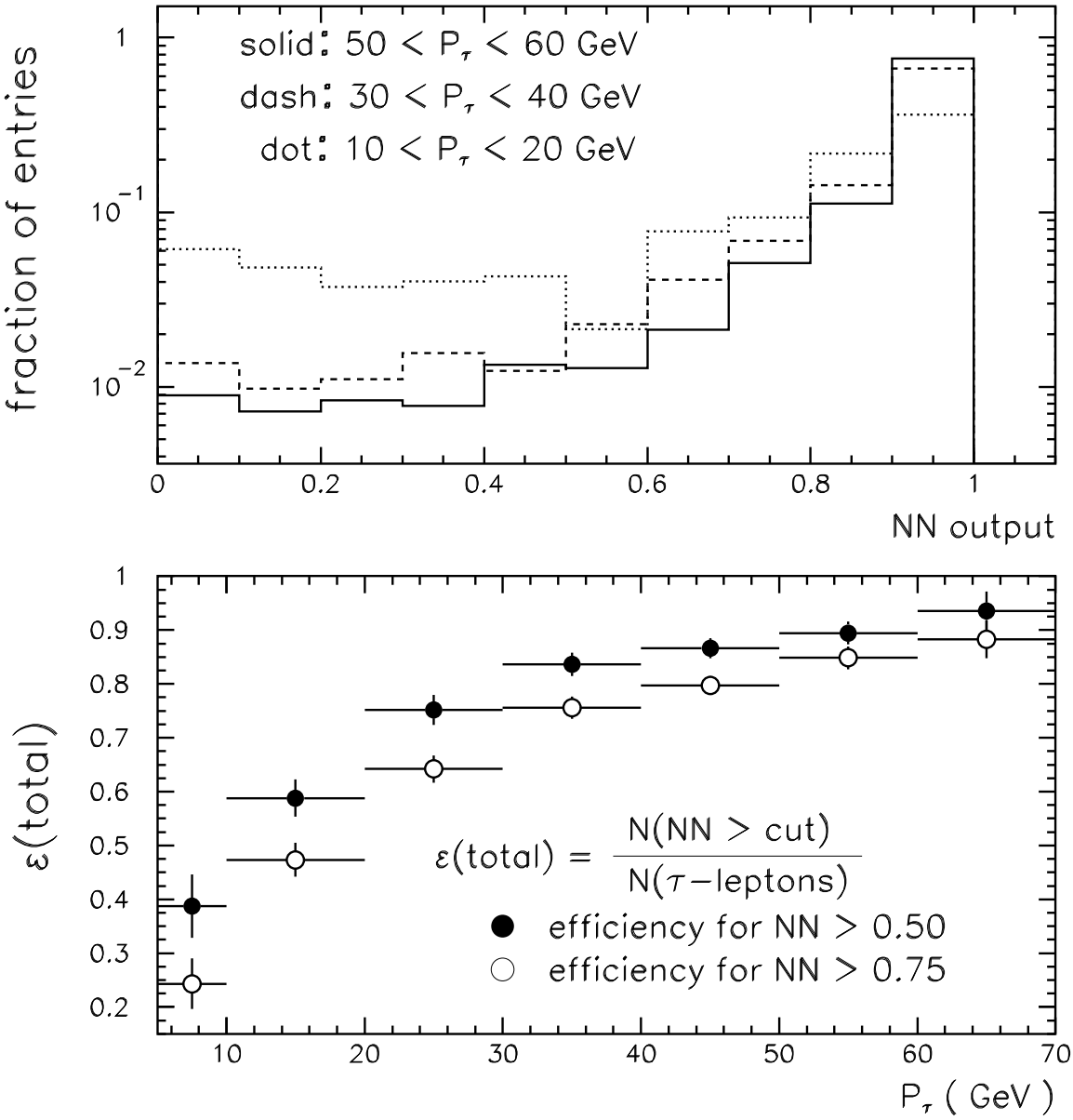

Figure 3.10: The distribution of the ANN output for three ranges of p_τ (top plot) and the total tau-finding efficiency as a function of p_τ for two different cuts on the ANN output (bottom plot).

One-prong net		
	ϵ ratio (data/MC)	
	ANN > 0.50	ANN > 0.75
Total	1.010 ± 0.022	0.998 ± 0.022
$q_\tau = +1$	0.995 ± 0.027	0.975 ± 0.027
$q_\tau = -1$	1.025 ± 0.028	1.021 ± 0.029
$2 < E_\tau^{\rm vis} < 15$ GeV	1.132 ± 0.049	1.110 ± 0.051
$15 < E_\tau^{\rm vis} < 30$ GeV	0.972 ± 0.027	0.973 ± 0.027
$30 < E_\tau^{\rm vis} < 45$ GeV	0.990 ± 0.032	0.965 ± 0.033
$45 < E_\tau^{\rm vis}$ GeV	1.175 ± 0.084	1.139 ± 0.089
$0.0 < \lvert\cos\theta_\tau^{\rm vis}\rvert < 0.2$	0.984 ± 0.037	0.952 ± 0.037
$0.2 < \lvert\cos\theta_\tau^{\rm vis}\rvert < 0.4$	0.988 ± 0.037	0.983 ± 0.038
$0.4 < \lvert\cos\theta_\tau^{\rm vis}\rvert < 0.6$	1.031 ± 0.038	1.014 ± 0.039
$0.5 < \lvert\cos\theta_\tau^{\rm vis}\rvert < 0.8$	0.988 ± 0.037	0.977 ± 0.038
$0.8 < \lvert\cos\theta_\tau^{\rm vis}\rvert$	1.111 ± 0.055	1.130 ± 0.058
Three-prong net		
	ϵ ratio (data/MC)	
	ANN > 0.50	ANN > 0.75
Total	1.001 ± 0.052	0.978 ± 0.053
$q_\tau = +1$	0.993 ± 0.066	0.978 ± 0.068
$q_\tau = -1$	1.008 ± 0.066	0.978 ± 0.067
$2 < E_\tau^{\rm vis} < 25$ GeV	0.873 ± 0.087	0.847 ± 0.089
$25 < E_\tau^{\rm vis} < 35$ GeV	0.918 ± 0.069	0.897 ± 0.071
$35 < E_\tau^{\rm vis} < 45$ GeV	1.065 ± 0.079	1.064 ± 0.083
$45 < E_\tau^{\rm vis}$ GeV	1.42 ± 0.19	1.32 ± 0.19
$0.0 < \lvert\cos\theta_\tau^{\rm vis}\rvert < 0.2$	1.014 ± 0.092	1.034 ± 0.098
$0.2 < \lvert\cos\theta_\tau^{\rm vis}\rvert < 0.4$	1.15 ± 0.10	1.14 ± 0.11
$0.4 < \lvert\cos\theta_\tau^{\rm vis}\rvert < 0.6$	1.015 ± 0.092	0.939 ± 0.091
$0.5 < \lvert\cos\theta_\tau^{\rm vis}\rvert < 0.8$	0.848 ± 0.079	0.835 ± 0.084
$0.8 < \lvert\cos\theta_\tau^{\rm vis}\rvert$	0.97 ± 0.12	0.91 ± 0.13

Table 3.2: One- and three-prong net efficiency ratios (data/MC) evaluated from the LEP1 mixed samples for two different ANN output cuts and for various values of q_τ, $E_\tau^{\rm vis}$, and $\lvert\cos\theta_\tau^{\rm vis}\rvert$.

(0.998 ± 0.022) for the one-prong net and 1.00 ± 0.055 (0.978 ± 0.053) for the three-prong net.

As the efficiency ratios are consistent with 1, a systematic uncertainty on the efficiency is assigned according to the statistical sensitivity of this test. The uncertainty for one-prong taus is then 2.2% and is 5.5% for three-prong taus. Taking the average, weighted by the one- and three-prong tau branching ratios, we arrive at a systematic uncertainty on the efficiency of 2.7%. No strong dependence on q_τ, $E_\tau^{\rm vis}$, or $|\cos\theta_\tau^{\rm vis}|$ is seen. The ANN outputs for the mixed events are shown in Figure 3.11

3.6.2 Fake Rate Systematics

A similar study was performed to check the uncertainty associated with the modelling of hadronic fake taus by calculating the fake rate ratio (data/MC) for LEP1 $Z^0 \to q\bar{q}$ events. These ratios are listed in Table 3.3.

Based on the overall ratios in Table 3.3, a systematic error of 20% (taking the larger of the two ratios for ANN > 0.5 and ANN > 0.75 to be conservative) is assigned to the one-prong fake rate and 2% to the three-prong rate. As the three-prong fakes constitute about half the total fake rate, an appropriate weighted average yields an overall fake rate systematic uncertainty of 10%. This uncertainty is strongly dependent on $E_\tau^{\rm vis}$; its sharp rise with falling $E_\tau^{\rm vis}$ is seen clearly in Table 3.3.

To understand the source of this uncertainty, we note that the ratios R listed in Tables 3.2 and 3.3 come in two pieces:

$$R = R_{\rm cand} \cdot R_{\rm ANN} \tag{3.10}$$

$R_{\rm cand}$ is the ratio of the number of tau candidates observed in the data to the number observed in the MC, according to the requirements of Section 3.2. $R_{\rm ANN}$ is the ratio of the fraction of tau candidates passing some cut on the ANN output as observed in the data to the fraction passing as observed in the MC. Whereas $R_{\rm ANN}$ was kept under control by choosing well-modelled inputs to the ANN, $R_{\rm cand}$ is more sensitive to details of the MC tune (*e.g.* fragmentation and hadronization modelling), as this dictates the characteristics of single, soft, isolated tracks that become one-prong tau

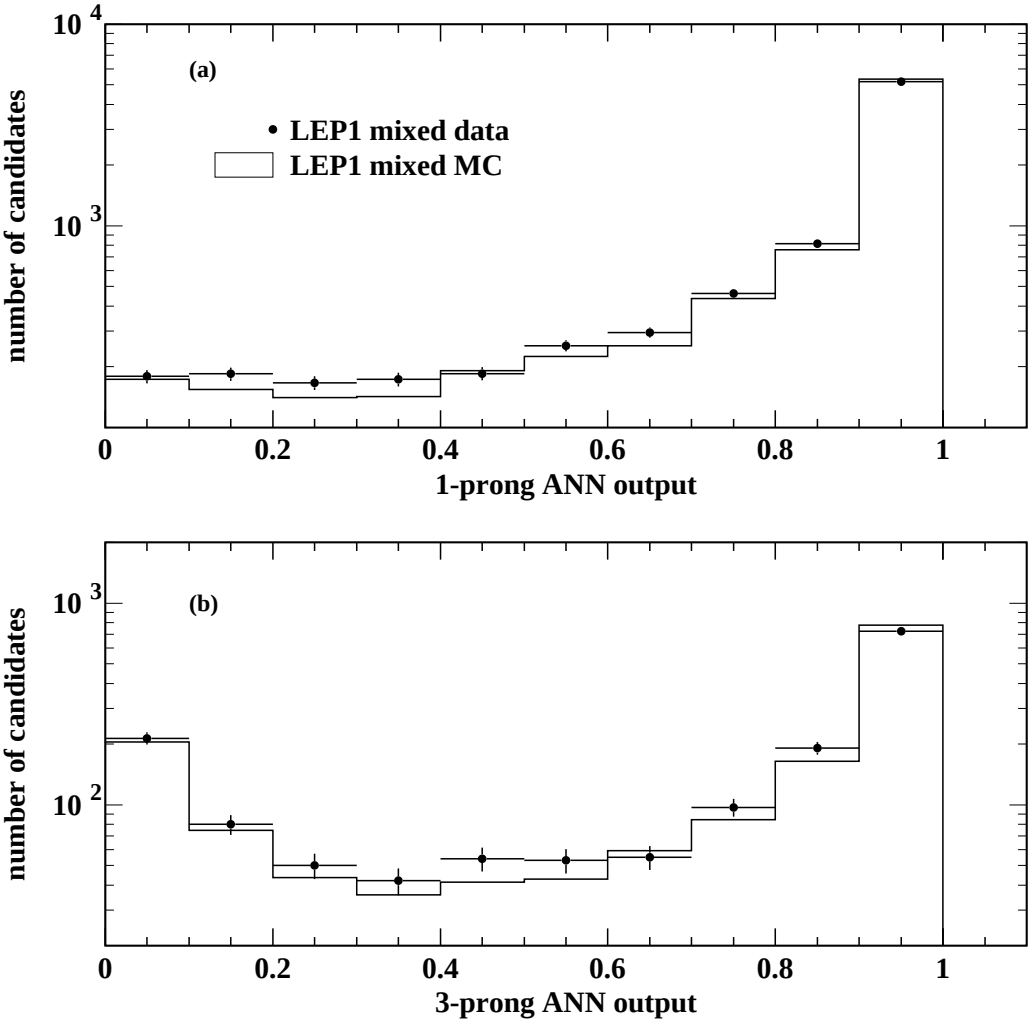

Figure 3.11: The distribution of (a) one-prong and (b) three-prong net outputs for real taus taken from LEP1 mixed events. The Monte Carlo is normalized to the same number of events as the data.

One-prong net		
	fake rate ratio (data/MC)	
	ANN > 0.50	ANN > 0.75
Total	1.209 ± 0.019	1.109 ± 0.027
$q_\tau = +1$	1.214 ± 0.026	1.102 ± 0.036
$q_\tau = -1$	1.205 ± 0.026	1.112 ± 0.038
$2 < E_\tau^{\rm vis} < 5$ GeV	1.606 ± 0.045	2.08 ± 0.13
$5 < E_\tau^{\rm vis} < 10$ GeV	1.696 ± 0.074	1.85 ± 0.12
$10 < E_\tau^{\rm vis} < 20$ GeV	1.323 ± 0.049	1.344 ± 0.078
$20 < E_\tau^{\rm vis}$ GeV	0.852 ± 0.021	0.774 ± 0.025
$0.0 < \lvert\cos\theta_\tau^{\rm vis}\rvert < 0.2$	1.256 ± 0.045	1.174 ± 0.068
$0.2 < \lvert\cos\theta_\tau^{\rm vis}\rvert < 0.4$	1.284 ± 0.046	1.158 ± 0.068
$0.4 < \lvert\cos\theta_\tau^{\rm vis}\rvert < 0.6$	1.207 ± 0.043	1.114 ± 0.063
$0.5 < \lvert\cos\theta_\tau^{\rm vis}\rvert < 0.8$	1.276 ± 0.045	1.175 ± 0.064
$0.8 < \lvert\cos\theta_\tau^{\rm vis}\rvert$	1.104 ± 0.031	1.017 ± 0.043
Three-prong net		
	fake rate ratio (data/MC)	
	ANN > 0.50	ANN > 0.75
Total	0.996 ± 0.017	1.002 ± 0.024
$q_\tau = +1$	0.980 ± 0.023	0.983 ± 0.033
$q_\tau = -1$	1.012 ± 0.024	1.021 ± 0.035
$2 < E_\tau^{\rm vis} < 10$ GeV	1.139 ± 0.049	1.236 ± 0.069
$10 < E_\tau^{\rm vis} < 20$ GeV	1.107 ± 0.049	1.142 ± 0.079
$20 < E_\tau^{\rm vis} < 30$ GeV	1.033 ± 0.036	1.087 ± 0.058
$30 < E_\tau^{\rm vis}$ GeV	0.915 ± 0.022	0.869 ± 0.030
$0.0 < \lvert\cos\theta_\tau^{\rm vis}\rvert < 0.2$	1.010 ± 0.040	1.036 ± 0.059
$0.2 < \lvert\cos\theta_\tau^{\rm vis}\rvert < 0.4$	1.000 ± 0.039	0.941 ± 0.052
$0.4 < \lvert\cos\theta_\tau^{\rm vis}\rvert < 0.6$	0.955 ± 0.036	0.931 ± 0.053
$0.5 < \lvert\cos\theta_\tau^{\rm vis}\rvert < 0.8$	1.009 ± 0.036	1.047 ± 0.056
$0.8 < \lvert\cos\theta_\tau^{\rm vis}\rvert$	1.002 ± 0.032	1.039 ± 0.049

Table 3.3: One- and three-prong net fake rate ratios (data/MC) evaluated from LEP1 $Z^0 \to q\bar{q}$ for two different ANN output cuts and for various values of q_τ, $E_\tau^{\rm vis}$, and $|\cos\theta_\tau^{\rm vis}|$.

candidates.

The 20% discrepancy in the one-prong fake rate turns out to be evenly split between R_{cand} and R_{ANN}. Figure 3.12a shows the ANN output distributions for real and simulated one-prong fakes; the agreement of the normalizations of these distributions is dictated by R_{cand} whereas the agreements of the shapes are related to R_{ANN}. One-prong fake taus have been historically problematic in OPAL; when the first $\mathrm{W^+W^-} \to \mathrm{q\bar{q}'}\tau\nu_\tau$ event selections [41] were being tuned, it was noticed that one-prong fakes in the MC were more isolated than those in the data, in the sense that simulated one-prong fakes typically had less energy in their isolation cones than real one-prong fakes. This discrepancy was traced to a mismodelling of soft hadrons in the electromagnetic calorimeter. Here the 2 GeV/c candidate momentum cut and the 750 MeV energy cut on annular cone particles input to the ANN serve to effectively halve this discrepancy.

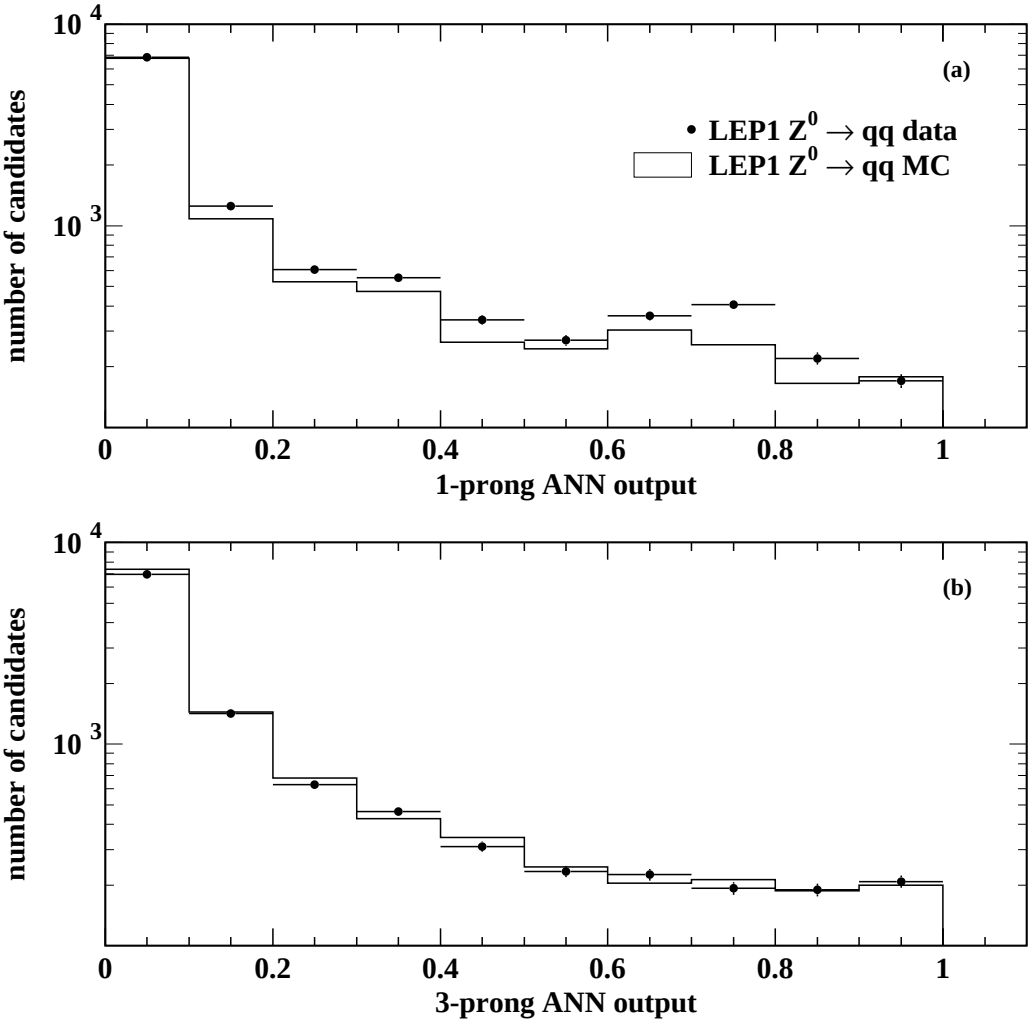

Figure 3.12: The distribution of (a) one-prong and (b) three-prong net outputs for fake taus taken from LEP1 $Z^0 \rightarrow q\bar{q}$ events. The Monte Carlo is normalized to the same number of events as the data.

CHAPTER 4
SELECTION OF HIGGS-LIKE EVENTS

The $q\bar{q}\tau^+\tau^-$ final state is characterized by two energetic hadron jets and and two isolated tau leptons, with significant missing energy arising from the neutrinos produced in the tau decay. In addition, when considering the Higgsstrahlung process described in Section 1.3.1, either the tau pair or the jet pair will have an invariant mass consistent with m_Z. In the case where the jets arise from the decay of a Higgs boson, the jets will very often have the distinction of carrying b-flavor (see Section 1.3.2).

Bearing this in mind, we consider what the expected background sources will be in this search. Since $\sqrt{s} > 2m_Z$, we are above the threshold for the pair production of Z^0 bosons. Therefore the process $Z^0Z^0 \to q\bar{q}\tau^+\tau^-$ becomes an irreducible background if the mass of the Higgs is near m_Z. Another four-fermion (4f) background source at LEP2 is the pair production of W bosons. In the semileptonic decay of the W pair ($W^+W^- \to q\bar{q}'\ell\nu_\ell$), there is a possibility of misidentifying part of the hadronic system as a tau lepton and thus realizing the event as a $q\bar{q}\tau^+\tau^-$ event. We note, however, that the jets in W decay do not carry b-flavor (V_{ub} and V_{cb} are small and $W \to tb$ is kinematically inaccessible). Finally, we consider the two-fermion (2f) process $(Z/\gamma)^* \to q\bar{q}$, in which two fake taus can arise from jet fragmentation tracks or low-multiplicity gluon jets, leaving a $q\bar{q}\tau^+\tau^-$-like topology. Although the excellent background rejection of the τ-ID ANN (Chapter 3) renders the probability of this occurrence rather small, the large cross section for this process ($\sim$ 100 pb) makes it a non-trivial background.

Section 4.1 gives a detailed description of the analysis used to search for the Standard Model Higgs boson. This analysis provides the backbone for slightly modified searches, described in Sections 4.2 and 4.3, for Higgs bosons in other models.

4.1 Standard Model Higgs Search

The overall organization of the SM $q\bar{q}\tau^+\tau^-$ Higgs search is a set of four sequential cuts of varying complexity (the first cut is actually a collection of cuts in itself), which are described in Sections 4.1.1 through 4.1.4. These cuts are followed by a final two-dimensional likelihood cut, described in Section 4.1.5. The effects of the cuts will be summarized in Table 4.2 at the end of this section.

4.1.1 Preliminary Event Selection

The selection begins with a standard set of loose cuts that retain events consistent with multihadron production and reject the vast majority of events that arise from "soft" processes like virtual photon-photon interactions. These cuts (collectively referred to as the "L2MH" cut) require a significant amount of energy deposited in the calorimeters that is not too unbalanced in the forward-backward direction. In addition low-multiplicity events are rejected by the L2MH cut by requiring a minimum number of charged tracks and calorimeter clusters.

At this point the quality requirements and energy-flow correction algorithm mentioned in Section 3.2 are applied to the tracks and clusters. In addition, a cut is made requiring the measured dp/p of a track to be less than 0.5 when the track's azimuthal angle is within 1.5° of a CJ anode plane. This is because stiff, isolated fake tracks arising from coherent anode plane noise can easily fake an energetic tau. After the energy-flow calculation events roughly consistent with the $q\bar{q}\tau^+\tau^-$ topology were selected by requiring them to meet the following criteria:

- $R_{miss} < 0.3$, where R_{miss} is the total missing momentum divided by $\sqrt{s}$
- $\cos\theta_{miss} < 0.95$, where θ_{miss} is the polar angle of the missing momentum vector
- $\sum_i p_T^i > 45$ GeV/c, where p_T^i is the scalar transverse momentum of the i^{th} particle in the event
- At least one pair of oppositely-charged tau candidates (see Section 3.2) in the event.

Distributions of these variables are shown for data and Monte Carlo in Figure 4.1. The effect of these preselection cuts (including L2MH) is a reduction of the two-photon background by over 99.9%, the four-fermion background by 87%, and the two-fermion $q\bar{q}$ background by 83%. The signal efficiency for a SM Higgs of mass 95 GeV/c^2 is reduced by 20%.

4.1.2 Tau Pair Tagging

To identify a tau pair in the event the neural network algorithm described in Chapter 3 is employed. The network outputs for the two highest-output tau candidates in simulated signal and background events are shown in Figure 4.2. A clear separation of signal and background is seen. To combine the two outputs in an optimal way, we first consider that one-prong taus and three-prong taus should not be given equal weight as they are in Figure 4.2. In addition to their substantially different branching ratios, they are subject to different levels of accepted signal and background when forming candidates, and the two different neural nets do not have identical sensitivities. To properly address these concerns we construct the following more probability-like quantity based on a tau's neural net output:

$$\mathcal{P}(x_i) = \frac{\mathcal{B}_i \epsilon_i f_i^{\mathrm{sig}}(x_i)}{\mathcal{B}_i \epsilon_i f_i^{\mathrm{sig}}(x_i) + \mathcal{F}_i f_i^{\mathrm{bkg}}(x_i)} \tag{4.1}$$

Here, $\mathcal{B}_i$ is the i-prong tau branching ratio, ϵ_i is the i-prong candidate finding efficiency (taken from the Monte Carlo sample used to train the networks; cf. Section 3.4), $f_i^{\mathrm{sig\ (bkg)}}(x_i)$ is the probability for a real (fake) i-prong tau to have network output x_i, and $\mathcal{F}_i$ is the average number of fake i-prong taus found per $q\bar{q}$ event. The f_i's are determined by fitting an analytic function to the shapes of the network outputs so that the final $\mathcal{P}$ has no unnatural discreteness due to binning effects. For real taus, we fit the shape of the output for the network "testing data" (described in Section 3.4). Since there already exists a good source of fake taus in Z^0 calibration runs, we use these data to determine f_i^{bkg} and $\mathcal{F}_i$, thus lessening the reliance on Monte Carlo simulation. The fits are shown in Figure 4.3; ϵ_i and $\mathcal{F}_i$ are given in Table 4.1.

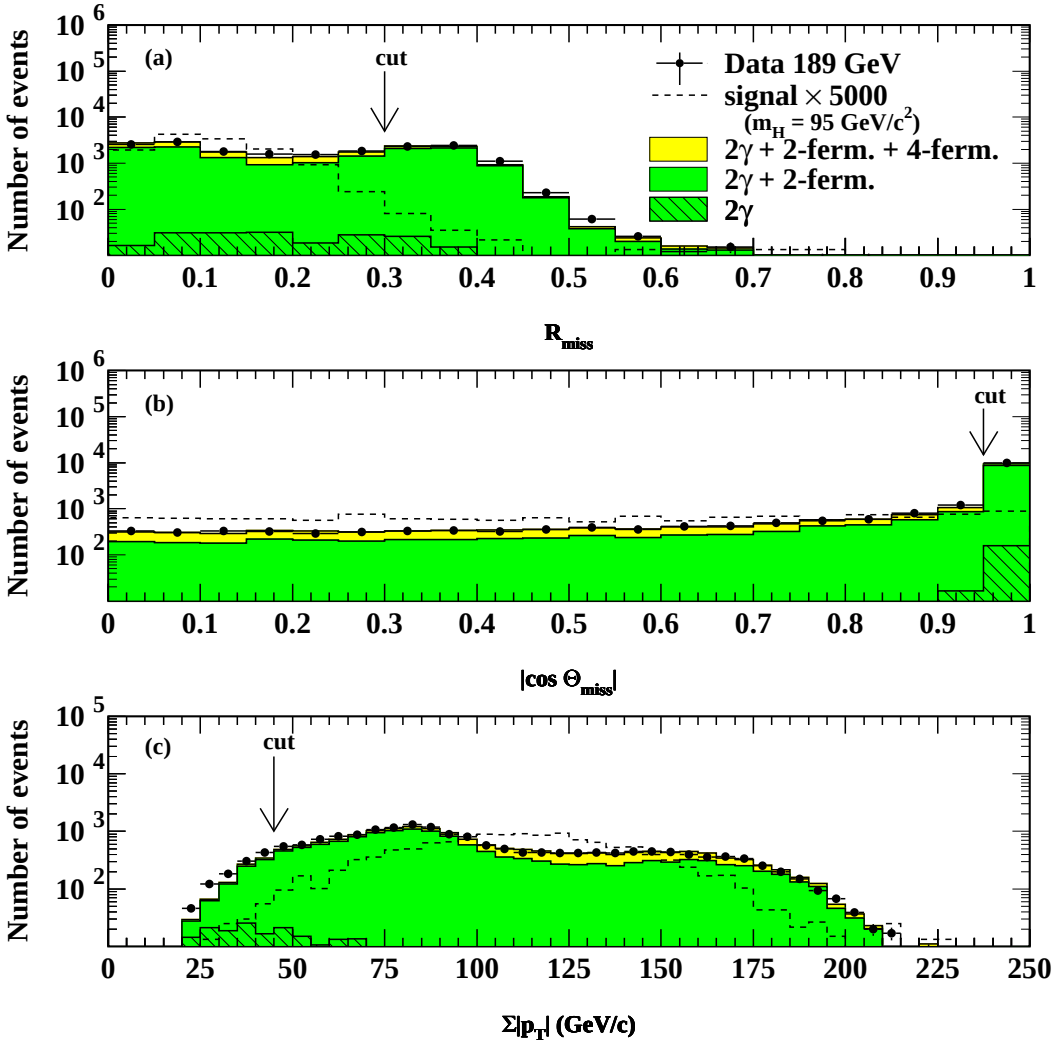

Figure 4.1: Distributions of the variables used in the preselection. The signal has been scaled up by a factor of 5000 for visibility. In all plots in this chapter, the background MC expectation is normalized to the integrated luminosity of the data.

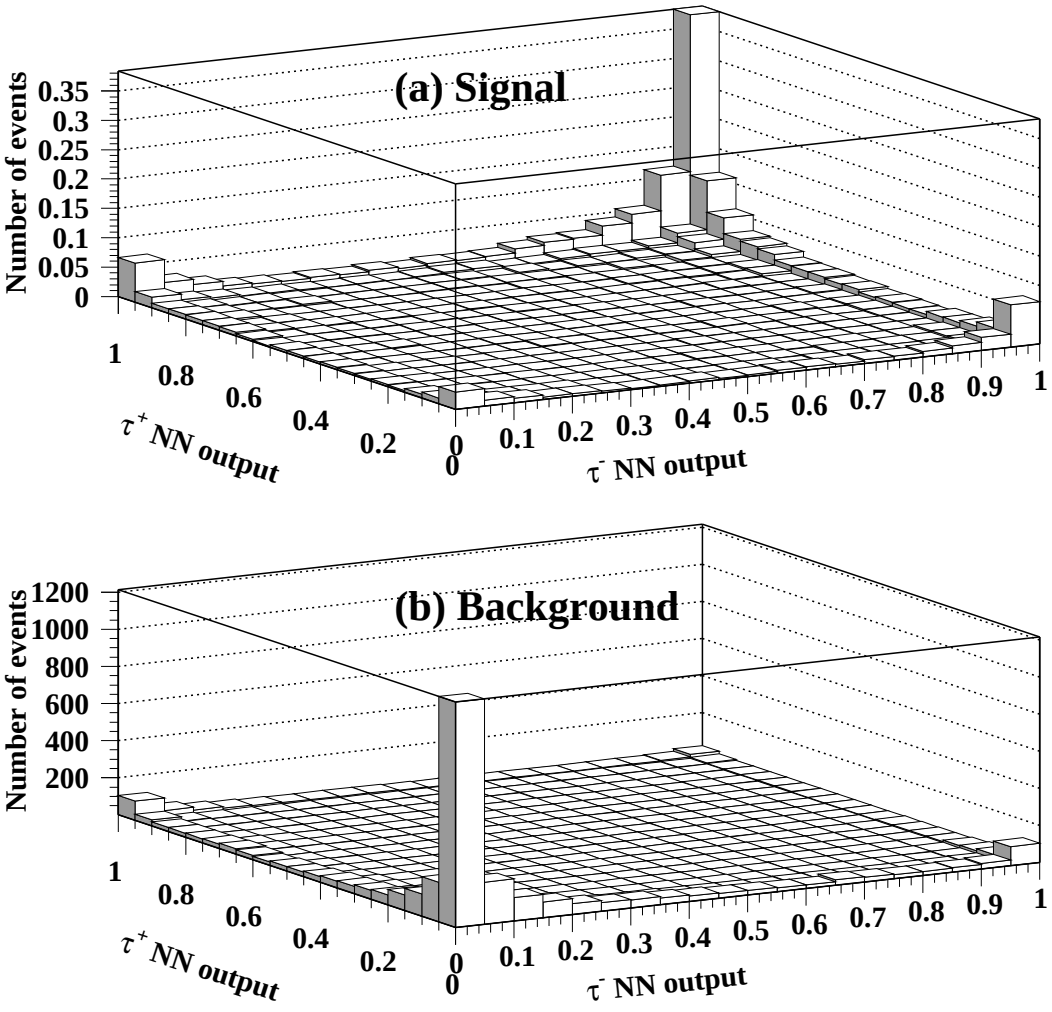

Figure 4.2: Distributions of the output of the τ-ID neural network for the two highest-output tau candidates in preselected events. Simulated 95 GeV/c^2 SM Higgs events are shown in (a), while SM background processes are shown in (b).

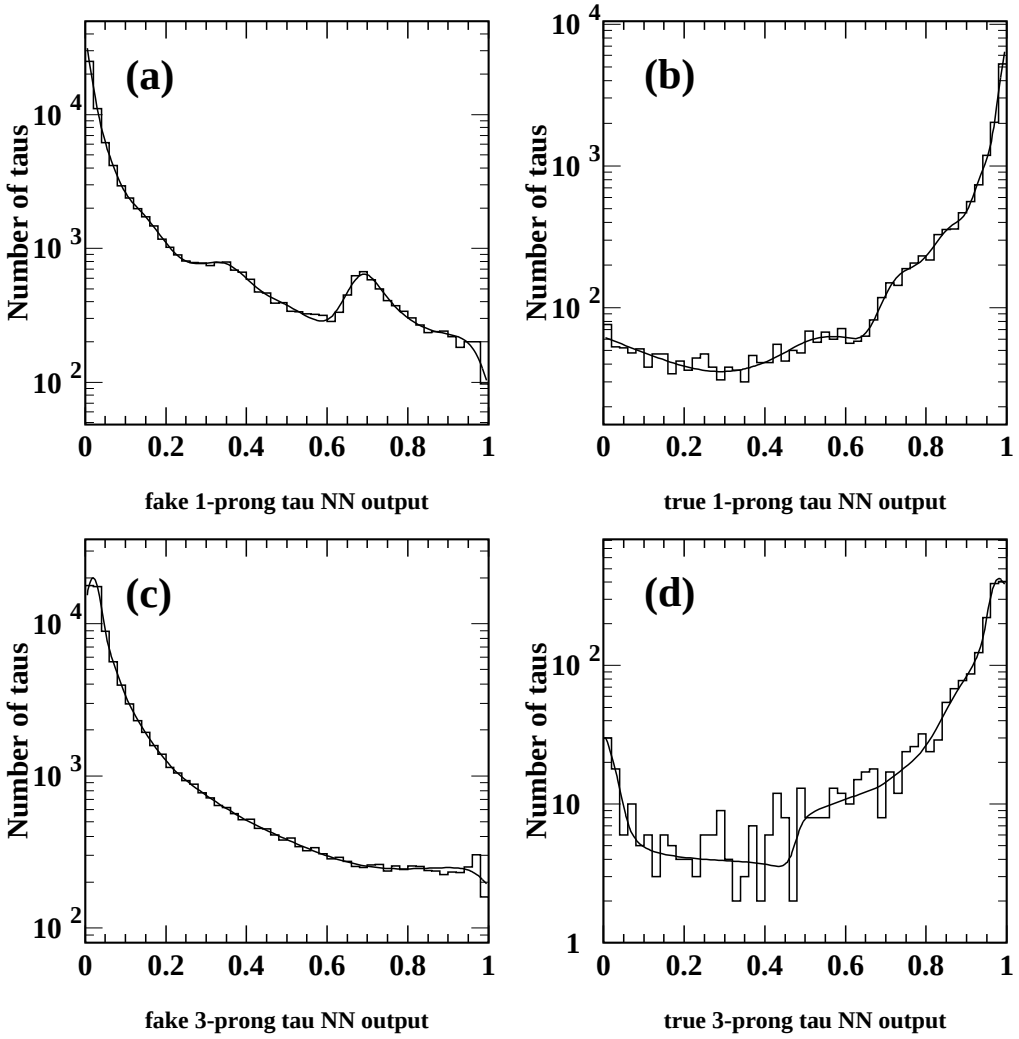

Figure 4.3: Distributions of the τ-ID neural network output for true taus and fakes. The curve shows the fits to the distributions used to construct the f_i's in Equation 4.1.

i	ϵ_i	$\mathcal{F}_i$
1-prong	0.771	1.22
3-prong	0.602	1.28

Table 4.1: The additional factors entering Equation 4.1.

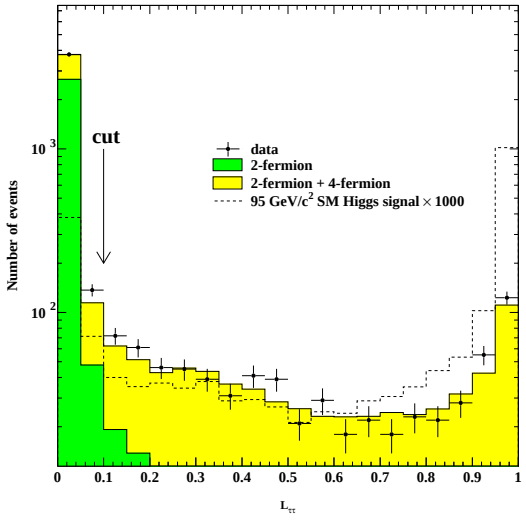

Figure 4.4: Distributions of $\mathcal{L}_{\tau\tau}$ (Equation 4.2) for signal, background, and data. The signal has been scaled up by a factor of 1000 for visibility.

Taking the oppositely-charged tau candidates with the highest $\mathcal{P}$'s, the following two-tau likelihood[1] is constructed:

$$\mathcal{L}_{\tau\tau} = \frac{\mathcal{P}_+\mathcal{P}_-}{\mathcal{P}_+\mathcal{P}_- + (1-\mathcal{P}_+)(1-\mathcal{P}_-)} \tag{4.2}$$

This quantity is shown in Figure 4.4. By requiring $\mathcal{L}_{\tau\tau} > 0.1$, 96% of the $(Z/\gamma)^* \to q\bar{q}$ background is removed.

[1]See Section 4.1.5 for a discussion on likelihoods.

4.1.3 Kinematic Fitting

After having identified the tau pair,[2] the rest of the event is forced into two jets using the Durham jet-finding algorithm [42]. Due to detector resolution (and fragmentation effects in the case of the jets), the reconstructed jets and taus do not perfectly reflect the momenta of the parent quarks and taus, as shown in Figure 4.5. In particular, the tau momentum is almost always underestimated due to the energy carried away by the neutrinos produced in its decay. To improve the resolution on the tau/jet four-momenta (and hence the resolution on the invariant masses reconstructed from these four-momenta), a kinematic fit along the lines of that described in [43] is performed, where $\mathrm{W^+W^-} \to \mathrm{q\bar{q}'}\tau\nu_\tau$ events were fitted in a hybrid scheme in which taus could be treated like hadron jets if

1. the visible tau decay products were used to define the tau direction, and

2. the energy of the tau was first estimated using energy-momentum conservation.

The first point is made possible by the fact that the taus are highly boosted and therefore their decay products are well-collimated around the tau flight direction. The second point is achieved here by treating the taus and jets as massless particles and solving the following matrix equation for four energy rescaling factors c_i:

$$\begin{pmatrix} p_x^{j_1} & p_x^{j_2} & p_x^{\tau_1} & p_x^{\tau_2} \\ p_y^{j_1} & p_y^{j_2} & p_y^{\tau_1} & p_y^{\tau_2} \\ p_z^{j_1} & p_z^{j_2} & p_z^{\tau_1} & p_z^{\tau_2} \\ E^{j_1} & E^{j_2} & E^{\tau_1} & E^{\tau_2} \end{pmatrix} \begin{pmatrix} c_1 \\ c_2 \\ c_3 \\ c_4 \end{pmatrix} = \begin{pmatrix} 0 \\ 0 \\ 0 \\ \sqrt{s} \end{pmatrix} \tag{4.3}$$

Here the p's and E's refer to the visible, measured energy of the taus and jets. After this calculation the energy of tau i is taken to be $c_{i+2}E^{\tau_i}$; the magnitude of the momentum is $\sqrt{(c_{i+2}E^{\tau_i})^2 - m_\tau^2}$. As can be seen in Figures 4.5 and 4.6, the true tau

[2]Recall that the tau candidates are single tracks or trios of tracks. At this stage we also identify all tracks and clusters within a cone of 10° half-angle around the candidate seed track as belonging to the tau.

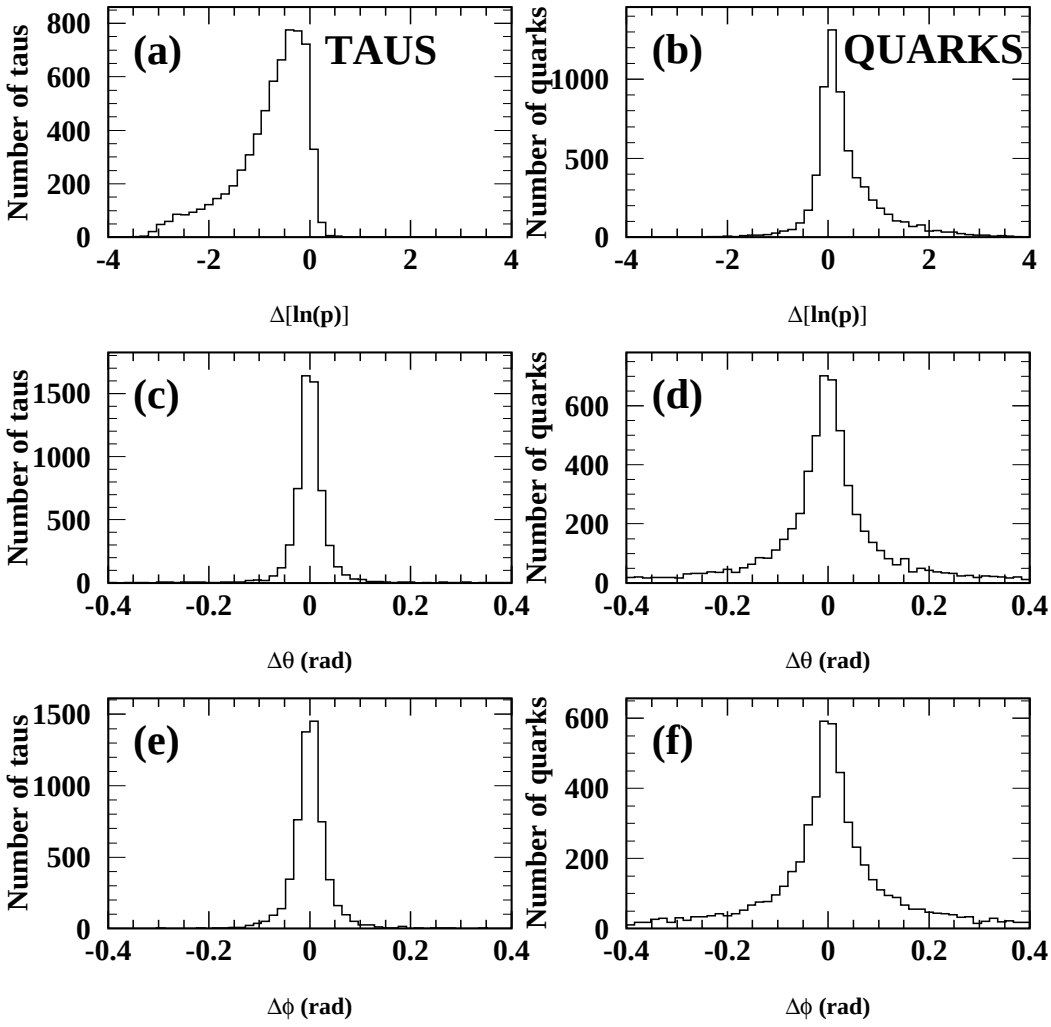

Figure 4.5: The residual errors on the momentum of taus (left column) and quarks (right column) in $H^0Z^0 \to \tau^+\tau^- q\bar{q}$ events (m_H= 95 GeV/c^2) using the quantities measured in the detector. Each plot shows $x_{meas} - x_{true}$ for the variable in question.

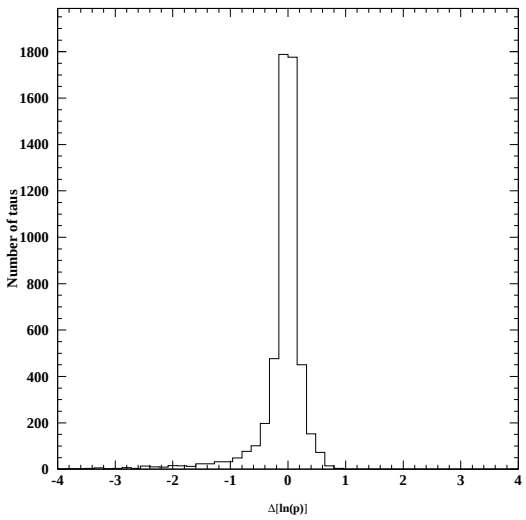

Figure 4.6: The residual error on tau momentum after application of the energy rescaling procedure described in Section 4.1.3.

energy[3] and direction is reproduced after this procedure at least as accurately as the measured jet momenta reproduce those of their parent quark.

After this procedure the measured jet momenta and rescaled tau momenta are subjected to the following three kinematic fits:

1. **The 2C fit.** Energy and momentum conservation are required; however, two of these four constraints are lost due to the prior use of energy-momentum conservation in determining the rescaled tau energies.

2. **The $3C_1$ fit.** In addition to energy-momentum conservation, the invariant mass of the jet pair is constrained to the Z^0 mass.

3. **The $3C_2$ fit.** This is the same as the $3C_1$ fit, except the invariant mass of the tau pair is constrained to the Z^0 mass instead of the jets.

Events wholly inconsistent with the $q\bar{q}\tau^+\tau^-$ kinematic hypothesis can be rejected by requiring a sensible solution to Equation 4.3 (all the c_i's should be positive and

[3]The figures show the residual error on $\ln p$, the variable actually used in the kinematic fit. It was found that this variable has a more Gaussian-like error distribution than that of E.

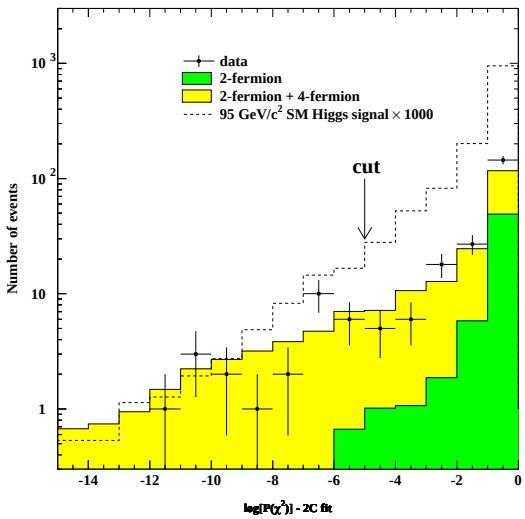

Figure 4.7: Distributions of the base-10 logarithm of the χ^2 probability for the 2C kinematic fit. The signal has been scaled up by a factor of 1000 for visibility.

the rescaled tau energies should be greater than m_τ) and requiring the 2C fit χ^2 probability to be greater than 10^{-5} (see Figure 4.7). Examples of the kinds of events that fail these criteria are events with significant undetected ISR and $\mathrm{q\bar{q}}'\ell\nu_\ell$ events where the neutrino carries away a large fraction of the energy.

One can check the validity of the fits by looking at the χ^2 probability distribution for simulated signal events that satisfy the kinematic hypothesis under consideration, as shown in Figure 4.8. Ideally this would be a flat distribution between 0 and 1; however, the fit assumes Gaussian-distributed errors on the input momenta. Therefore the tails in the distributions of Figures 4.5 and 4.6 show up as a pile-up of events with probability near zero in Figure 4.8.

4.1.4 One Other Cut

Before moving to the final stage of the analysis, one more cut is made for events in which both tau candidates are identified as 1-prong decays. In this case the sum of the measured energies of the two charged particles is required to be less than 80 GeV. This cut specifically reduces the background from $\mathrm{Z^0Z^0} \to \ell^+\ell^-\mathrm{q\bar{q}}$ ($\ell = \mathrm{e}, \mu$), where

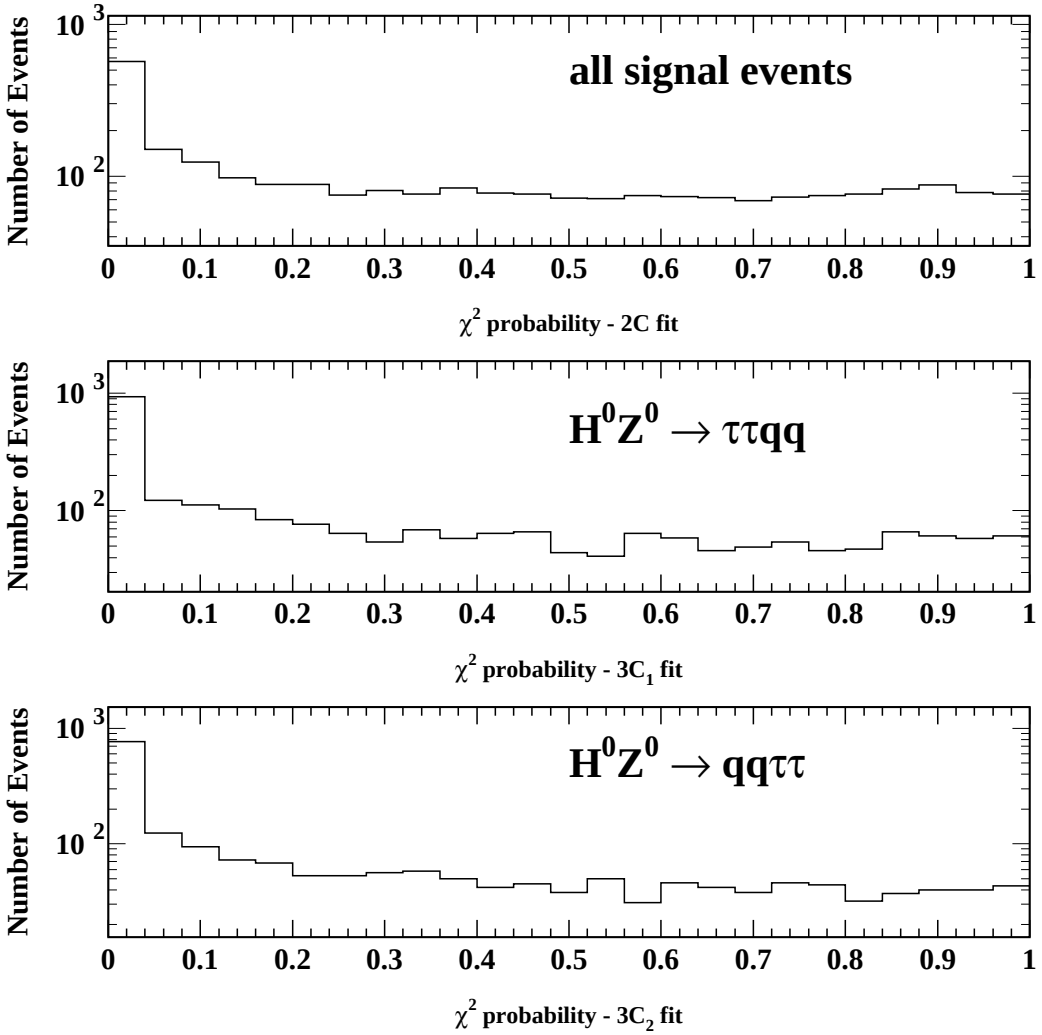

Figure 4.8: χ^2 probability distributions of kinematic fits for signal events.

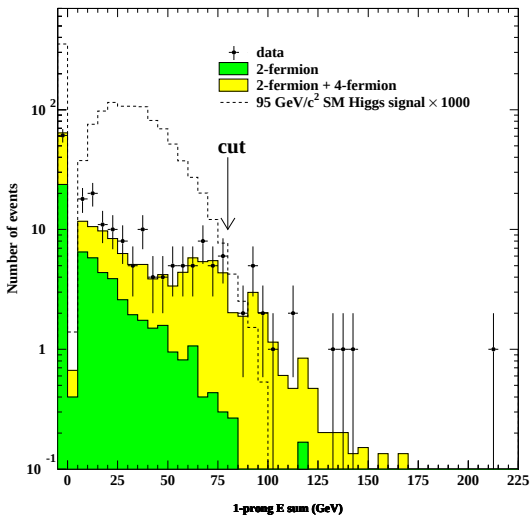

Figure 4.9: Distributions of the sum of the energies of the charged particles identified as two 1-prong tau decays. The signal has been scaled up by a factor of 1000 for visibility. Events with 3-prong taus are piled into the first ($E < 0$) bin.

the $\ell^+\ell^-$ pair carries away all the energy of the Z^0; true tau decay products will of course be softer due to the sharing of energy with neutrinos. This cut is shown in Figure 4.9.

4.1.5 Likelihood Selection

To identify signal-like events efficiently, a number of discriminating variables are used together in a multivariate relative likelihood calculation. The likelihood technique is an application of Bayes' theorem, which states that if $P(x|y)$ is the probability of observing x given y ("conditional probability"), and $P(x)$ is the probability of observing x regardless of the value of y ("marginal probability"),

$$P(x|y) = \frac{P(y|x)P(x)}{\int P(y|x)P(x)dx} \tag{4.4}$$

For our purposes, x is identified with an event class, i.e. either "signal," "four-fermion background," or "two-fermion background." y is identified with a configuration of event variables $\{y_1, y_2, \ldots, y_n\}$. If, for a given event class x, the y_i's are

plotted in normalized histograms (called "reference histograms") such that $h_i(y_i)$ is the content of the histogram bin in which y_i falls, then $P(y|x)$ can be expressed as $\prod_{i=1}^{n} h_i(y_i)$ if the y_i's are uncorrelated. Here, the following variables are used:

1. R_{vis}, the ratio of the total visible energy to $\sqrt{s}$
2. $\cos\theta_{miss}$
3. $\log y_{34}$, where y_{34} is value of y_{cut} where the number of jets found in the event changes from 3 to 4 in the Durham algorithm (allowing taus to be identified as low-multiplicity jets)
4. E^{ℓ}_{max}, the energy of the highest-energy lepton (electron or muon) in the event. The leptons are identified using standard algorithms described in [44] and [45].
5. The angle between the τ^- and the nearest jet
6. The angle between the τ^+ and the nearest jet
7. The base-10 logarithm of the largest of the two 3C fit χ^2 probabilities
8. $1-\sqrt{1-\mathcal{L}_{\tau\tau}}$
9. $1-\sqrt{1-\mathcal{B}_{2jet}}$, where $\mathcal{B}_{2jet}$ is the b-tagging discriminant described in Appendix A
10. $\sqrt{P_J}$, where P_J is the tau pair's impact parameter significance joint probability (see Appendix B)

Note that a few variables have transformations (such as $1-\sqrt{1-x}$) applied to them in order to expand the sensitive regions of their distributions.

One of the subtleties of the SM Higgs tau channel signal is that about half of it does not carry b-flavor. Of the half that does, about two-thirds comes from $H^0Z^0 \to b\bar{b}\tau^+\tau^-$ and one-third from $H^0Z^0 \to \tau^+\tau^- b\bar{b}$. To address this, two likelihoods, $\mathcal{L}_{b\bar{b}\tau^+\tau^-}$ and $\mathcal{L}_{q\bar{q}\tau^+\tau^-}$, are constructed. $\mathcal{L}_{q\bar{q}\tau^+\tau^-}$ does not include the $\mathcal{B}_{2jet}$

variable and only non-b-flavored events are used to construct its signal reference histograms, whereas $\mathcal{L}_{\mathrm{b\bar{b}}\tau^+\tau^-}$ uses b-flavored events and does include $\mathcal{B}_{\mathrm{2jet}}$. The signal reference histograms for both likelihoods use a mixture of Higgs masses (85, 90, and 95 GeV/c^2) so as not to introduce a bias toward any one particular mass. The reference histograms for both likelihoods are shown in Figures 4.10 and 4.11.

The signal likelihood is then calculated as follows (where $\mathrm{b\bar{b}}\tau^+\tau^-$ or $\mathrm{q\bar{q}}\tau^+\tau^-$ is represented with the generic j):

$$\mathcal{L}_j = \frac{\prod_{i=1}^{n_j} h_i^j(y_i)}{\prod_{i=1}^{n_j} h_i^j(y_i) + \prod_{i=1}^{n_j} h_i^{\mathrm{2f}}(y_i) + \frac{\sigma_{\mathrm{4f}}^{\mathrm{acc}}}{\sigma_{\mathrm{2f}}^{\mathrm{acc}}} \prod_{i=1}^{n_j} h_i^{\mathrm{4f}}(y_i)} \tag{4.5}$$

One can note the similarity in form to Equation 4.4; however the marginal probabilities for the different event classes ($P(x)$ in Equation 4.4), which are related to their different accepted cross sections, have been set to 1. This is because the Higgs cross section is a function of the Higgs mass under consideration; the only consequence is that the likelihood can not be interpreted as a strict probability. The cross sections of the two different background classes are well-defined, however, and the ratio of the two is used to give the backgrounds the appropriate relative weight in the calculation. The distributions of $\mathcal{L}_{\mathrm{q\bar{q}}\tau^+\tau^-}$ and $\mathcal{L}_{\mathrm{b\bar{b}}\tau^+\tau^-}$ are shown in Figure 4.12.

Events were selected as candidates if $\mathcal{L}_{\mathrm{b\bar{b}}\tau^+\tau^-} > 0.92$ or $\mathcal{L}_{\mathrm{q\bar{q}}\tau^+\tau^-} > 0.88$. These cuts were chosen such that σ_{95} was minimized, where σ_{95} is the Higgs production cross section that can be excluded at 95% confidence level in a simple event-counting experiment as described in Section 29.6.4 of [46].

4.1.6 Performance

The SM analysis is summarized in Table 4.2. A slight discrepancy between data and Monte Carlo, never amounting to more than 2.9σ, is seen throughout due to imperfect modelling of the cut variables. This is addressed in the assignment of a systematic uncertainty on the background expectation that covers this discrepancy

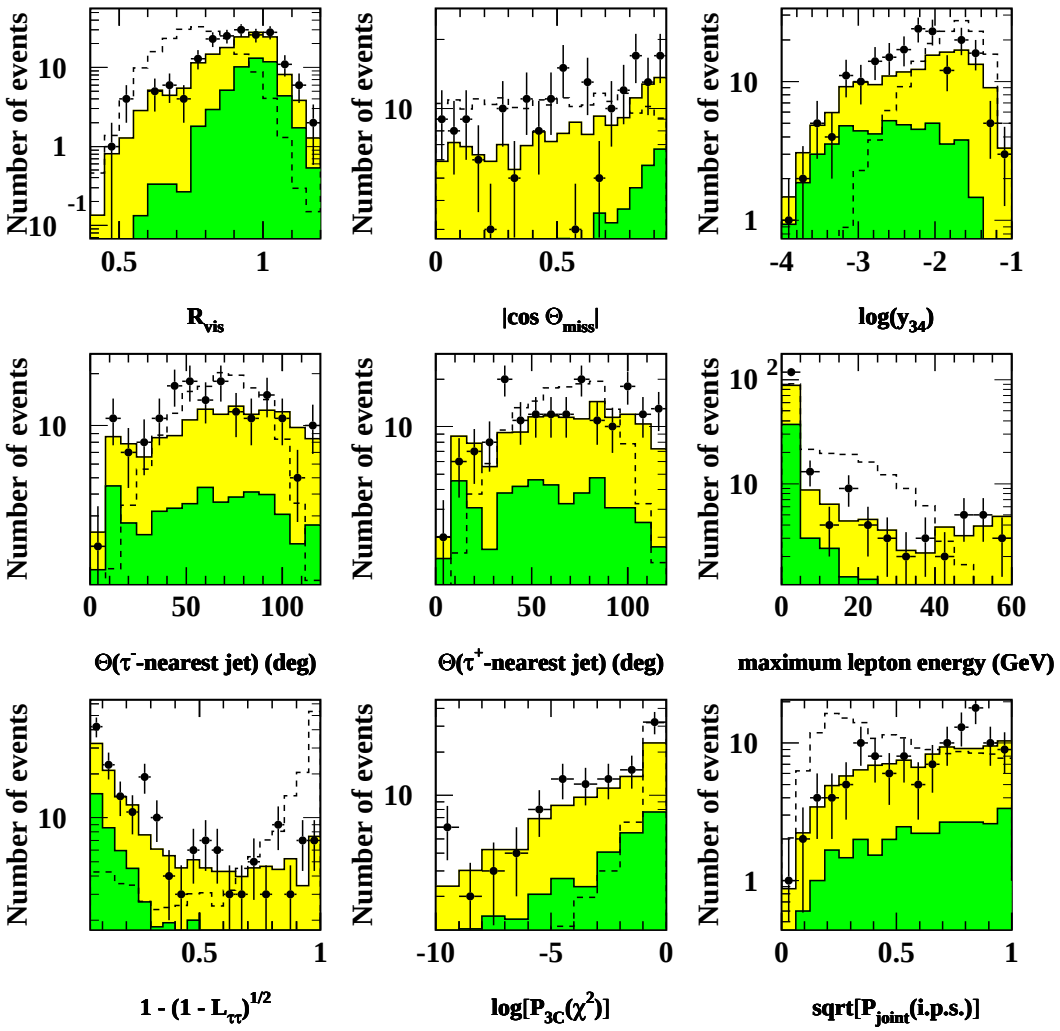

Figure 4.10: $\mathcal{L}_{q\bar{q}\tau^+\tau^-}$ reference histograms for four-fermion background (yellow/light grey), two-fermion background (green/dark grey), and signal (open dashed). Here the background histograms are normalized to the same luminosity as the data (shown as points) to illustrate the data-Monte Carlo agreement. The signal histogram normalization is arbitrary. In the actual likelihood calculation all histograms are normalized to unity.

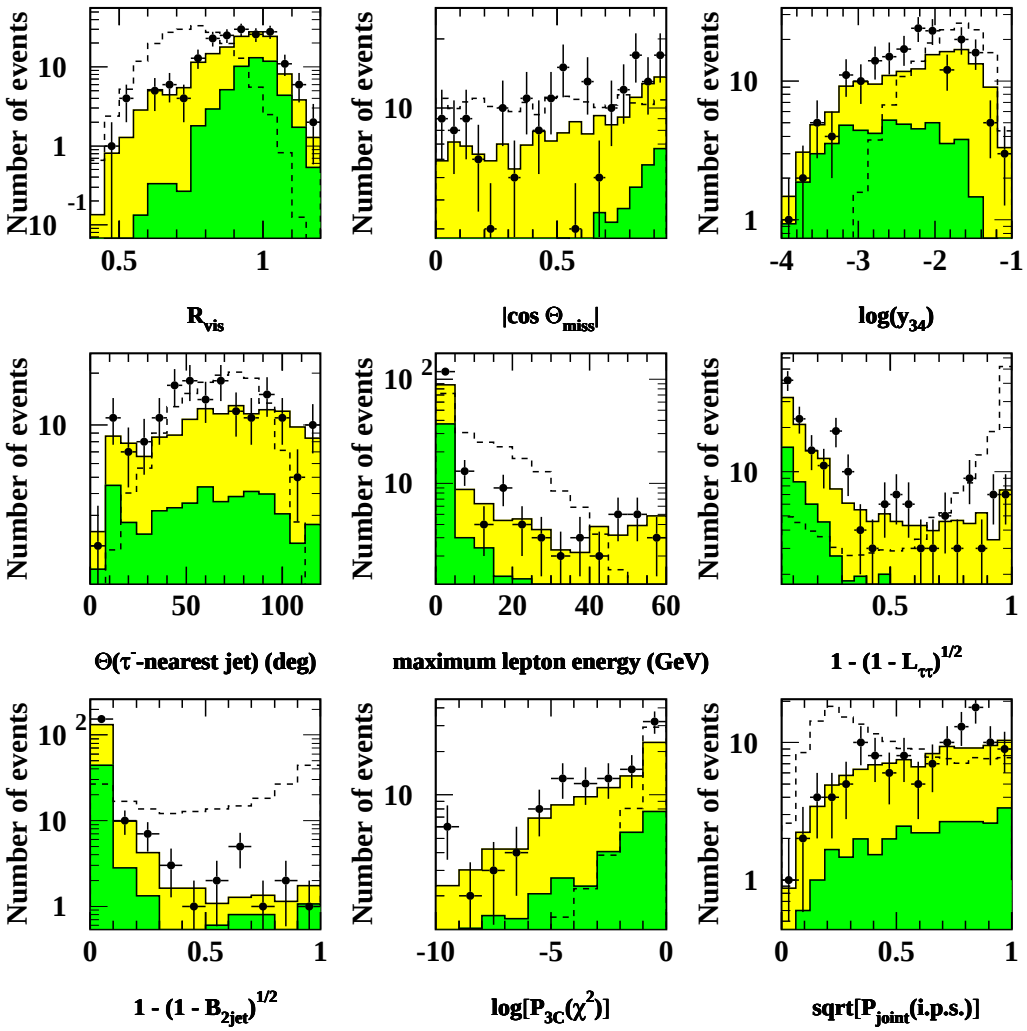

Figure 4.11: $\mathcal{L}_{b\bar{b}\tau^+\tau^-}$ reference histograms for four-fermion background (yellow/light grey), two-fermion background (green/dark grey), and signal (open dashed). The $\theta(\tau^+ - \text{nearest jet})$ variable has been suppressed for presentation purposes. Here the background histograms are normalized to the same luminosity as the data (shown as points) to illustrate the data-Monte Carlo agreement. The signal histogram normalization is arbitrary. In the actual likelihood calculation all histograms are normalized to unity.

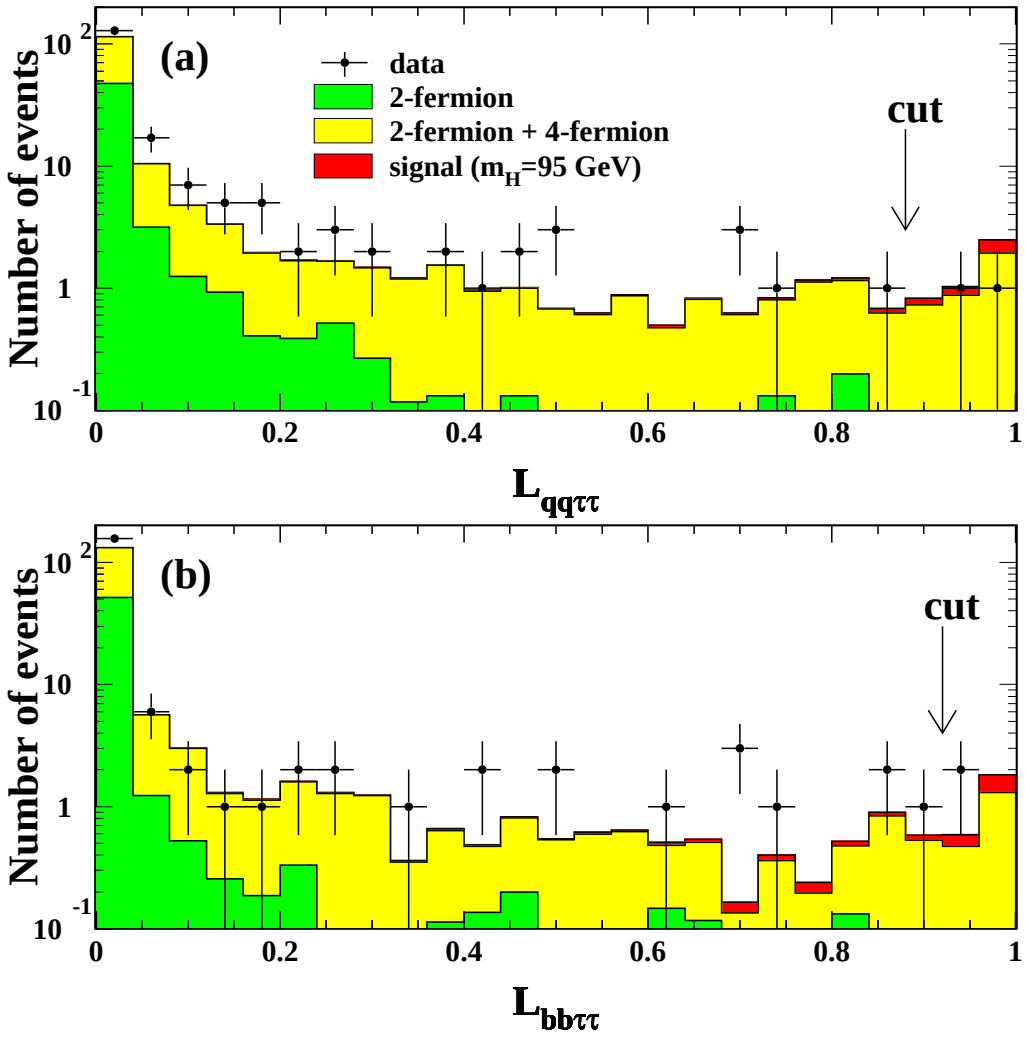

Figure 4.12: Distributions of (a) $\mathcal{L}_{q\bar{q}\tau^+\tau^-}$ and (b) $\mathcal{L}_{b\bar{b}\tau^+\tau^-}$. The expected signal is shown added to the total background.

cut	data	total bkgd.	4f	2f	2γ	efficiency (%)
(1) preselection cuts	4652	4580±20	1766.8	2808.5	8.3	80.4
(2) $\mathcal{L}_{\tau\tau} > 0.1$	733	693±7	590.4	100.0	2.6	62.3
(3) $P_{2C}(\chi^2) > 10^{-5}$	201	160±3	103.6	55.7	0.3	50.3
(4) 1-p E sum < 80 GeV	185	156±3	100.5	55.2	0.3	50.0
(5) Final $\mathcal{L}$'s	3	4.0±0.5	3.9	0.1	0.0	34.4 ± 1.1

Table 4.2: Cut flow table for the SM analysis. Cut n is described in detail in Section 4.1.n. 4f, 2f, and 2γ refer to the individual four-fermion, two-fermion, and two-photon backgrounds respectively. The efficiency shown is for $m_{\mathrm{H}} = 95$ GeV/c^2 and the errors are statistical only.

(see Section 4.1.7). For a 95 GeV/c^2 SM Higgs boson, the analysis has a signal efficiency of $(34.4 \pm 1.1 \pm 2.4)\%$, where the first error is statistical and the second is systematic (see Section 4.1.7). This corresponds to about 0.9 signal events expected in the data. Efficiencies for other Higgs masses are tabulated in detail in Table 4.3. The overlap between the two likelihoods ($\mathcal{L}_{\mathrm{b\bar{b}}\tau^+\tau^-}$ and $\mathcal{L}_{\mathrm{q\bar{q}}\tau^+\tau^-}$) is shown in Figure 4.13. A high degree of correlation is seen, but Table 4.4 shows quantitatively that the two-

m_{H}	efficiency (%)		
(GeV/c^2)	$\mathrm{Z}^0 \to \mathrm{q\bar{q}}$, $\mathrm{H}^0 \to \tau^+\tau^-$	$\mathrm{Z}^0 \to \tau^+\tau^-$, $\mathrm{H}^0 \to$ all	total
30	9.7	15.1	11.9 ± 0.7
40	16.7	20.9	18.4 ± 0.9
50	19.0	27.0	22.2 ± 0.9
60	26.5	29.1	27.5 ± 1.0
65	27.4	28.4	27.8 ± 1.0
70	27.9	34.5	30.5 ± 1.0
75	30.5	32.8	31.4 ± 1.1
80	29.1	35.0	31.3 ± 1.1
85	31.5	34.8	32.8 ± 1.1
90	34.2	35.1	34.6 ± 1.1
95	32.8	37.0	34.4 ± 1.1
100	27.7	30.9	28.9 ± 1.0

Table 4.3: Signal efficiencies for various SM Higgs masses. The total tau channel efficiency (column 4) is the branching-ratio-weighted average of the channel efficiencies shown in columns 2 and 3. The errors are statistical only.

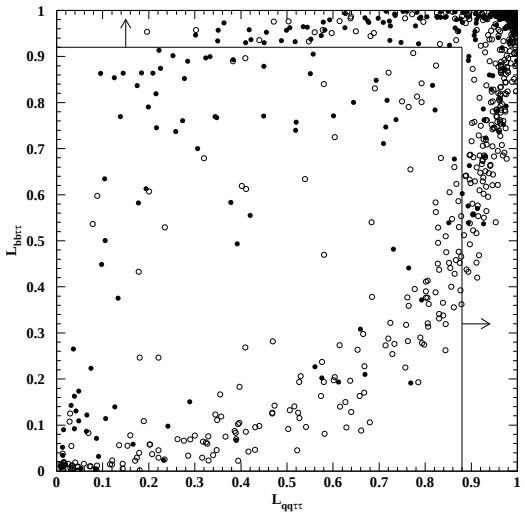

Figure 4.13: $\mathcal{L}_{b\bar{b}\tau^+\tau^-}$ vs. $\mathcal{L}_{q\bar{q}\tau^+\tau^-}$ for 95 GeV/c^2 SM Higgs events. Filled circles are $b\bar{b}\tau^+\tau^-$ events, while open circles are $q\bar{q}\tau^+\tau^-$ events (q = u, d, s, c). The arrows show the area retained by the likelihood cuts.

	$bb\tau^+\tau^-$ events	$q\bar{q}\tau^+\tau^-$(non-b) events
selected by $\mathcal{L}_{b\bar{b}\tau^+\tau^-}$ only	23%	1%
selected by $\mathcal{L}_{q\bar{q}\tau^+\tau^-}$ only	7%	58%
selected by both	70%	41%

Table 4.4: A breakdown of how 95 GeV/c^2 SM Higgs events are selected by the two likelihoods described in Section 4.1.5.

likelihood approach recovers a significant amount of signal that would be lost by using $\mathcal{L}_{b\bar{b}\tau^+\tau^-}$ or $\mathcal{L}_{q\bar{q}\tau^+\tau^-}$ alone.

Three events are selected in the 168.7 pb^{-1} of data collected at $\sqrt{s} = 189$ GeV, consistent with the $4.0 \pm 0.5(\text{stat.}) \pm 0.9(\text{syst.})$ events expected from SM background. For each event a Higgs mass is reconstructed from the invariant mass of either the tau pair or the jet pair, depending on which of the two 3C kinematic fits has the larger χ^2 probability. The expected distribution of this mass for SM background events is shown in Figure 4.14. One can see the expected peak at $m_{\text{rec}} = m_{\text{Z}}$ due to the irreducible $Z^0Z^0 \to q\bar{q}\tau^+\tau^-$ background. The masses of the three candidates are also

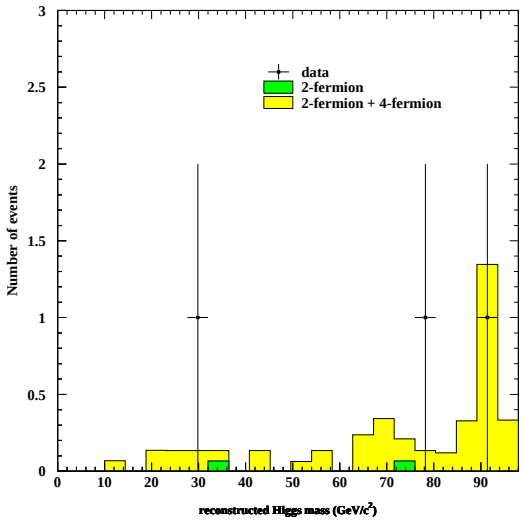

Figure 4.14: Reconstructed Higgs mass distribution for selected SM background events.

Event	selected as	m_{H} (GeV/c^2)	m_{Z} (GeV/c^2)	$\mathcal{L}_{\mathrm{b\bar{b}}\tau^+\tau^-}$	$\mathcal{L}_{\mathrm{q\bar{q}}\tau^+\tau^-}$	$\mathcal{B}_{\mathrm{2jet}}$	$\mathcal{L}_{\tau\tau}$
1	$\mathrm{H^0Z^0} \to \mathrm{q\bar{q}}\tau^+\tau^-$	79.5	92.4	0.71	0.94	0.00	1.00
2	$\mathrm{H^0Z^0} \to \tau^+\tau^-\mathrm{q\bar{q}}$	29.7	94.8	0.95	0.48	0.91	0.10
3	$\mathrm{H^0Z^0} \to \tau^+\tau^-\mathrm{q\bar{q}}$	89.4	90.6	0.94	0.99	0.04	1.00

Table 4.5: Some characteristics of the three SM Higgs candidate events. The m_{Z} shown is reconstructed after the 2C kinematic fit, whereas the m_{H} shown is reconstructed after the appropriate 3C fit.

shown in this plot, as well as listed in Table 4.5. It should be noted that the expected resolution on the Higgs mass is around 2–3 GeV/c^2, as shown in Figure 4.15.

4.1.7 Systematic Uncertainties

The two "workhorses" of the analysis, in terms of signal and background separation, are clearly the b- and tau-tagging. Therefore the systematic uncertainties associated with these techniques need to be addressed. The following sources of uncertainty were investigated.

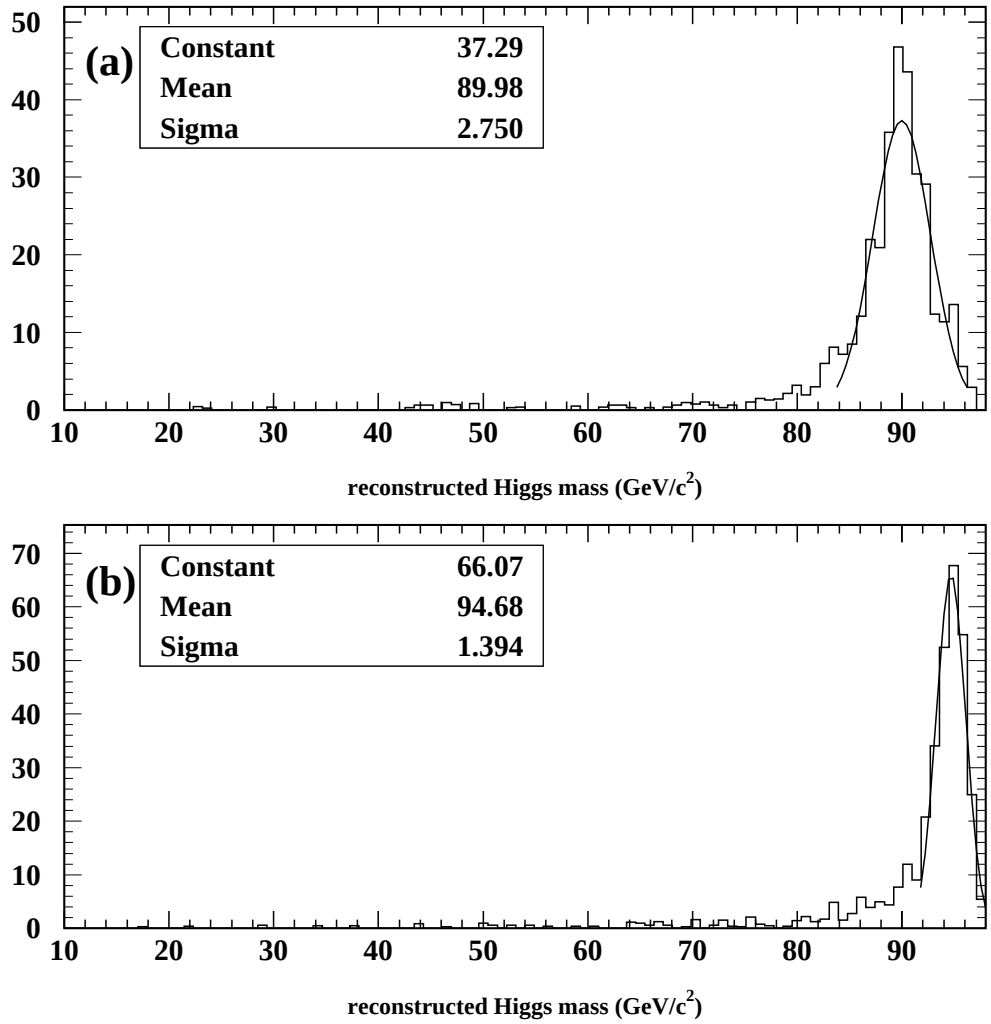

Figure 4.15: Reconstructed Higgs mass for selected signal events with (a) $m_{\mathrm{H}} = 90$ GeV/c^2 and (b) $m_{\mathrm{H}} = 95$ GeV/c^2. The tails to lower masses arise from events where one tau was misidentified. The Gaussian fits are shown to give an idea of the mass resolution; the normalization is arbitrary.

- ***B* decay multiplicity:** Relying as heavily as it does on secondary vertexing, b-tagging is sensitive to the charged multiplicity of B decays. The current 1σ uncertainty on the average multiplicity is 0.062 [47], so Monte Carlo events were reweighted according to their B decay multiplicities so as to effectively shift their average by this amount. Analyzing the reweighted events yields a 1% effect on the final signal and background expectations, which is taken as the systematic uncertainty.

- **b fragmentation:** The average fraction of energy carried by the B hadron in a b jet has an uncertainty of about ± 0.008 [47], so again Monte Carlo events were reweighted so as to shift the average by this amount. Analyzing the reweighted events shows a 1.5% relative effect on the efficiency and a 5% effect on the background expectation.

- **Tracking modelling:** Monte Carlo events were re-reconstructed after smearing track parameters in the $r - \phi$ plane by 5% and the z direction by 10%, corresponding to the observed resolution on these quantities. This results in a 1% difference in efficiency and 4% difference in expected background.

- **Tau polarization:** The signal Monte Carlo samples were generated with a bug that caused the taus to have the incorrect polarization. The bug was fixed and new samples were produced and compared with the samples used to determine the efficiency. A 5% relative difference was seen and assigned as a systematic error.

- **Different Monte Carlo generators:** The total expected background was compared using EXCALIBUR (vs. grc4f) for the four-fermion background and HERWIG (vs. PYTHIA) for the $q\bar{q}$ background. The difference (3%) was taken as the systematic error.

- **Tau ID:** As discussed in Section 3.6, the tau ID neural network has a 3% systematic uncertainty associated with its efficiency and a 10% uncertainty associated with its fake rate. For the signal, then, the 3% efficiency uncertainty is simply assigned twice (once for each tau).

cut	data	total bkgd.	ratio data/MC
preselection cuts	4889	4864±18	1.01 ± 0.01
$\mathcal{L}_{\tau\tau} > 0.1$	611	571±6	1.07 ± 0.05
$P_{2C}(\chi^2) > 10^{-5}$	179	144±3	1.24 ± 0.09
1-p E sum < 80 GeV	173	141±3	1.23 ± 0.10
Final $\mathcal{L}$'s	1	1.4±0.3	n/a

Table 4.6: Cut flow table for events with a like-signed tau pair. The errors are statistical only. No final ratio is given due to the lack of statistics necessary to make a meaningful comparison.

The background is a mixture of events with two, one, and zero real taus. Since the tau ID is insensitive to the charge of the tau, by selecting events with a like-signed tau pair we can use the data to cross-check that portion of the background where one or both of the taus is a fake. Table 4.6 shows the cut flow for this "fake-enriched" data sample. The overall discrepancy of 23% after the final pre-likelihood cut is taken as the systematic error on this portion of the background. For the portion with two real taus, we make the conservative assumption that the 19% discrepancy observed after the final pre-likelihood cut in Table 4.2 is due entirely to kinematics mismodelling and that this should be added in quadrature to the two 3% efficiency uncertainties associated with the identification of the real tau pair, leading to an uncertainty of 20% on this portion of the background. Using the "bottom-line" Monte Carlo background expectations from Tables 4.6 and 4.2 to assess the relative rates of these two backgrounds, we add their uncertainties and arrive at a final uncertainty on the total background of 21%.

The systematic errors are summarized in Table 4.7.

4.2 Searches for MSSM Higgs Bosons

In this section we describe how the Standard Model Higgs search is extended to look for Higgs bosons of the MSSM. Recall from Section 1.5.3 that MSSM Higgs

Source	Signal	Background
B multiplicity	1%	1%
b fragmentation	2%	5%
tracking modelling	1%	4%
tau ID	4%	21%
tau polarization	5%	n/a
MC generators	n/a	3%
Total	7%	22%
MC statistics	3%	13%

Table 4.7: Systematic uncertainties on signal and background listed by source.

bosons can be produced either via Higgsstrahlung ($e^+e^- \to h^0Z^0$) or pair-production ($e^+e^- \to h^0A^0$).

4.2.1 The Higgsstrahlung Process

Because of the similarity in decay properties of the h^0 and H^0 to those of H^0_{SM}, the SM Higgs search described in Section 4.1 can be recycled and reinterpreted as a search for $e^+e^- \to h^0Z^0$ (and $e^+e^- \to H^0Z^0$ if it is kinematically accessible). However, if $m_h > 2m_A$, the decay channel $h^0 \to A^0A^0$ opens up and may in fact be dominant. In this scenario we get final states like $f\bar{f}b\bar{b}b\bar{b}$, $f\bar{f}b\bar{b}\tau^+\tau^- \ldots$ where the $f\bar{f}$ arises from the Z^0 decay. The case where the A^0's decay to $b\bar{b}$ has the largest branching ratio, and due to the large boost of the light A^0's, the two $b\bar{b}$ pairs will often collapse to form two "fat" jets. When the Z^0 decays to a tau pair, we then arrive at a $q\bar{q}\tau^+\tau^-$ topology similar to one searched for in the SM. In fact, since the "fat" jets each contain in principle two displaced vertices, it is still possible to tag their b-flavor. Therefore, the SM Higgs search should retain a respectable (although certainly not optimal) efficiency for this process. Efficiencies for several values of m_h and m_A are shown in Table 4.8.

m_{h} (GeV/c^2)	m_{A} (GeV/c^2)	Efficiency
20	10	7.4%
40	10	12.4%
60	10	21.6%
80	10	30.2%
40	20	24.4%
50	20	24.8%
70	20	38.0%
60	30	31.2%
80	30	31.8%
80	40	33.2%

Table 4.8: Efficiencies for the process $\mathrm{Z^0h^0} \to \mathrm{Z^0A^0A^0} \to \tau^+\tau^-\mathrm{b\bar{b}b\bar{b}}$.

4.2.2 Pair Production

The process $\mathrm{h^0A^0} \to \mathrm{b\bar{b}}\tau^+\tau^-$ ($\tau^+\tau^-\mathrm{b\bar{b}}$) is kinematically and topologically similar to the Higgsstrahlung process, except for the loss of the $\mathrm{Z^0}$ mass constraint. Therefore the SM search is recycled up until the construction of the final likelihood. A new likelihood ($\mathcal{L}_{\mathrm{hA}}$) is constructed using the same variables as the SM $\mathcal{L}_{\mathrm{b\bar{b}}\tau^+\tau^-}$ likelihood, with the following differences:

1. The signal reference histograms are constructed from simulated $\mathrm{h^0A^0}$ events, using a large variety of $\mathrm{h^0}$ and $\mathrm{A^0}$ masses.

2. The 3C fit probability variable is dropped.

3. A new variable, $< |\cos\theta_{\mathrm{dijet}}| >$, is introduced to partially compensate for the loss of the powerful m_{Z} constraint in the SM analysis. This variable is the average of the absolute values of the polar angles of the $\mathrm{b\bar{b}}$ system and the $\tau^+\tau^-$ system. It represents the $\mathrm{h^0A^0}$ production angle, and since the dominant backgrounds ($\mathrm{W^+W^-}$, $\mathrm{Z^0Z^0}$) are mainly t-channel processes, their distributions will be more forward-peaked than the signal. This can be seen in Figure 4.16.

Distributions of $\mathcal{L}_{\mathrm{hA}}$ are shown in Figure 4.17. A cut requiring $\mathcal{L}_{\mathrm{hA}} > 0.64$ selects seven events in the data, with $4.9 \pm 0.6(\mathrm{stat.}) \pm 1.6(\mathrm{syst.})$ events expected from SM

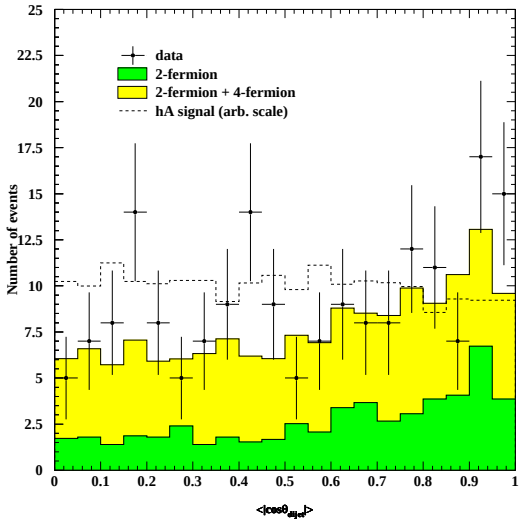

Figure 4.16: Distributions of $< |\cos\theta_{\rm dijet}| >$ for signal, background, and data. The normalization of the signal histogram is arbitrary.

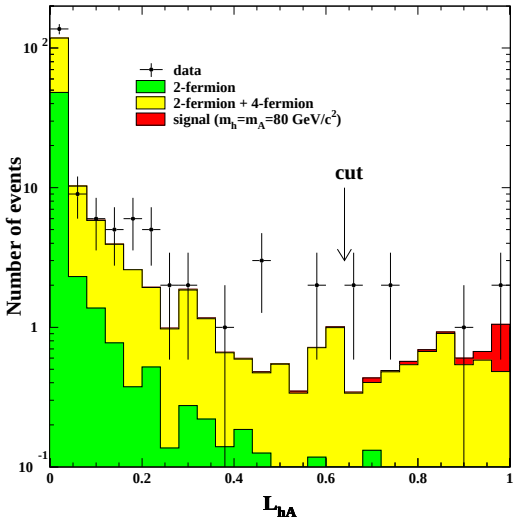

Figure 4.17: Distributions of $\mathcal{L}_{\rm hA}$. The expected signal (see footnote, page 101) is shown added to the total background.

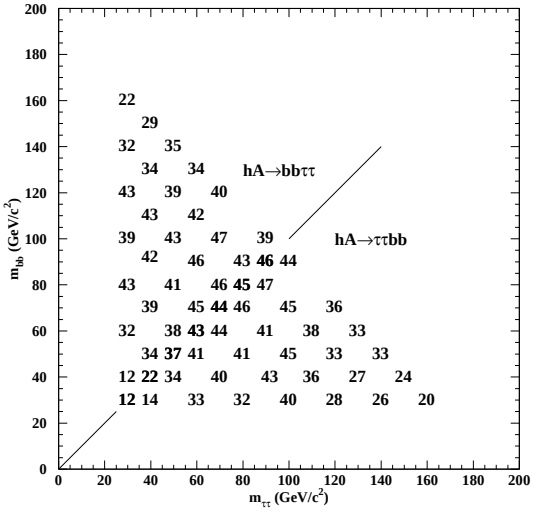

Figure 4.18: h^0A^0 signal efficiencies (in %) for various h^0 and A^0 masses.

background. The efficiency for $m_h = m_A = 80$ GeV/c^2 is $(45.3 \pm 1.5(\text{stat.}) \pm 2.3(\text{syst.}))\%$, corresponding to about 0.8 signal events expected in the data.[4] Efficiencies for other masses are shown in Figure 4.18. The expected distribution of the *sum* of the $b\bar{b}$ and $\tau^+\tau^-$ masses (since it is impossible to distinguish $h^0A^0 \to b\bar{b}\tau^+\tau^-$ and $h^0A^0 \to \tau^+\tau^- b\bar{b}$) is shown in Figure 4.19 for simulated background events, along with the mass sums for the candidates observed in the data. The expected resolution on the mass sum for signal events is shown in Figure 4.20, along with the resolution on the mass difference. Systematic uncertainties on the signal and background expectations are evaluated in the same way as Section 4.1.7.

4.3 Flavor-Independent Higgsstrahlung Search

In a general Type II Two Higgs Doublet Model (see Section 1.4), the Higgs coupling to down-type fermions can be suppressed with suitable choices of the free parameters α and $\tan\beta$. In this case, $h^0 \to c\bar{c}$ and $h^0 \to gg$ dominate the hadronic Higgs

[4]To calculate the signal rate, one must first choose a set of MSSM parameters to work with. Throughout this section, the parameters used are those employed in the "benchmark" scan with maximal stop mixing (see Section 5.3.1).

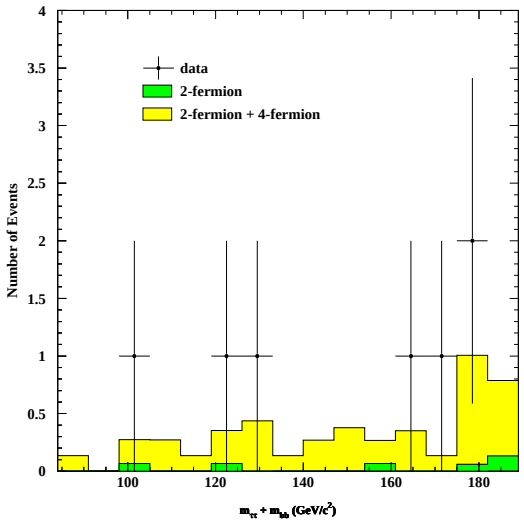

Figure 4.19: Sum of the reconstructed masses of the $\tau^+\tau^-$ and $b\bar{b}$ pair in selected h^0A^0 background events.

decays. In the SM H^0Z^0 likelihood $\mathcal{L}_{q\bar{q}\tau^+\tau^-}$ described in Section 4.1.5, no b-tagging is used and therefore it can efficiently select $h^0Z^0 \to gg\tau^+\tau^-$ and $h^0Z^0 \to q\bar{q}\tau^+\tau^-$ events, where q is a quark of arbitrary flavor. By requiring $\mathcal{L}_{q\bar{q}\tau^+\tau^-} > 0.8$ (chosen such that the accepted level of signal and background is similar to the SM search) and explicitly requiring the event to satisfy the $h^0Z^0 \to q\bar{q}\tau^+\tau^-$ kinematic hypothesis ($P_{3C_1}(\chi^2) > 10^{-5}$), an efficiency of $(28.7 \pm 1.5(\text{stat.}) \pm 2.7(\text{syst.}))\%$ for a hadronically-decaying Higgs of mass 80 GeV/c^2 is retained. From Figure 4.21 one can see that the efficiencies for exclusive samples of $h^0 \to b\bar{b}$ and $h^0 \to c\bar{c}$ are quite similar, while the efficiencies for gluonic Higgs decays are only about 6% (relative) less.[5] In the data, two events are selected (to be compared with $3.4 \pm 0.5(\text{stat.}) \pm 0.7(\text{syst.})$ expected from SM background), with masses 79.5 GeV/c^2 and 89.2 GeV/c^2. They correspond to the first and third SM candidates in Table 4.5, where the latter (an obvious Z^0Z^0 event) is interpreted this time as $h^0Z^0 \to q\bar{q}\tau^+\tau^-$ instead of $H^0Z^0 \to \tau^+\tau^-q\bar{q}$. Systematic uncertainties were again evaluated as in Section 4.1.7; however, b-tagging uncertainties

[5]Presumably this is due to the different kinematic properties of gluon jets relative to quark jets. The selection, in particular the kinematic fitting, tends to pick out events that have quark-like jets, which can be seen in the similarity of the final mass resolutions (Figure 4.21b).

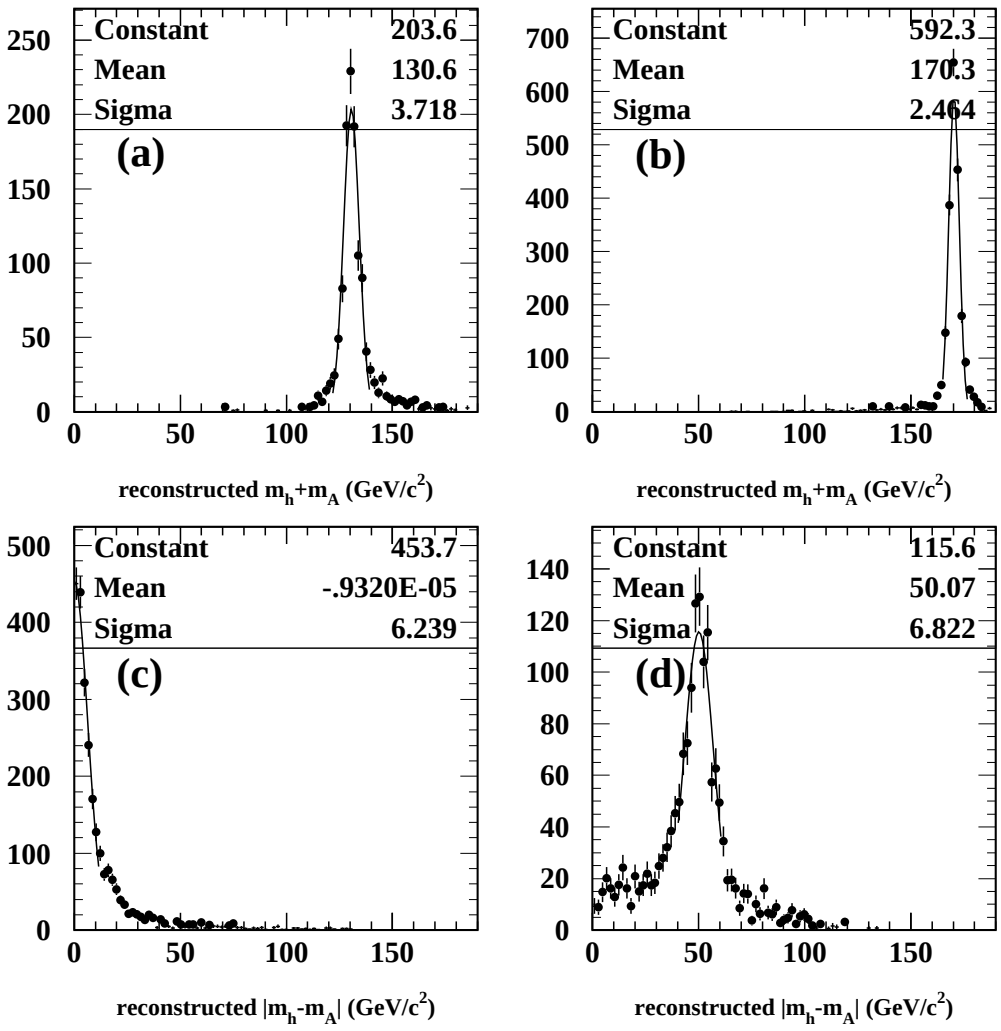

Figure 4.20: Reconstructed Higgs mass sums for selected signal events with (a) $m_{\mathrm{h}} + m_{\mathrm{A}} = 130$ GeV/c^2 and (b) $m_{\mathrm{h}} + m_{\mathrm{A}} = 170$ GeV/c^2, and reconstructed absolute mass differences for (c) $|m_{\mathrm{h}} - m_{\mathrm{A}}| = 0$ GeV/c^2 and (d) $|m_{\mathrm{h}} - m_{\mathrm{A}}| = 50$ GeV/c^2. The Gaussian fits to the cores of the distributions are shown to give an idea of the resolution and the normalization is arbitrary.

were dropped and the aforementioned 6% gluon efficiency difference was incorporated as a "flavor-dependence" uncertainty on the efficiency.

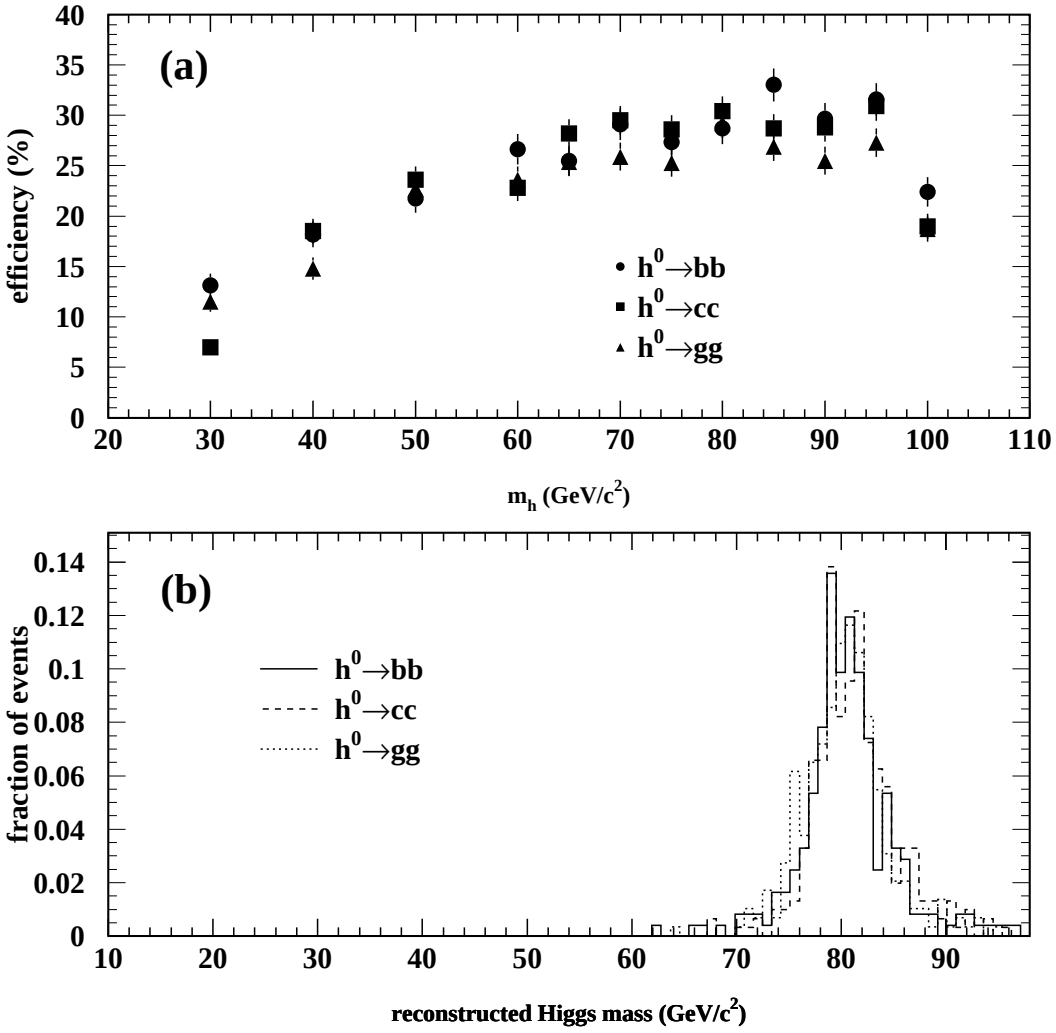

Figure 4.21: The (a) efficiencies and (b) mass resolutions for Higgs decays to bottom, charm, and gluons. (b) is for a Higgs of mass 80 GeV/c^2.

CHAPTER 5
RESULTS

Maximum sensitivity to detection of the Higgs is achieved by combining the results of all search topologies from all relevant center-of-mass energies. From OPAL's previously published lower bound on the SM Higgs mass (88.3 GeV/c^2) [48] it is seen that only the data sets from $\sqrt{s} = 183$ [48] and 189 GeV [49] are relevant to this SM Higgs search. For searches within the context of more complex Higgs theories (such as the MSSM), light Higgs bosons are not absolutely excluded and therefore the data taken at lower $\sqrt{s}$ [50, 51, 52] (especially the large amount of data taken at $\sqrt{s} \approx m_{\mathrm{Z}}$ at LEP1) extend the reach of the searches.

Section 5.1 describes the method used to combine the search channels and extract results. The results of the searches are then presented for the SM Higgs (Section 5.2), for the MSSM (Section 5.3), and for more general models (Section 5.4).

5.1 Limit Calculation Method

To search for a signal in the data, the simplest thing one could imagine doing is to look for an excess in the number of selected events over the number expected from background processes. However, more information is available to discriminate Higgs production from background. For each event one can reconstruct a Higgs mass from the four-vectors of its decay products (see Figure 4.14 for example). Therefore any excess due to Higgs production should show up as a peak in the reconstructed mass spectrum of the selected events, and events far from the peak can be considered less signal-like. In addition, signal events should distribute themselves among the various final states in a definite manner (according to the H^0 and Z^0 branching ratios), whereas background events might have a completely different distribution.

We take advantage of these features of the signal via "fractional event-counting," a technique described in detail in [53]. For a given Higgs mass hypothesis (hereafter

referred to as m_{test}) one can construct an expected mass distribution $D(m - m_{\text{test}})$ with a maximum $D_{\max}$ at $m = m_{\text{test}}$, similar to the distributions shown in Figure 4.15. Any event can then be given a weight w_1 varying between 0 and 1 according to its reconstructed mass m:

$$w_1 = \frac{D(m - m_{\text{test}})}{D_{\max}} \tag{5.1}$$

For one event, the event weight probability distribution is

$$P_1(w_1) = \sum w_1 D_{\max}^2 \left| \frac{dm}{dD} \right| \tag{5.2}$$

where the sum runs over all ambiguities in the inversion of $D(m - m_{\text{test}})$.

For a fixed number of events n, the quantity of interest is the weight sum $w_n = \sum_{i=1}^{n} w_i$ (note that $0 < w_n < n$ by definition). Its distribution $P_n(w_n)$ must be determined through iterative folding:

$$P_n(w_n) = \int_{\max[0, w_n - (n-1)]}^{\min(1, w_n)} P_{n-1}(w_n - w_1)\, P_1(w_1)\, dw_1 \tag{5.3}$$

To get the weight sum distribution for an arbitrary number of events, $P_n(w_n)$ must be convoluted with the Poisson distribution $\mathcal{P}(\mu; n)$, where μ is the mean number of events expected:

$$P(\mu; w) = \sum_{n=0}^{\infty} \mathcal{P}(\mu; n) P_n(w) \tag{5.4}$$

Note that $P_n(w) = 0$ for $n < w$.

If the weight sum w is to include events from different search channels, it is clear that channels with more expected signal, less expected background, and/or better mass resolution should somehow be given more weight in the sum than less sensitive channels. To do this, the weight for an event in a given channel k is multiplied by

$$c_k = \frac{(S_k/S_1)(D_{k,\max}/D_{1,\max})}{B_k/B_1} \tag{5.5}$$

where S_k and B_k are the amount of signal and background, differential in mass, expected in channel k (this will depend on the channel's luminosity, efficiency, and

for S_k, signal branching ratio into channel k). $D_{k,\max}$ is the height of the peak of the signal distribution and is inversely proportional to the channel's mass resolution. The $k = 1$ channel used in Equation 5.5 refers to the one with the largest signal-to-background ratio, such that $c_1 = 1$.

Given a background shape such as Figure 4.14, we can follow the same procedure to assign an event a weight v indicating its compatibility with background and continue with the formalism to arrive at a background weight sum distribution $Q(\mu_b; v)$. We then define the quantity CL_b to be the probability under the background-only hypothesis to obtain a weight sum w less than or equal to the one observed:

$$CL_b = \int_0^{w_{\text{obs}}} Q(\mu_b; v)\, dv \tag{5.6}$$

The alternative hypothesis is that signal accompanies the background. The probability to observe a weight sum w' when the expected signal and background rates are μ_s and μ_b is

$$P_{s+b}(w') = \int_0^{w'} P(\mu_s; w' - v)\, Q(\mu_b; v)\, dv \tag{5.7}$$

Therefore the probability to observe a weight sum less than or equal to the one observed is

$$CL_{s+b} = \int_0^{w_{\text{obs}}} P_{s+b}(w')\, dw' \tag{5.8}$$

One could now imagine excluding the signal hypothesis at a confidence level CL if $1 - CL_{s+b} \leq \text{CL}$. However, if the number of candidates observed is fewer than what is expected even in the background-only hypothesis, this leads to artificially strong signal exclusions. To retain conservative limits in these cases, the modified frequentist approach prescribed in [46] is adopted, where the quantity CL_s is defined as

$$CL_s = CL_{s+b}/CL_b \tag{5.9}$$

and a signal is excluded at a confidence level CL if $1 - CL_s \leq \text{CL}$. Taking CL=0.95 for concreteness, one can also say that the 95% CL upper limit on the signal production rate (N_{95}) is the μ_s that results in $1 - CL_s = 0.95$.

Channel	$\sqrt{s} = 183$ GeV		$\sqrt{s} = 189$ GeV		Total	
	Expected	Obs.	Expected	Obs.	Expected	Obs.
4-jet	5.0 ± 0.2	7	19.9 ± 0.8	24	24.9 ± 0.8	31
missing-E	1.6 ± 0.1	0	6.9 ± 0.5	10	8.5 ± 0.5	10
lepton	0.6 ± 0.1	1	4.7 ± 0.2	4	5.3 ± 0.2	5
tau	1.3 ± 0.1	1	4.0 ± 0.5	3	5.3 ± 0.5	4
All	8.5 ± 0.3	9	35.5 ± 1.1	41	44.0 ± 1.1	50

Table 5.1: Total number of events expected and observed for the four SM search channels. The errors are statistical only.

Systematic uncertainties on the background expectation are taken into account by conservatively reducing the background by its systematic error before it is statistically subtracted in Equation 5.7. Systematic uncertainties on the signal rate are incorporated using the method of [54] where quantities which depend on the signal are averaged over the systematic uncertainties on the signal.

5.2 SM Higgs Results

The number of events expected from SM background processes and the number of events actually observed in the data are shown in Table 5.1 for the four SM search channels (cf. Section 1.3.3). The distribution of reconstructed Higgs masses from the observed and expected events is shown in Figure 5.1. The peak of the expected background at $m = 91$ GeV/c^2 is due to irreducible $\mathrm{Z^0Z^0}$ production. As it turns out, the small excess of events seen in the last column of Table 5.1 is mainly concentrated around this mass, suggesting an upward statistical fluctuation of the $\mathrm{Z^0Z^0} \to \mathrm{b\bar{b}f\bar{f}}$ production rate. For comparison, a hypothetical signal of $m_{\mathrm{H}} = 91$ GeV/c^2 is shown added to the expected background in Figure 5.1. It can be seen that this signal would require an excess significantly larger than the one observed.

The lack of a significant excess in the data can be turned around to quote a 95% confidence level upper limit on the SM Higgs production cross section σ_{HZ}, or equivalently, since σ_{HZ} is a function of the Higgs mass, a 95% CL lower limit on m_{H}. Figure 5.2a shows CL_s, the confidence level on the signal hypothesis computed as

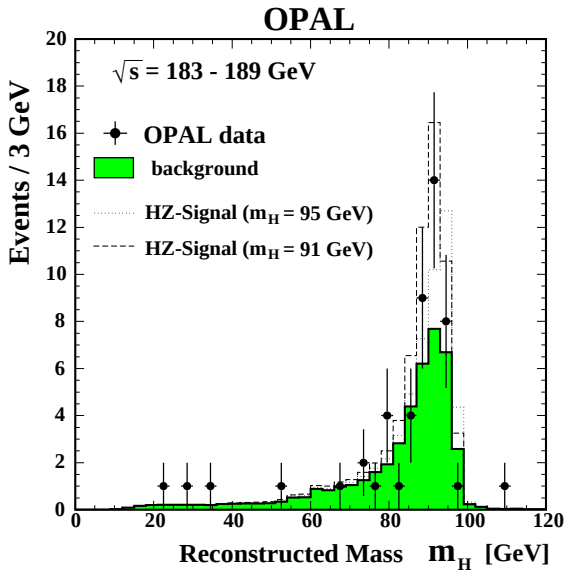

Figure 5.1: Distribution of reconstructed Higgs masses in all four SM search channels. The expected signal is shown added to the background.

described in Section 5.1, as a function of m_{H}. The solid line is the CL_s observed from the data, while the dashed line is the average CL_s determined from a large number of simulated "background-only" experiments, with simulated candidates distributed according to the expected background shapes. The 95% CL Higgs mass lower limit is set where these curves intersect the 5% line. The observed limit is $m_{\mathrm{H}} > 91.0$ GeV/c^2, whereas the average expected limit is 94.9 GeV/c^2. The latter result gives an indication of OPAL's sensitivity to the Higgs, independent of the effects of statistical fluctuations in the data.

Figure 5.2b shows more clearly how the small excess of events around $m = 91$ GeV/c^2 brings the observed limit down from the expected one. The solid curve shows the minimum number of signal events one can exclude at 95% CL via the fractional event-counting method described in Section 5.1. The excess gives rise to a bump in the curve at $m_{\mathrm{H}} = 91$ GeV/c^2, and therefore it intersects the steeply-falling signal rate curve "earlier" than expected. From the distribution of expected limits used to compute the average, one can ask what the probability is to observe a limit less than or equal to 91.0 GeV/c^2 when the average expected is 94.9 GeV/c^2. This probability is 4%.

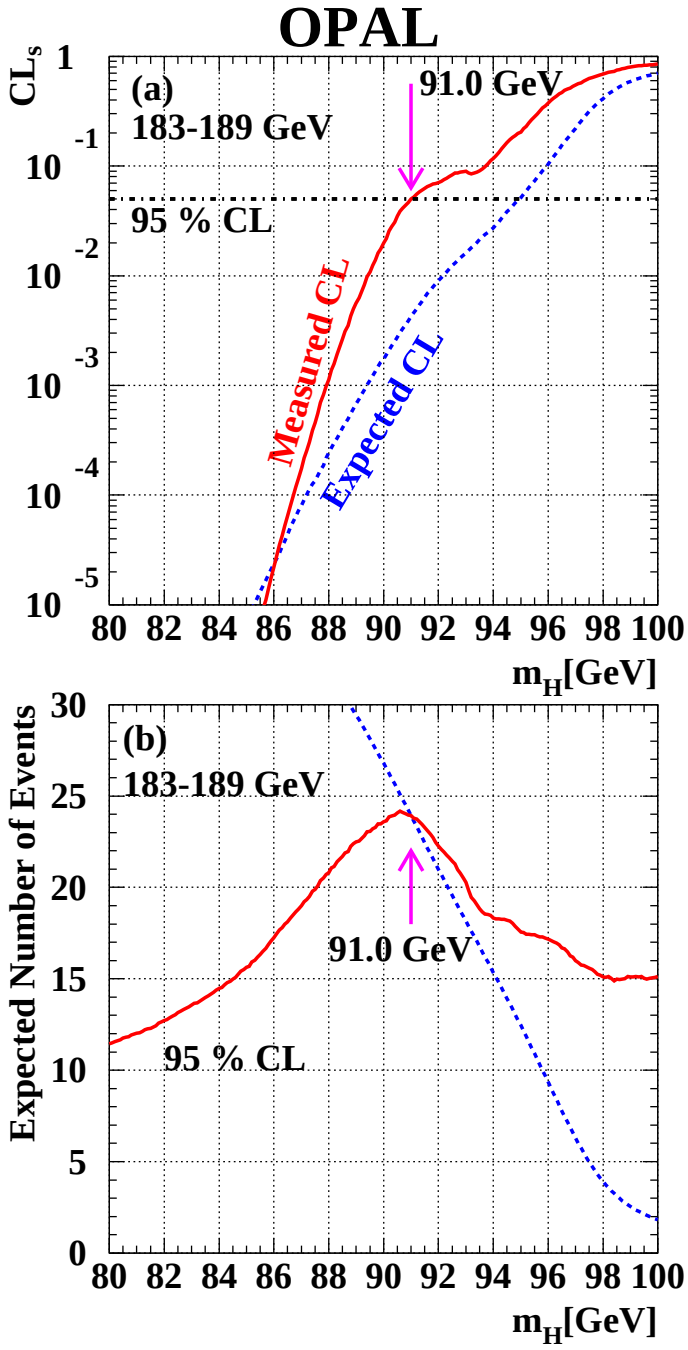

Figure 5.2: The confidence level on the signal hypothesis (a) and the expected signal rate and N_{95} curves (b) as a function of Higgs mass. In (a) the solid curve is the observed CL_s while the dashed curve is the average expected CL_s. In (b) the solid curve is the minimum number of events excludable at 95% CL (N_{95}) while the dashed curve is the expected number of signal events.

Channel	$\sqrt{s} = 183$ GeV		$\sqrt{s} = 189$ GeV		Total	
	Expected	Obs.	Expected	Obs.	Expected	Obs.
4-b	2.9 ± 0.2	4	8.0 ± 0.5	8	10.9 ± 0.5	12
tau	1.5 ± 0.1	3	4.9 ± 0.6	7	6.4 ± 0.6	10
6-b	2.3 ± 0.2	2	8.7 ± 1.0	5	11.0 ± 1.0	7
All	6.7 ± 0.3	9	21.6 ± 1.3	20	28.3 ± 1.3	29

Table 5.2: Total number of events expected and observed for the h^0A^0 search channels. The errors are statistical only.

5.3 MSSM Results

The four SM search channels are reinterpreted as searches for the MSSM Higgs-strahlung process $e^+e^- \to h^0Z^0$, where $h^0 \to b\bar{b}$ or $h^0 \to A^0A^0$. To cover the pair-production process $e^+e^- \to h^0A^0$, three dedicated searches for $h^0A^0 \to b\bar{b}b\bar{b}$, $h^0A^0 \to b\bar{b}\tau^+\tau^-$ (described in detail in Section 4.2.2), and $h^0A^0 \to A^0A^0A^0 \to b\bar{b}b\bar{b}b\bar{b}$ are also used.

The number of events expected and observed in these channels is shown in Table 5.2. In the 4-b channel, there are three ways to pair the four jets to reconstruct the h^0 and A^0 masses. In addition, there is no way to tell which mass is the h^0 and which is the A^0, so each event is interpreted six times in the event counting. The jet-pairing ambiguity is absent in the tau channel, but the h^0-A^0 ambiguity remains, so each tau channel event is counted twice. No mass reconstruction is done in the 6-b channel.

For presentation of mass spectra, the distributions of the sums of the reconstructed m_{h} and m_{A} are shown in Figure 5.3 for the 4-b and tau channels. Again, no significant excess is observed anywhere and upper limits on signal production can be extracted. However, interpreting these limits within the MSSM requires the specification of the parameters of the MSSM that determine the Higgs masses, cross sections, and branching ratios. The strategy adopted, then, is to "scan" over possible parameter sets, interpreting each point in parameter space as an independent model, and determining if the predicted signal production rate is excludable from the data. Two different scans are performed, the "benchmark" scan (Section 5.3.1) and the "general"

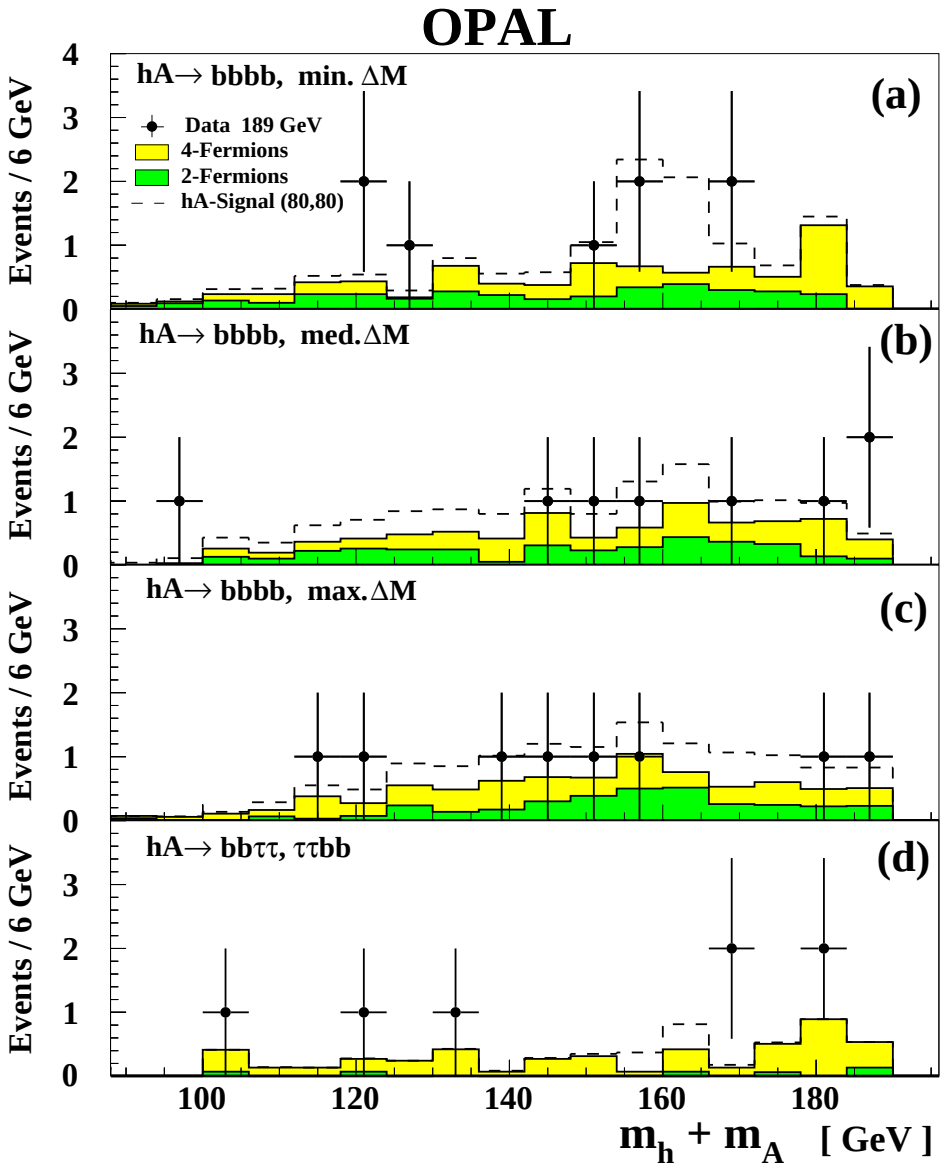

Figure 5.3: Distributions of the sums of the reconstructed h^0 and A^0 masses for the 4-b and tau channels. (a) is for the 4-b channel jet pairing that minimizes the difference in the reconstructed masses, (c) is for the pairing that maximizes the difference, and (b) is the third pairing. The tau channel (d) is free from this ambiguity. The signal is for $m_{\mathrm{h}} = m_{\mathrm{A}} = 80$ GeV/c^2, with benchmark scan parameters and maximal stop-mixing (see Section 5.3.1), and is shown added to the background.

scan (Section 5.3.2).

5.3.1 Benchmark Scan

In order to determine limits in a reasonably-sized model space, the supergravity-inspired CMSSM discussed in Section 1.5.2 is used as a framework to calculate the parameters contributing to the sizeable radiative corrections to the Higgs sector. Recall that this required the specification of five parameters:

- m_0, the common GUT-scale sfermion mass.
- M_2, the SU(2) gaugino mass at the EW scale.[1] The U(1) and SU(3) gaugino masses are determined from the ratio of coupling constants, i.e. $M_1 : M_2 : M_3 = \alpha_1 : \alpha_2 : \alpha_3$.
- A, the Higgs-sfermion trilinear coupling.
- μ, the supersymmetric Higgs mass parameter
- $\tan\beta$, the ratio of the vacuum expectation values of the two Higgs doublet fields.

In addition, we also specify

- m_{A}, the running mass of the neutral CP-odd Higgs boson. The five parameters of the CMSSM are sufficient to determine all the parameters that enter into the Higgs radiative corrections, but m_{A} is a tree-level free parameter.
- m_{t}, the top quark mass. The current experimental determination is $m_{\mathrm{t}} = 174.3 \pm 5.1$ GeV/c^2 [55]. Variation of this parameter within $\pm 1\sigma$ has significant effects on the MSSM Higgs sector (for example, m_{h} depends on the fourth power of m_{t}, as seen in Equation 1.52), and therefore it is left as a "quasi-free" parameter.

[1] This parameter is used in favor of the common GUT-scale gaugino mass $m_{1/2}$ mentioned in Section 1.5.2.

In the benchmark scan, proposed in [20], we fix $m_0 = 1$ TeV/c^2, $M_2 = 1.63$ TeV/c^2, $\mu = -100$ GeV/c^2, and $m_{\rm t} = 175$ GeV/c^2. Two possible scenarios are considered for the mixing of left- and right-handed stops to form the physical mass eigenstates. For the first, A is set to 0, corresponding to no mixing. For the second, $A = \sqrt{6}m_Q$, corresponding to maximal mixing (m_Q is the "left-up" squark mass at the EW scale, computed from m_0). $\tan\beta$ is varied from 0.7 to 50[2]; $m_{\rm A}$ is varied from 5 to 160 GeV/c^2, and then in 5 GeV/c^2 bands around 250, 400, 1000, and 2000 GeV/c^2.

These parameters are input to the HZHA [34] program, which calculates the Higgs masses and couplings in the renormalization-group-improved one-loop effective potential approximation [13]. This program is supplemented by SUSYGEN [56], which calculates the EW-scale sfermion masses from the same inputs. The final Higgs production cross sections and branching ratios output from HZHA include next-to-leading-order EW and next-to-next-to-leading-order QCD corrections.

The results of the benchmark scan are shown in Figure 5.4 in three projections, the ($m_{\rm h}$, $m_{\rm A}$) plane, the ($m_{\rm h}$, $\tan\beta$) plane, and the ($m_{\rm A}$, $\tan\beta$) plane. Areas shown in blue (black) are excluded at 95% CL for both stop-mixing scenarios. In (a), (b), and (c) the yellow (grey) areas indicate regions of parameter space that are theoretically inaccessible in the benchmark scan. Unexcluded areas are shown in white.

Figure 5.4a shows the ($m_{\rm h}$, $m_{\rm A}$) plane restricted to $\tan\beta$ values larger than 1. One can read off the lower left-hand corner of the unexcluded region to get a 95% CL lower limit on $m_{\rm h}$ and $m_{\rm A}$ (see Table 5.3). In Figure 5.4b the $\tan\beta$ restriction is released and a small unexcluded region at $m_{\rm h} \approx 70$ GeV/c^2 and $m_{\rm A} < 10$ GeV/c^2 appears for $\tan\beta \approx 0.7$. Note that this area is in the $m_{\rm h} > 2m_{\rm A}$ regime and that the $\rm A^0 \to b\bar{b}$ branching ratio goes as $\tan\beta$. Therefore in this region the decay $\rm h^0 \to A^0A^0$ with subsequently suppressed $\rm A^0 \to b\bar{b}$ is expected. Since all OPAL $\rm h^0 \to A^0A^0$ searches require b-tagging, sensitivity is lacking in this regime. The smallness of the unexcluded area can be attributed to an ill-behaved, rapid variation of the $\rm A^0 \to b\bar{b}$ branching ratio near the edge of the theoretically allowed region.

[2]The theoretically favored range is $1 < \tan\beta < m_{\rm t}/m_{\rm b}$, but it is extended here for robustness.

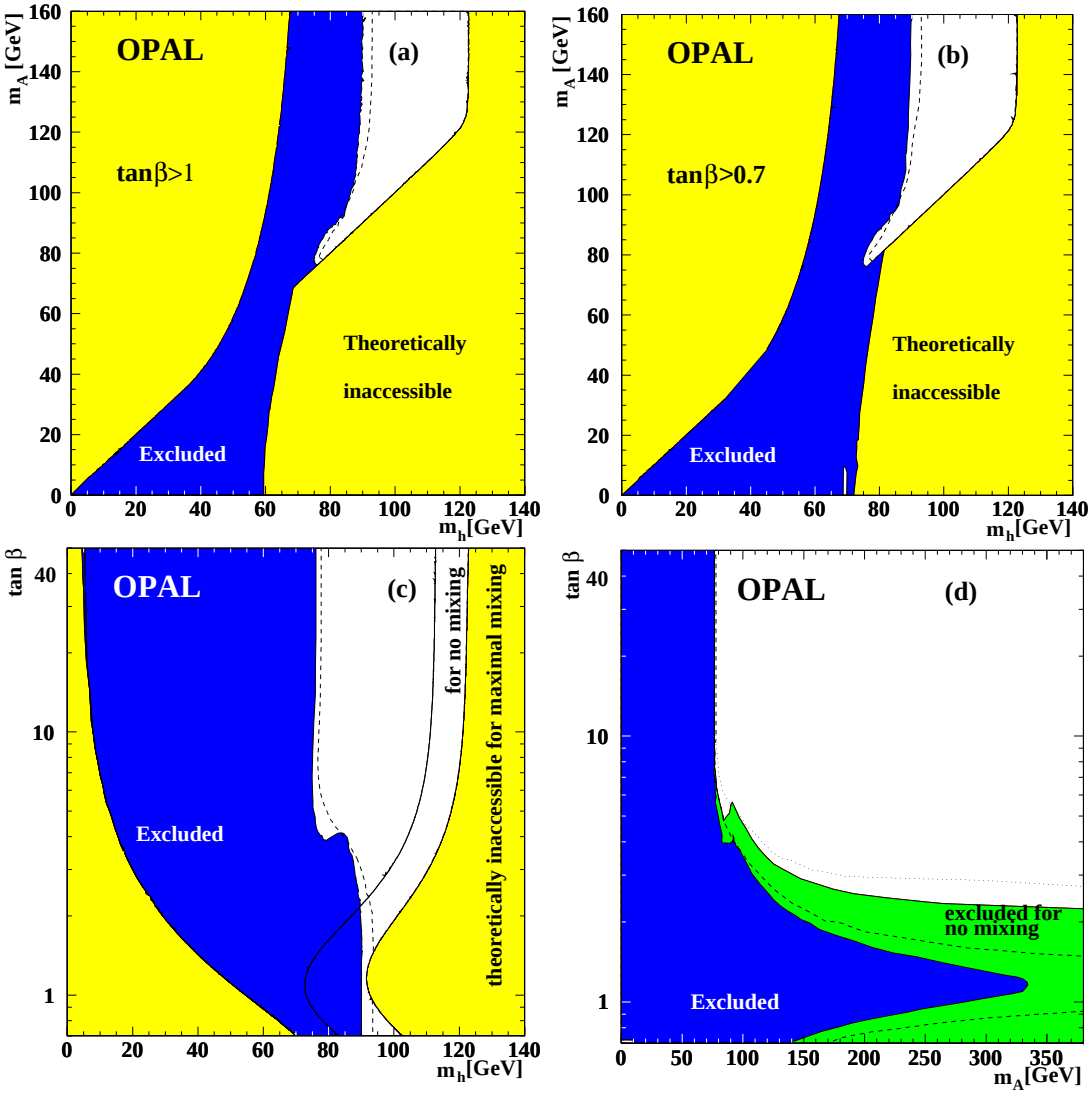

Figure 5.4: Results of the benchmark scan in (a) the (m_{h}, m_{A}) plane with $\tan\beta > 1$, (b) the (m_{h}, m_{A}) plane with $\tan\beta > 0.7$, (c) the (m_{h}, $\tan\beta$) plane, and (d) the (m_{h}, m_{A}) plane. The white areas are unexcluded. In (a), (b), and (c) the blue (black) areas are excluded at 95% CL and the yellow (grey) areas are theoretically inaccessible. In (d) the blue (black) area is excluded for maximal stop mixing; the green (grey) area is additionally excluded for no stop mixing. The dotted lines represent the expected exclusions.

Figure 5.4c shows the projection in the (m_{h}, $\tan\beta$) plane. The experimentally excluded region intersects the theoretically inaccessible region for the case of no stop-mixing. This allows an exclusion of a range of $\tan\beta$ around 1 for this scenario. For maximal mixing, the theoretically allowed region opens somewhat and this $\tan\beta$ range is no longer excluded. It should be noted that this $\tan\beta$ region is the SM-like, Higgsstrahlung-dominated regime. A maximal-mixing $\tan\beta$ exclusion here is actually expected from the simulated background-only experiments (as indicated by the dotted line), but the small 91 GeV/c^2 excess in the SM searches weakens the excluded area. It should also be noted that the quoted $\tan\beta$ exclusion (Table 5.3) is valid for $m_{\mathrm{t}} \leq 175$ GeV/c^2, as shifting m_{t} by its 1σ experimental uncertainty increases the theoretical upper bound on m_{h} (and hence the allowed (m_{h}, $\tan\beta$) space) by about 5 GeV/c^2.

Figure 5.4d shows the projection in the (m_{A}, $\tan\beta$) plane. These are the two scan variables and hence there are no theoretically inaccessible regions in this projection; instead the green (grey) area corresponds to the region excluded assuming no stop-mixing.

5.3.2 General Scan

In this scan all the parameters listed in Section 5.3.1 are varied within reasonable ranges. In particular,

1. $0 < m_0 < 1$ TeV/c^2
2. $0 < M_2 < 2$ TeV/c^2
3. $-2.5m_0 < A < 2.5m_0$
4. $-1 < \mu < 1$ TeV/c^2
5. $m_{\mathrm{t}} = 165$, 175, and 185 GeV/c^2
6. $\tan\beta$ and m_{A} varied as before

As one would expect, the allowed parameter space opens up considerably in this scan. For example, some parameter sets allow the heavier CP-even Higgs H^0 to be light enough to be produced via $e^+e^- \rightarrow H^0Z^0$. The SM searches are assumed to be sensitive to this process.

Some parameter sets yield CMSSM scenarios that can be excluded by current independent experimental constraints. These sets are those that yield stop or lightest neutralino masses that are excluded by direct OPAL searches [57, 58], and those that predict h^0 and A^0 masses small enough to generate an increase in the Z^0 width via $Z^0 \rightarrow h^0Z^*$ or $Z^0 \rightarrow h^0A^0$ that is inconsistent with the 95% CL upper limit on excess Z^0 width of 7.1 MeV/c^2 [51].

In addition, there are approximate theoretical constraints to apply to the CMSSM parameters. For large A and μ, it is possible for the stop fields to acquire a vacuum expectation value and give rise to a CMSSM potential with a global minimum in which charge and color are not conserved, which is of course incompatible with the present state of the universe. To generally avoid a charge- and color-breaking (CCB) minimum, the restriction

$$A^2 + 3\mu^2 < x(m^2_{\tilde{t}_L} + m^2_{\tilde{t}_R}) \tag{5.10}$$

should be applied, with $x \approx 3$ [59]. However, a calculation allowing for the universe to exist in a non-CCB local minimum, with a tunneling rate to a CCB global minimum small enough that the non-CCB vacuum has a long lifetime (compared to the age of the universe), relaxes this restriction to $x \approx 7.5$ [60].

Figure 5.5 shows the results of the general scan in the same projections as Figure 5.4. Again, the black areas are excluded, the grey areas theoretically inaccessible, and the white areas unexcluded. The grey hatched areas are unexcluded in general, but give rise to CCB minima in the CMSSM Lagrangian and are excluded when Inequality 5.10 is applied with $x = 7.5$. From Figure 5.5a absolute 95% CL lower mass limits for h^0 and A^0 can be derived for $\tan\beta > 1$ and are listed in Table 5.3.

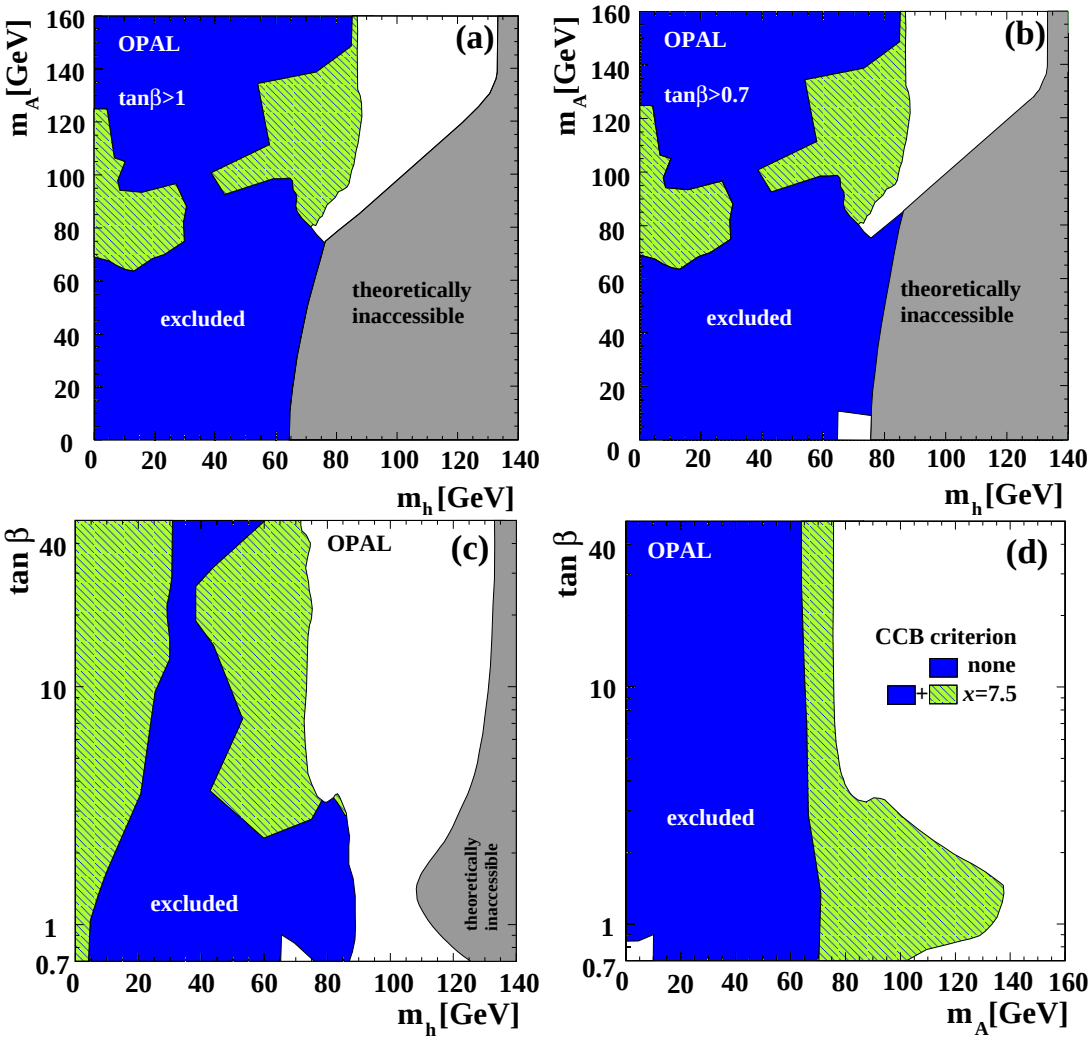

Figure 5.5: Results of the general scan in (a) the (m_{h}, m_{A}) plane with $\tan\beta > 1$, (b) the (m_{h}, m_{A}) plane with $\tan\beta > 0.7$, (c) the (m_{h}, $\tan\beta$) plane, and (d) the (m_{h}, m_{A}) plane. The blue (black) areas are excluded at 95% CL, the grey areas are theoretically inaccessible, and the white areas are unexcluded. The green (grey hatched) areas are additionally excluded with the application of a CCB criterion.

Scan	95% CL lower m_{h} limit, $\tan\beta > 1$ (GeV/c^2)		95% CL lower m_{A} limit, $\tan\beta > 1$ (GeV/c^2)		95% CL $\tan\beta$ exclusion (no $\tilde{t}$ mixing)
	Exp.	Obs.	Exp.	Obs.	Observed
benchmark	76.4	74.8	78.2	76.5	$0.72 < \tan\beta < 2.19$
general	n/a	72.2	n/a	76.0	none

Table 5.3: Summary of MSSM results. Expected limits from the general scan are unavailable due to CPU time limitations.

5.4 More General Interpretations

The interpretations of the analyses can be extended beyond the SM and CMSSM to search for other Higgs-like particles. In particular, we recast the results as upper limits on the production cross sections of semi-generic neutral scalar particles outside the context of any specific model (Section 5.4.1) and as exclusions in the parameter space of general Type II Two Higgs Doublet Models (Section 5.4.2). All OPAL data taken up to $\sqrt{s} = 189$ GeV [49, 48, 50, 51, 52] contribute here, since the mass reach needs to be as broad as possible.

5.4.1 Model-Independent Results

The first process considered is $\mathrm{e^+e^-} \to \mathrm{S^0Z^0}$, where $\mathrm{S^0}$ is any neutral scalar particle. The production cross section σ_{SZ} is parameterized with a scale factor s^2 relating it to the SM Higgs production cross section $\sigma_{\mathrm{HZ}}^{\mathrm{SM}}$:

$$\sigma_{\mathrm{SZ}} = s^2 \sigma_{\mathrm{HZ}}^{\mathrm{SM}} \tag{5.11}$$

Assuming the $\mathrm{S^0}$ has couplings identical to that of the SM Higgs boson, we can place a 95% CL upper limit on s^2 via

$$s^2_{95} = \frac{N^{\mathrm{SZ}}_{95}}{\sum(\epsilon \mathcal{L} \sigma^{\mathrm{SM}}_{\mathrm{HZ}})} \tag{5.12}$$

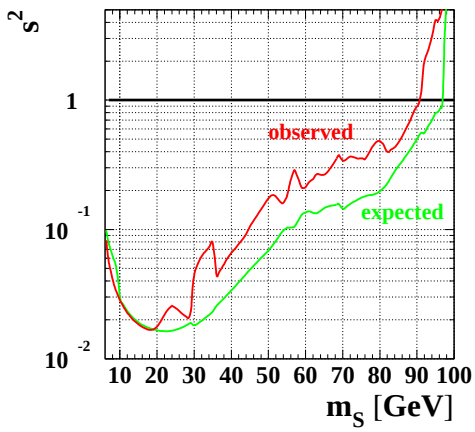

Figure 5.6: The 95% CL upper limit on s^2 (cf. Equation 5.11) as a function of m_{S^0}, assuming SM Higgs branching ratios for the S^0. The red (black) curve is the observed upper limit, and the green (grey) curve the average expected.

where the sum runs over the different center-of-mass energies, ϵ is the overall signal efficiency taken from the SM H^0Z^0 searches, and $\mathcal{L}$ is the integrated luminosity. N_{95}^{SZ} is the 95% CL upper limit on the number of S^0Z^0 signal events, calculated according to Section 5.1. This upper bound on s^2 is shown as a function of m_{S^0} in Figure 5.6. Note that this curve crosses the $s^2 = 1$ line at the SM Higgs 95% CL mass limit, as it should.

The assumption of SM Higgs couplings for the S^0 somewhat belies the "model-independence" of the results shown in Figure 5.6; the limit is only valid for a S^0 that decays predominantly to $b\bar{b}$ pairs. However, with an analysis like the flavor-independent one described in Section 4.3, a limit can be derived that is valid for a S^0 that decays to any quark or gluon pair. To this end, similar flavor-independent analyses were developed for the other three SM H^0Z^0 search channels [61]. The reconstructed mass distribution of their selected events is shown in Figure 5.7. No excess is observed, indicating that a non-standard Higgs did not "slip through the cracks" of the b-tag-dependent SM searches. The subsequent s^2 limit, assuming only 100% hadronic branching ratio for the S^0, is shown in Figure 5.8.

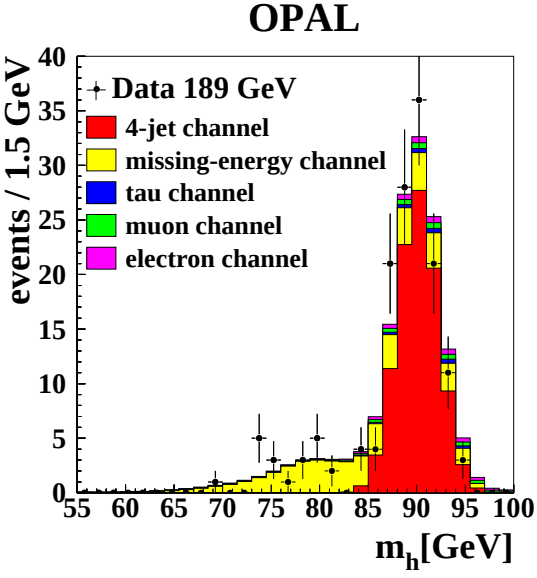

Figure 5.7: Mass spectrum of events selected by the flavor-independent H^0Z^0 searches. The flavor-independent four-jet channel is a mass-dependent analysis; shown here are the events selected for a hypothesized Higgs mass of 90 GeV/c^2.

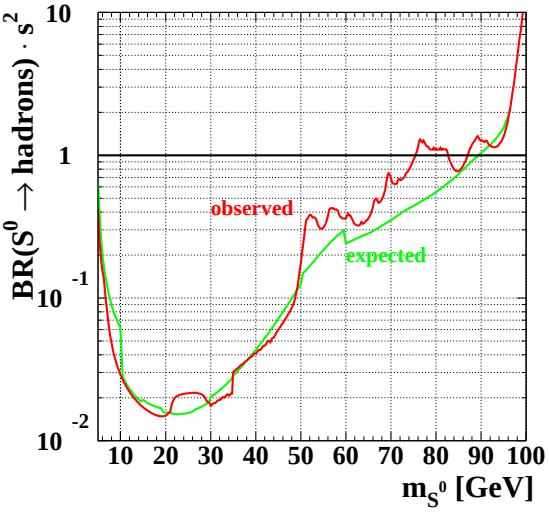

Figure 5.8: The 95% CL upper limit on s^2 (cf. Equation 5.11) as a function of m_{S^0}, assuming 100% hadronic branching ratio for the S^0. The red (black) curve is the observed upper limit, and the green (grey) curve the average expected.

Going further, the $h^0A^0 \to b\bar{b}\tau^+\tau^-$ analysis described in Section 4.2.2 can be applied to the generic process $e^+e^- \to S^0P^0 \to b\bar{b}\tau^+\tau^-$, where P^0 is any pseudoscalar particle. We again parameterize the production cross section σ_{SP} in terms of the SM H^0Z^0 cross section:

$$\sigma_{SP} = c^2\bar{\lambda}\sigma_{HZ}^{SM} \tag{5.13}$$

where $\bar{\lambda}$ is a kinematic factor akin to the one defined in Equation 1.40. The 95% CL upper limit on c^2 is then

$$c_{95}^2 = \frac{N_{95}^{SP}}{\sum(\epsilon\mathcal{L}\bar{\lambda}\sigma_{HZ}^{SM})} \tag{5.14}$$

where ϵ now refers to the efficiencies for the $h^0A^0 \to b\bar{b}\tau^+\tau^-$ searches. The decays of the S^0 and P^0 are not known *a priori*, so the upper limits are presented in the $(m_{\tau^+\tau^-}, m_{b\bar{b}})$ plane in Figure 5.9, assuming 100% branching ratio into the $b\bar{b}\tau^+\tau^-$ final state. Along the $m_{\tau^+\tau^-} = m_{b\bar{b}}$ diagonal, a 95% CL lower limit on m_{S^0} and m_{P^0} of 78 GeV/c^2 is obtained for $c^2 \geq 1$.

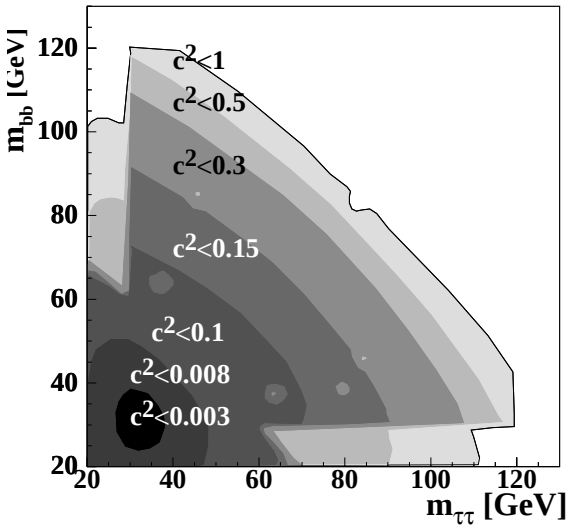

Figure 5.9: The 95% CL upper limits on c^2 (cf. Equation 5.13) as a function of $m_{\tau^+\tau^-}$ and $m_{b\bar{b}}$, assuming 100% branching ratio into the $b\bar{b}\tau^+\tau^-$ final state.

5.4.2 Type II Two Higgs Doublet Model Results

As discussed in Section 1.4, the cross sections and branching ratios of Higgs bosons in any Type II 2HDM are determined at tree level by the Higgs masses, $\tan\beta$, and α. In the most general case, these parameters are all free. Therefore an interpretation of the results in this context is done by scanning over m_{h}, m_{A}, $\tan\beta$, and α, similar to what is done in the MSSM (see Section 5.3). Calculations of the cross sections and branching ratios, assuming no other particles besides those of the SM, are performed using these parameters as inputs to the HZHA program. Results are then presented as excluded areas in the four-dimensional parameter space. The parameter space covered is:

- $1.0 \leq m_{\mathrm{h}} \leq 100$ GeV/c^2, in steps of 1 GeV/c^2
- $5.0 \leq m_{\mathrm{A}} \leq 2.0$ TeV/c^2, in steps of 1 GeV/c^2 up to 100 GeV/c^2, steps of 5 GeV/c^2 up to 500 GeV/c^2, and steps of 500 GeV/c^2 thereafter
- $0.4 \leq \tan\beta \leq 58.0$, in steps of $\beta = 1^\circ$
- $\alpha = 0, -\pi/8, -\pi/4, -3\pi/8$, and $-\pi/2$

As in Section 5.4.1, both low- and high-energy data samples are used, and the flavor-independent searches are used at points where they yield a better expected confidence level than the b-tagging searches (*e.g.*, for $\alpha = 0$ points, where $\mathrm{BR}(\mathrm{h}^0 \to \mathrm{b\bar{b}}) = 0$). In addition to the direct searches, the Z^0 width constraint (see Section 5.3.2) and the results from a search for any light (≤ 9.5 GeV/c^2) neutral scalar particle produced in association with a Z^0 [62] are used to provide exclusion for light Higgses.

Figure 5.10 shows the results of the scan in the (m_{h},m_{A}) projection for the five α values. The areas shown in green (dark grey) are excluded at 95% CL for all scanned values of $\tan\beta$. The excluded areas are extended when restricting $\tan\beta$ to $0.4 \leq \tan\beta \leq 1.0$ (yellow/light grey) and $1.0 \leq \tan\beta \leq 58.0$ (hatched). The expected excluded area for all $\tan\beta$ is shown by the dashed line. Listing some features of the different searches and data samples is helpful to understand some of the sharp edges in Figure 5.10.

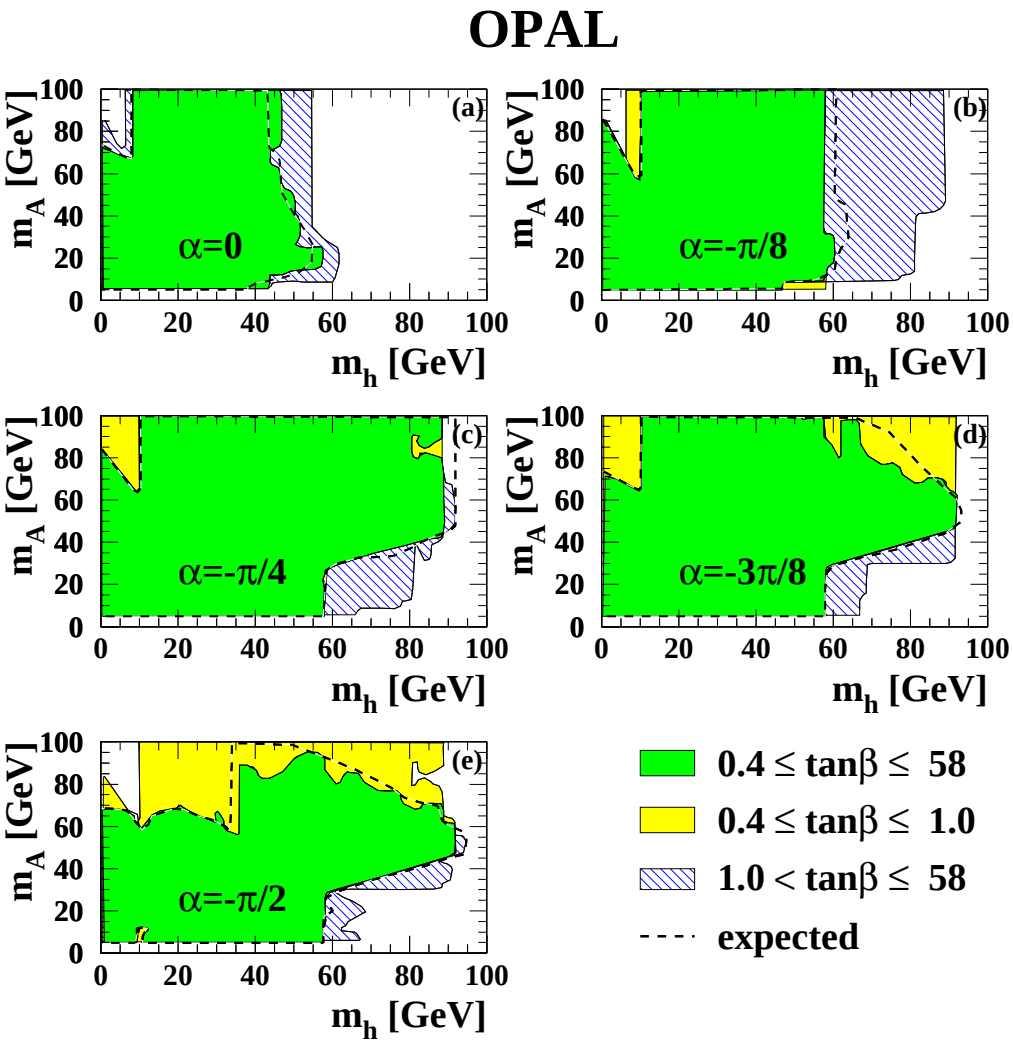

Figure 5.10: Excluded areas of the (m_{h}, m_{A}) plane for a general Type II 2HDM, for five different values of α. The green (dark grey) regions are excluded at 95% CL for $0.4 \leq \tan\beta \leq 58.0$. The yellow (light grey) areas are additionally excluded making the restriction $0.4 \leq \tan\beta \leq 1.0$, and the hatched areas are additionally excluded under the restriction $1.0 \leq \tan\beta \leq 58.0$.

1. The direct h^0Z^0 searches from $\sqrt{s} = m_Z$ are only sensitive for h^0 masses from about 10 to 57 GeV/c^2.

2. The h^0A^0 process at $\sqrt{s} = m_Z$ is kinematically limited to $m_h + m_A \leq m_Z$.

3. The high-energy h^0A^0 searches are only sensitive for h^0 and A^0 masses larger than about 35 GeV/c^2.

4. The $h^0 \to A^0A^0$ process is restricted by kinematics to the $m_h \geq 2m_A$ regime. The high-energy searches for this process all require b-tagging and are therefore only sensitive for large $\tan\beta$ (recall $\mathrm{BR}(A^0 \to b\bar{b}) \propto \tan\beta$).

The h^0 and A^0 masses excluded independently of α are shown in Figure 5.11. This is basically the "intersection" of the five plots of Figure 5.10.

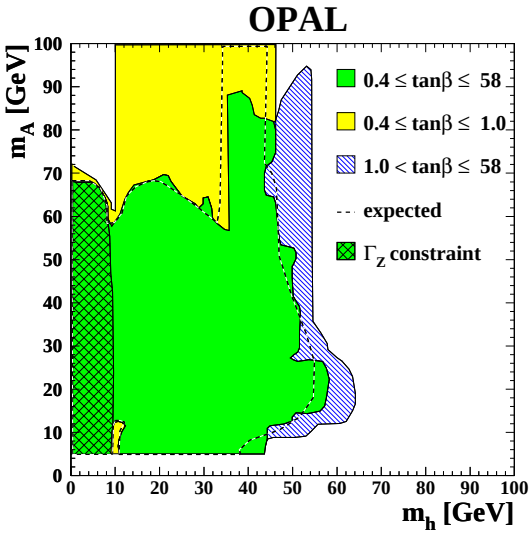

Figure 5.11: Excluded areas of the (m_h, m_A) plane for a general Type II 2HDM, independent of the value of α. The green (dark grey) regions are excluded at 95% CL for $0.4 \leq \tan\beta \leq 58.0$. The yellow (light grey) areas are additionally excluded making the restriction $0.4 \leq \tan\beta \leq 1.0$, and the hatched areas are additionally excluded under the restriction $1.0 \leq \tan\beta \leq 58.0$. The cross-hatched region is excluded using constraints from the Z^0 width only.

CHAPTER 6
CONCLUSIONS

As was seen in Chapter 5, no Higgs bosons were found in the 1998 OPAL data. The LEP2 program has continued since then with ever larger center-of-mass energies; for example, in 1999 OPAL collected almost 225 pb^{-1} at center-of-mass energies from 192 to 202 GeV. These additional data allow one to search for heavier Higgs bosons, and also to better understand the nature of the small excess of candidates at $m_{\mathrm{H}} \approx m_{\mathrm{Z}}$ seen in Figure 5.1. Distributions of reconstructed Higgs masses for the 1999 data are shown in Figure 6.1; the excess at m_{Z} clearly did not persist. This lends credence to the hypothesis that there was merely an upward statistical fluctuation of $\mathrm{Z}^0\mathrm{Z}^0$ production in 1998, and not hints of 91 GeV/c^2 Higgs production.

The strongest possible limits on Higgs boson production come from combining the results of the four LEP experiments, so as to effectively quadruple the luminosity of

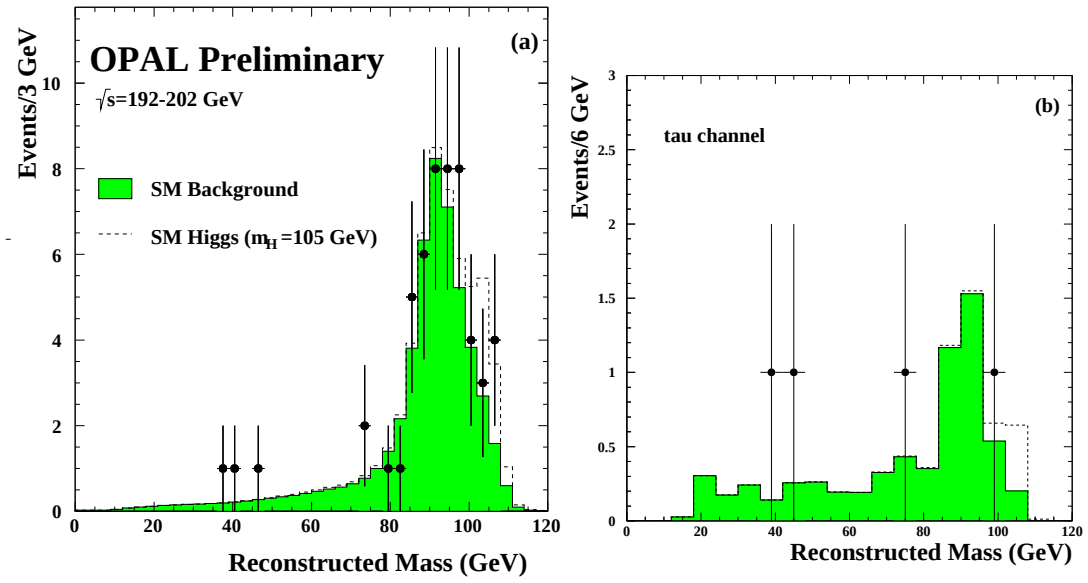

Figure 6.1: Distribution of reconstructed Higgs masses in (a) all four OPAL SM search channels and (b) the tau channel only, from data taken in 1999.

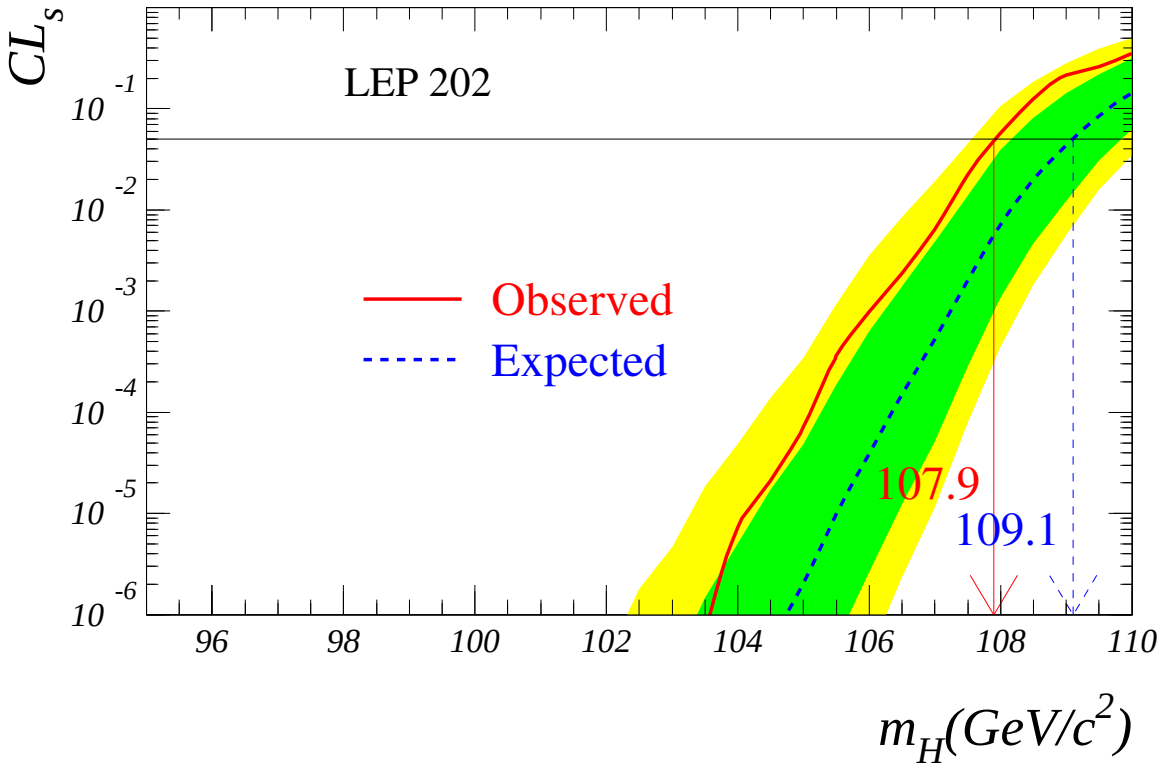

Figure 6.2: CL_s vs. SM Higgs mass. All four LEP experiments are combined, using all data taken up to the end of 1999. The red (solid) curve is the observed CL_s, the blue (dashed) is the median expected CL_s in the absence of signal. The bands represent the 1σ and 2σ probability contours for the expected CL_s.

any one experiment. This is in principle straightforward to do using the formalism of Section 5.1; each experiment is considered as a new independent set of search channels. Figure 6.2 shows the LEP-wide CL_s as a function of the SM Higgs mass including the data collected in 1999; the observed 95% CL lower limit is $m_{\mathrm{H}} > 107.9$ GeV/c^2. By the end of LEP2 in 2000, this limit is expected to improve by an additional 5–6 GeV/c^2.

The Higgs search will continue to have high priority at future collider programs, specifically at the TeVatron $p\bar{p}$ facility at Fermilab and CERN's LHC pp collider. An encouraging experimental result for these programs is the SM Higgs mass estimated from electroweak precision measurements. The Higgs mass enters, albeit only logarithmically, into loop corrections for a number of EW parameters, so that by performing a global fit to the 18 different parameters listed in Figure 1.1 one can

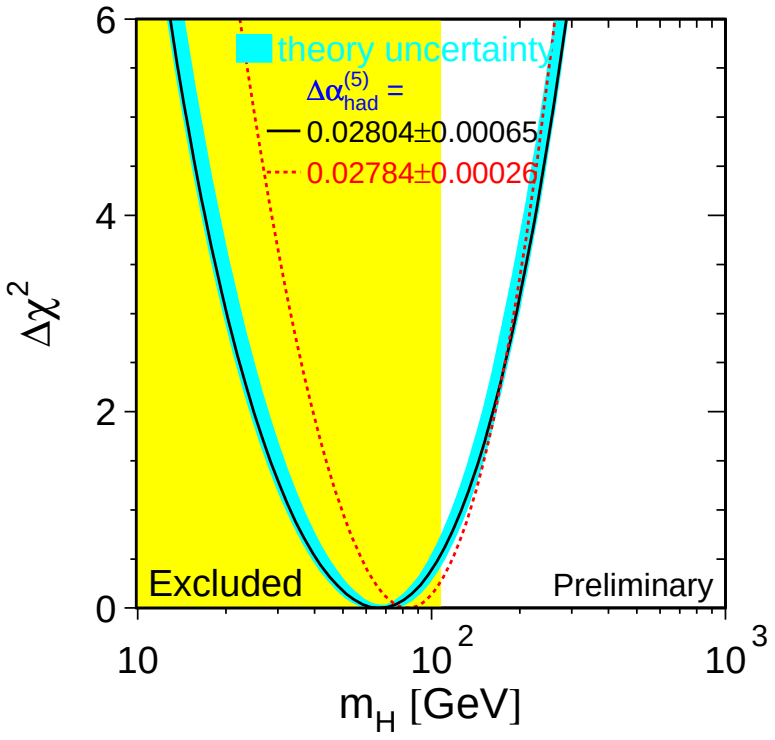

Figure 6.3: The $\Delta\chi^2 = \chi^2 - \chi^2_{\rm min}$ vs. SM Higgs mass curve for a global fit to precision EW measurements. The solid and dotted curves are obtained for two different determinations of the hadronic correction to the electromagnetic coupling constant. The shaded area is excluded by the direct LEP searches (cf. Figure 6.2).

determine the Higgs mass (with a large uncertainty) from the value that minimizes the χ^2 of the fit. This is shown in Figure 6.3; it is seen that the EW data prefer a Higgs mass of 67^{+60}_{-33} GeV/c^2, well below its theoretical upper bound (cf. Figure 1.7). The two EW parameters that are most sensitive to the Higgs mass are $m_{\rm t}$ and $m_{\rm W}$; Figure 6.4 shows the 68% CL contours for these measurements along with the predicted $m_{\rm W}$ vs. $m_{\rm t}$ curves for several different Higgs masses. Again one sees that relatively low values of Higgs masses are preferred, indicating that the Higgs may in fact be "just around the corner," and awaiting discovery at the TeVatron or LHC.

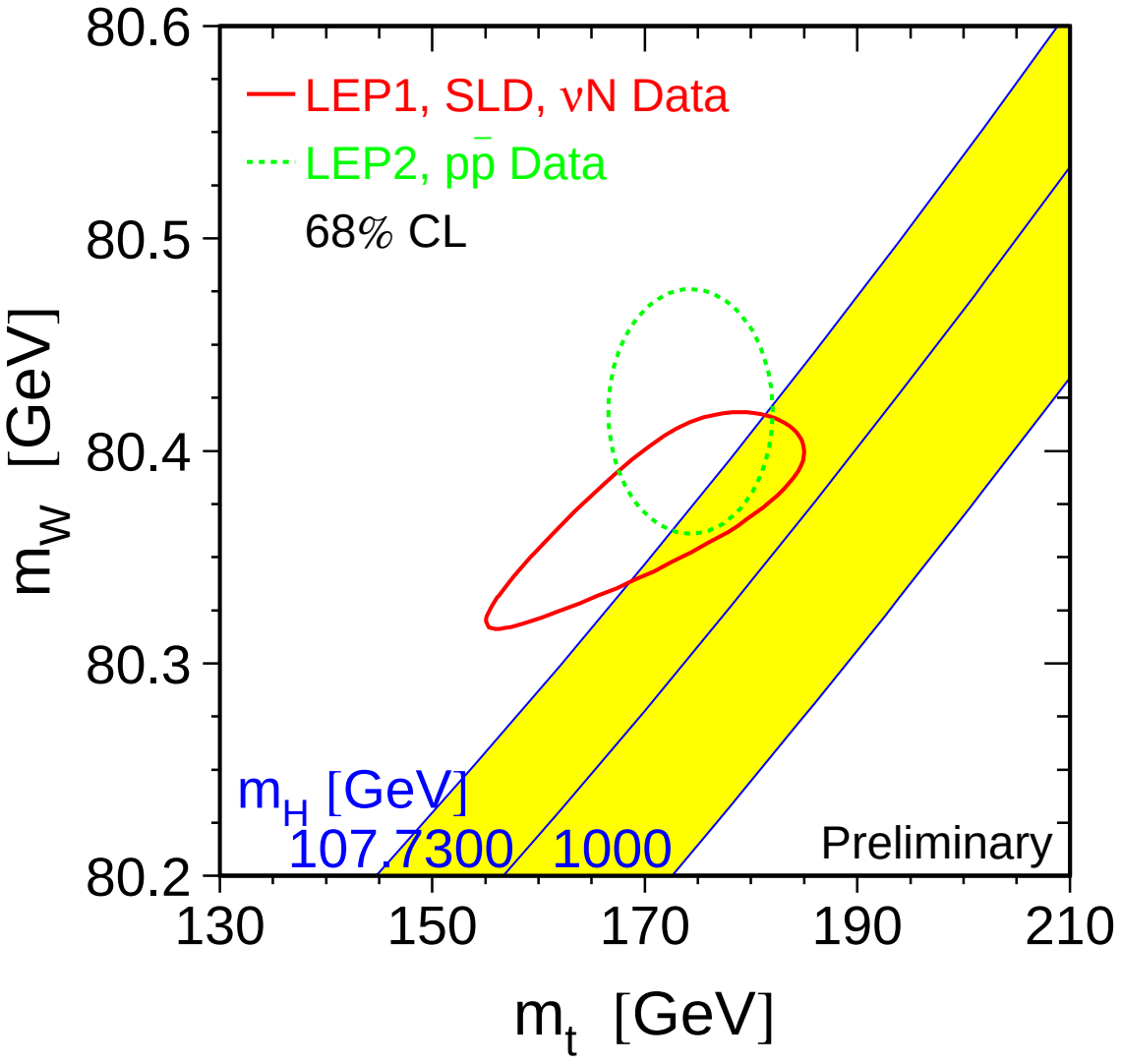

Figure 6.4: Implications of m_{t} and m_{W} for the SM Higgs mass. The red (solid) curve shows the 68% CL contour for m_{t} and m_{W} obtained indirectly from precision measurements from LEP1, SLD, and neutrino-scattering experiments. The green (dotted) curve is obtained from direct measurements of m_{t} and m_{W} at the TeVatron and LEP2. The shaded area shows the region of the (m_{t}, m_{W}) plane allowed for varying SM Higgs masses.

APPENDIX A
THE LB B-TAGGER

As discussed in Chapter 1, the dominant decay mode for Higgs bosons in the LEP2 mass range of interest is $H^0 \to b\bar{b}$. Therefore the ability to identify b-quark jets with high efficiency and purity is one of the most important ingredients of a Higgs search. There are three general characteristics of B hadron decay that can be exploited to tag the presence of a b quark:

1. B hadrons have a relatively long lifetime (~ 1.5 ps); therefore, with the excellent tracking resolution provided by the silicon microvertex detector (Section 2.2.1), one can look for secondary vertices significantly displaced from the primary vertex, or for tracks with large impact parameters with respect to the primary vertex.

2. When the B decays semileptonically, the presence of a charged lepton with large p_T with respect to the jet can be used to tag the b.

3. The kinematics of b jets provides some discrimination against light-quark jets; for example, the particle multiplicity of a b jet is generally larger.

To tag b's as efficiently as possible, OPAL makes use of all three of these tagging strategies. Since they are to a good approximation uncorrelated, they are combined using an unbinned relative likelihood into one variable that corresponds to the "b-ness" of a given jet. Figure A.1 shows a schematic of the algorithm, known as LB (for **L**EP2 **B**-tagger).

Before discussing the three ingredients of the b-tagger it is worth noting that the algorithm was developed using jets from Z^0 calibration data taken at the beginning of 1998 and from equivalent simulated $Z^0 \to q\bar{q}$ decays. This provides a good source of both b jets and light-quark jets, and since the Higgs mass range under exploration

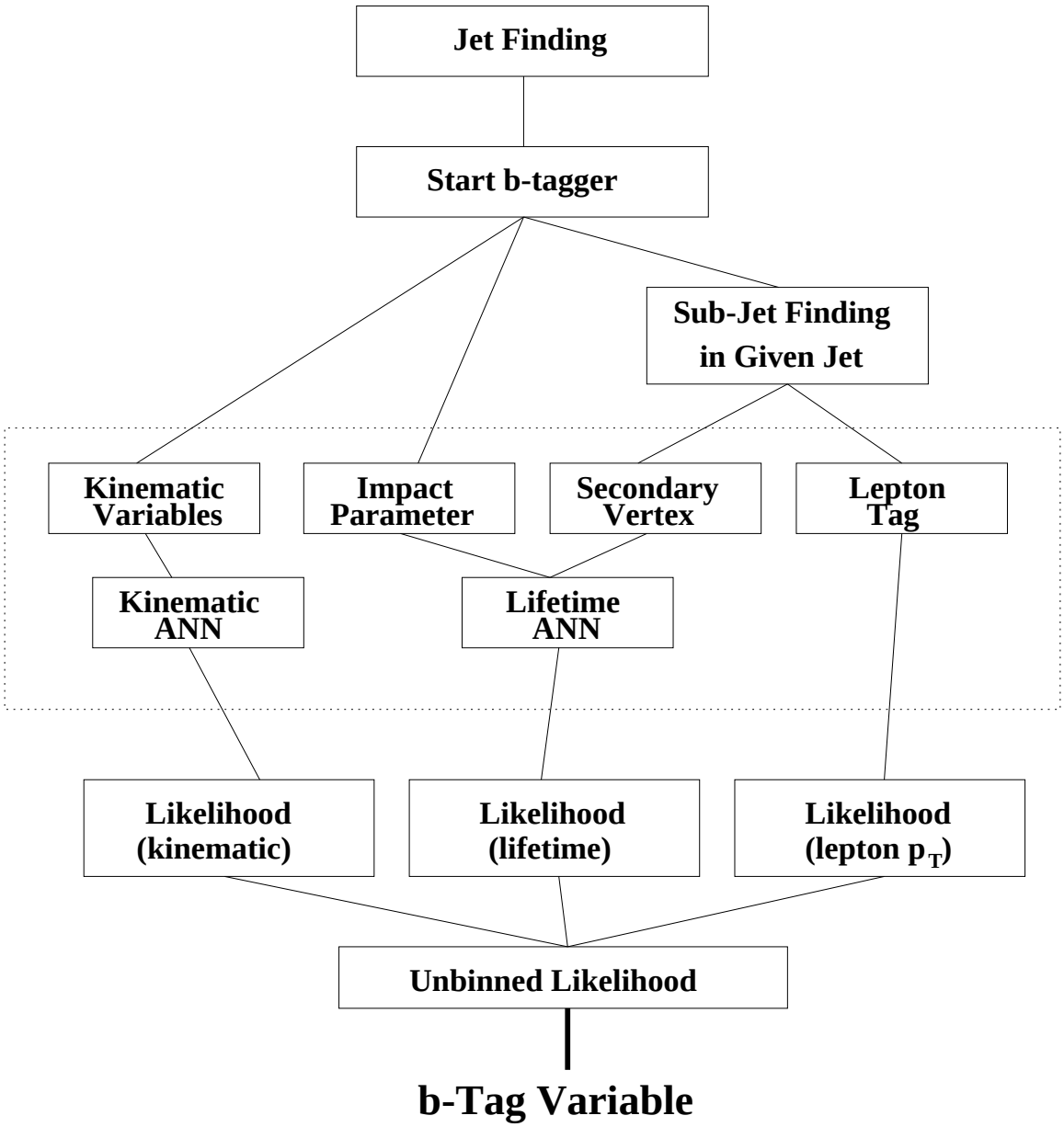

Figure A.1: Schematic of the LB b-tagger.

is similar to m_{Z}, the kinematics of the Z^0 jets will be kinematically similar to Higgs jets.

A.1 Lifetime Tagging

When forming a secondary vertex, one would like to avoid using fragmentation tracks from the primary vertex and instead only use the tracks from the B decay. To this end, a cone jet-finding algorithm [63] is used to find an energetic sub-jet within the original jet, to be associated with the actual B decay. The tracks in this sub-jet are then used to construct a secondary vertex, and the decay length L (the distance from the secondary vertex to the primary) and its error σ_L are used to define the decay length significance L/σ_L. The distributions of this variable for b, c, and light-quark (uds) jets are then used as p.d.f.'s for a likelihood calculation to arrive at a secondary vertex likelihood $\mathcal{L}_{\mathrm{SV}}$. Distributions of this variable are shown in Figure A.2a.

A powerful discriminant between b's and light quarks is the "reduced" decay length significance. This is a calculation of the decay length for the secondary vertex formed after removing the track with the largest impact parameter significance (b/σ_b). The reason this is useful is because when a significant decay length is found in a light-quark jet, it is usually due to one mismeasured track with large impact parameter. A secondary vertex from a true B decay should be stable upon removal of this track, whereas a light-quark vertex will not. Analogously to the calculation of $\mathcal{L}_{\mathrm{SV}}$, a reduced secondary vertex likelihood $\mathcal{R}_{\mathrm{SV}}$ is calculated from the distributions of the reduced decay length significance; the distribution of $\mathcal{R}_{\mathrm{SV}}$ is shown in Figure A.2b.

In order to recover some signal efficiency in the event that a good secondary vertex cannot be found, the impact parameter significances of the sub-jet tracks can be used provide lifetime information. Here, the distributions of impact parameter significances for b, c, and uds jets are again used as p.d.f.'s to form an impact parameter significance likelihood $\mathcal{L}_{\mathrm{IP}}$ for the jet. In addition, and for the same reasons as discussed above, a reduced impact parameter significance likelihood $\mathcal{R}_{\mathrm{IP}}$ is formed in the same manner as $\mathcal{R}_{\mathrm{SV}}$. Distributions of $\mathcal{L}_{\mathrm{IP}}$ and $\mathcal{R}_{\mathrm{IP}}$ are shown in Figure A.3.

The four variables $\mathcal{L}_{\mathrm{SV}}$, $\mathcal{R}_{\mathrm{SV}}$, $\mathcal{L}_{\mathrm{IP}}$, and $\mathcal{R}_{\mathrm{IP}}$ all have a high degree of discrimination

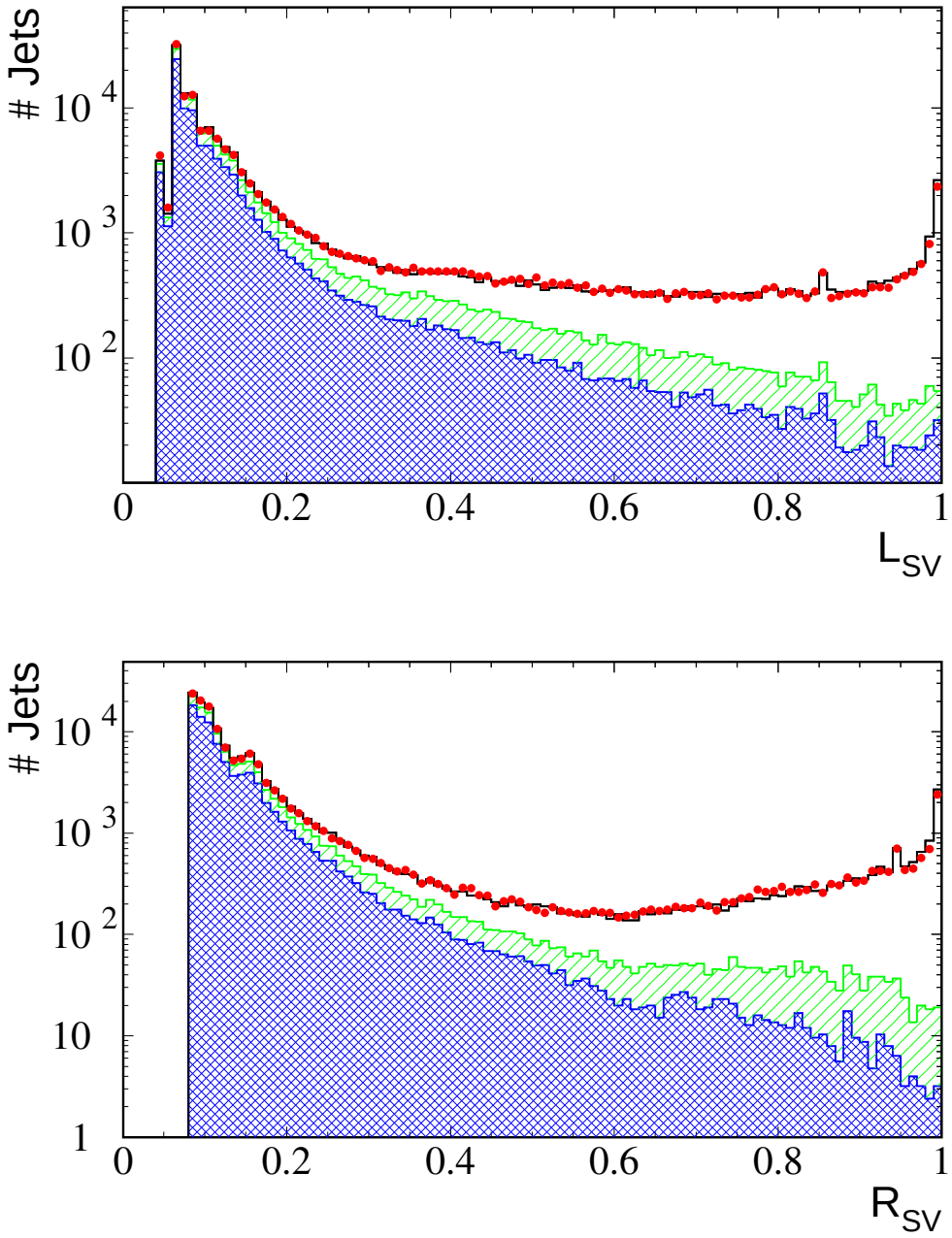

Figure A.2: Distributions of the secondary vertex likelihood (top plot) and the reduced secondary vertex likelihood (bottom plot) for uds jets (double-hatched histogram), c and uds jets (hatched histogram), and b, c, and uds jets (open histogram). The points are for real Z^0 decays.

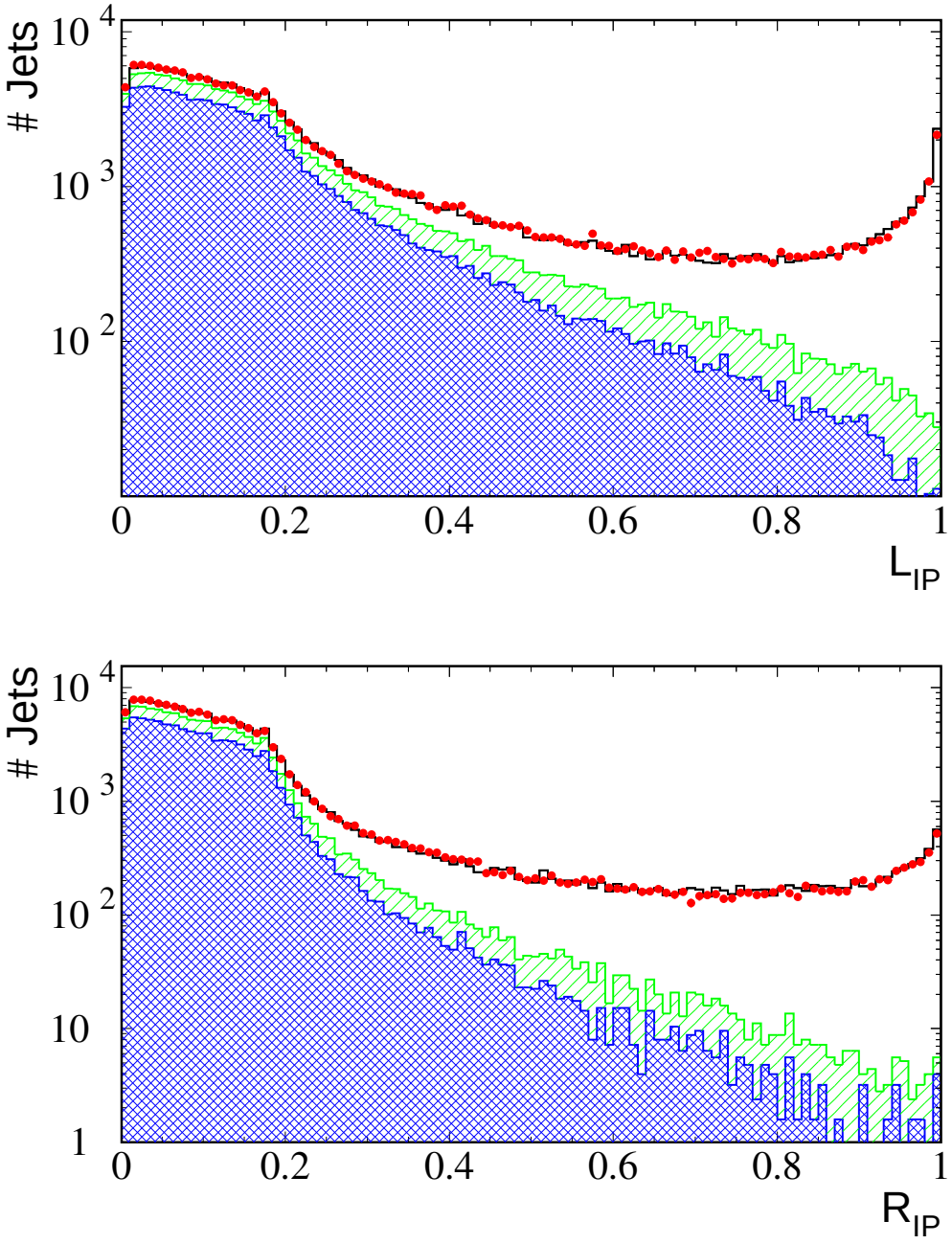

Figure A.3: Distributions of the impact parameter significance likelihood (top plot) and the reduced impact parameter significance likelihood (bottom plot) for uds jets (double-hatched histogram), c and uds jets (hatched histogram), and b, c, and uds jets (open histogram). The points are for real Z^0 decays.

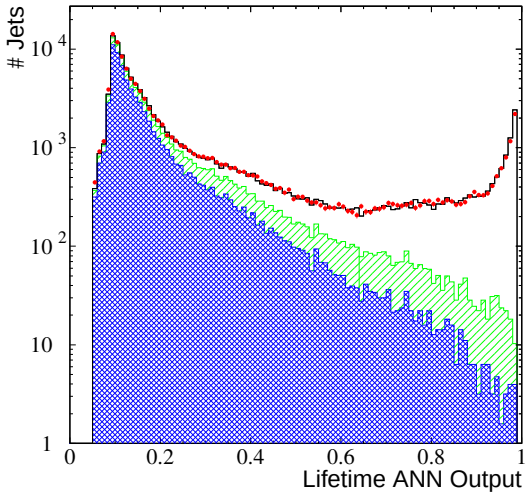

Figure A.4: Distributions of the lifetime ANN output for uds jets (double-hatched histogram), c and uds jets (hatched histogram), and b, c, and uds jets (open histogram). The points are for real Z^0 decays.

power, but they are also highly correlated. Therefore an ANN is used to combine them into one lifetime variable L_{ANN}, shown in Figure A.4.

A.2 High-p_T Lepton Tagging

Distributions of electron and muon p_T's with respect to the jet axis is shown in Figure A.5. Good discrimination power is seen, although the efficiency of this tag is limited by the B semileptonic branching ratio. The distributions of Figure A.5 are again used as p.d.f.'s for a calculation of a lepton p_T likelihood $\mathcal{L}_{\mathrm{lept}}$.

A.3 Kinematics Tagging

In and of themselves, jet kinematics are not an overwhelmingly discriminant b-tagger; however, their complementarity to the previous two tags provides a bit of extra sensitivity to b quarks. To form a kinematics tagger, three variables are input to an ANN:

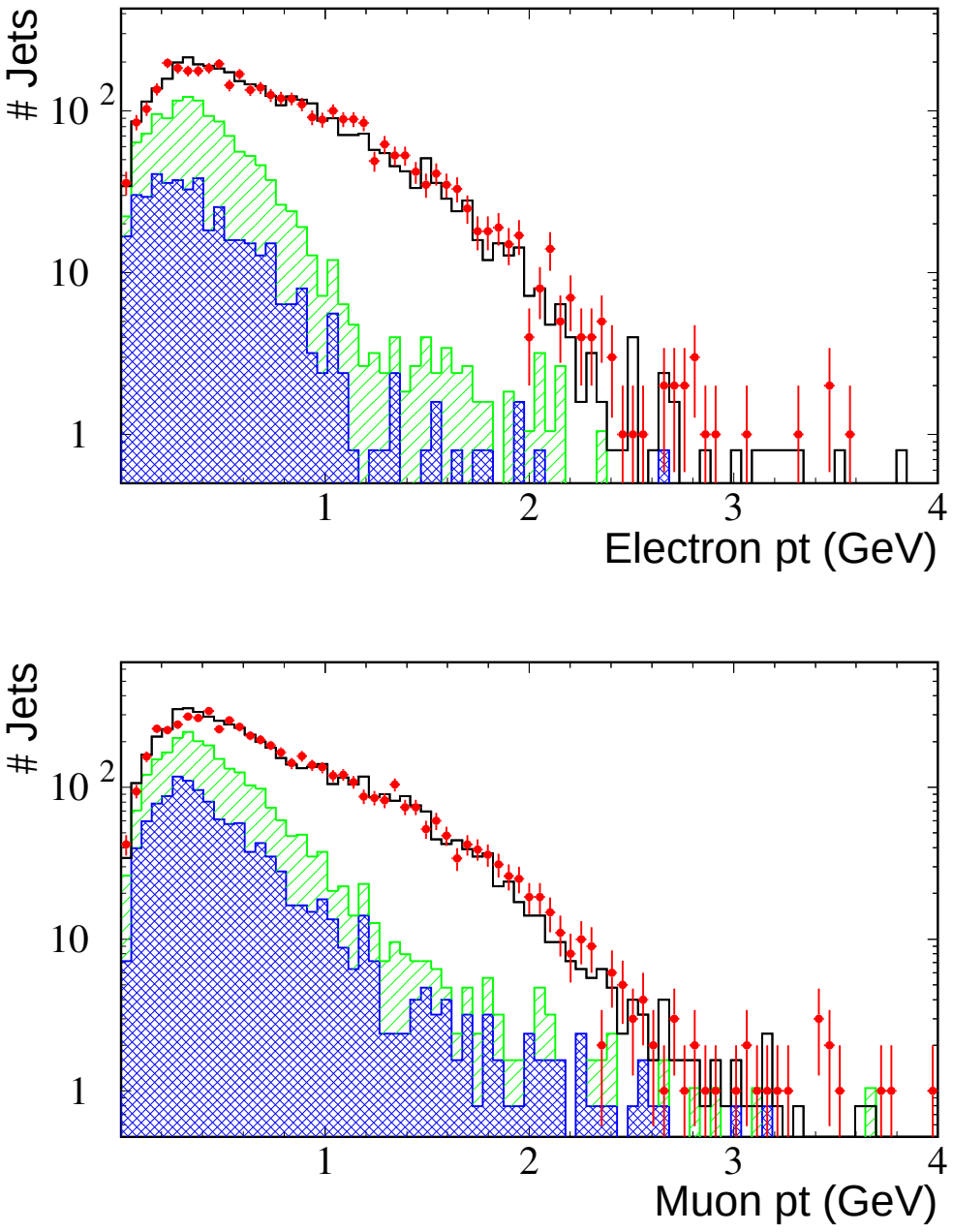

Figure A.5: Distributions of electron (top plot) and muon (bottom plot) p_T's for uds jets (double-hatched histogram), c and uds jets (hatched histogram), and b, c, and uds jets (open histogram). The points are for real Z^0 decays.

1. The number of particles in the sub-jet.

2. The angle between the sub-jet axis and the sub-jet boosted sphericity axis. The boosted sphericity axis is the boost direction that maximizes the sphericity of the sub-jet.

3. A jet-shape variable called the boosted C-parameter [64] calculated for the sub-jet.

The output of the ANN gives one discriminating variable K_{ANN}.

A.4 Combination of the Tags and Performance

As mentioned before, the three tagging variables L_{ANN}, $\mathcal{L}_{\mathrm{lept}}$, and K_{ANN} are essentially uncorrelated and can be combined using an unbinned relative likelihood method to form a final b-tagging discriminant $\mathcal{B}_{\mathrm{jet}}$, the distribution of which is shown in Figure A.6a along with an efficiency versus impurity curve for $\mathrm{Z}^0 \to \mathrm{q\bar{q}}$ decays. For reference, this b-tagger achieves 50% efficiency with an impurity of only 8%.

The price of this excellent performance is, as should be obvious, an extremely complex algorithm. To ensure the validity of the procedure, a number of cross-checks were done comparing real data to Monte Carlo. Some examples are listed below.

- **Comparison of jet tagging rates.** The fraction of jets tagged as a function of $\mathcal{B}_{\mathrm{jet}}$ was compared. This is shown in Figure A.6b; data and MC agree to about 2%.

- **Comparison of efficiencies with a double-tag method [45].** Using the fact that a b jet will be accompanied by a $\bar{\mathrm{b}}$ jet, one can extract an efficiency from real data independent of any MC prediction. Applying the same procedure to MC data and comparing efficiencies, 2–5% agreement is seen.

- **Semileptonic W pair decays.** To test the b-tagger on a sample enriched in non-b jets, the algorithm was applied to the jets in $\mathrm{W^+W^-} \to \mathrm{q\bar{q}'}\ell\nu_\ell$ events. No discrepancy was seen within the 5–10% statistical precision of this test.

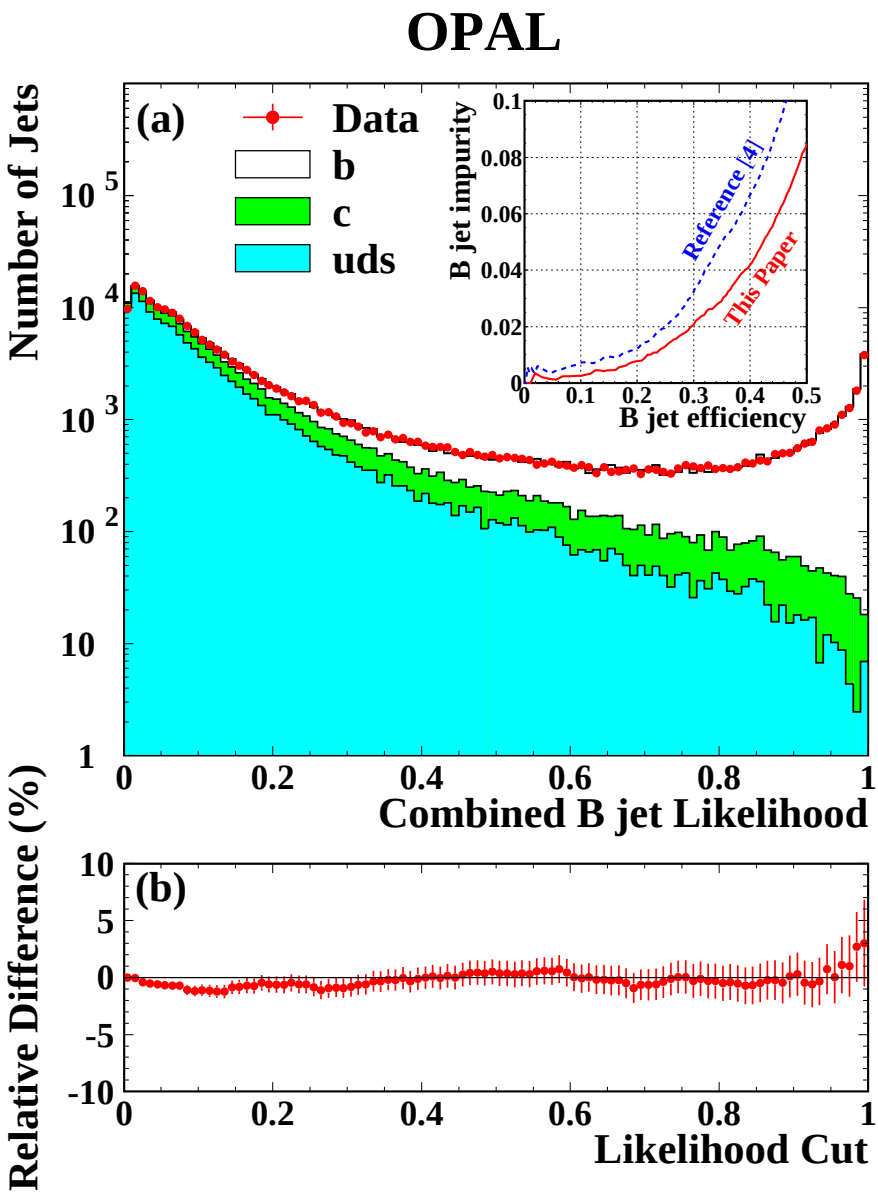

Figure A.6: Performance of the LB b-tagger (taken from [49]). In (a) the distribution of $\mathcal{B}_{\text{jet}}$ is shown for jets from real and simulated Z^0 decays. The inset shows the efficiency versus impurity curve for LB and for a previous b-tagging algorithm (Reference [4] in the inset corresponds to [48] in this thesis). In (b) the relative difference between the tagging rates observed in data and MC is shown as a function of the cut on $\mathcal{B}_{\text{jet}}$ for Z^0 decays (the plotted values are correlated point to point).

In the end, the variable used in the $\mathcal{L}_{b\bar{b}\tau^+\tau^-}$ likelihood described in Section 4.1.5 is a combination of the b-tags for the two jets:

$$\mathcal{B}_{2\text{jet}} = \frac{\mathcal{B}_1\mathcal{B}_2}{\mathcal{B}_1\mathcal{B}_2 + (1-\mathcal{B}_1)(1-\mathcal{B}_2)} \tag{A.1}$$

This is shown in Figure 4.11 with the transformation $1 - \sqrt{1-x}$ applied.

APPENDIX B
THE IMPACT PARAMETER JOINT PROBABILITY TAG

As discussed in Appendix A.1, using impact parameters to tag lifetime provides an alternative to secondary-vertexing methods. The joint probability tag discussed here was developed for use as a b-tagger; discussion of its application to taus will be postponed until the end.

The tag is based on a track's $r-\phi$ impact parameter with respect to the primary vertex b, divided by its error σ_b, and signed with respect to the nearest jet axis.[1] Tracks with $b/\sigma_b < 0$ ("backward" tracks) are assumed to come from the primary vertex, *i.e.* their non-zero significances are purely the result of detector resolution and contain no lifetime information. Thus the distribution of negative impact parameter significances provides an estimate of the detector resolution function $f(x)$. The resolution function is used to weight forward tracks according to their impact parameter significances; the probability that a track i from the primary vertex would have a significance greater than or equal to its observed b/σ_b is

$$P_i = \frac{\int_{b/\sigma_b}^{\infty} f(x)\,dx}{\int_0^{\infty} f(x)\,dx} \tag{B.1}$$

If y is the product of the P_i's for some ensemble of N tracks, then the joint probability P_J that the ensemble comes from the primary vertex is the integral over the volume of the N-dimensional unit hypercube in P_i space for which $y < y_{\rm obs}$:

$$P_J = y_{\rm obs} \sum_{m=0}^{N-1} \frac{(-\ln y_{\rm obs})^m}{m!} \tag{B.2}$$

[1]The signing is done as follows. Let $\hat{\jmath}$ be the vector passing through the primary vertex and parallel to the jet direction, and $\hat{k}$ be the vector from the primary vertex to the point of closest approach on the track trajectory. The sign of b is then the sign of $\hat{\jmath}\cdot\hat{k}$.

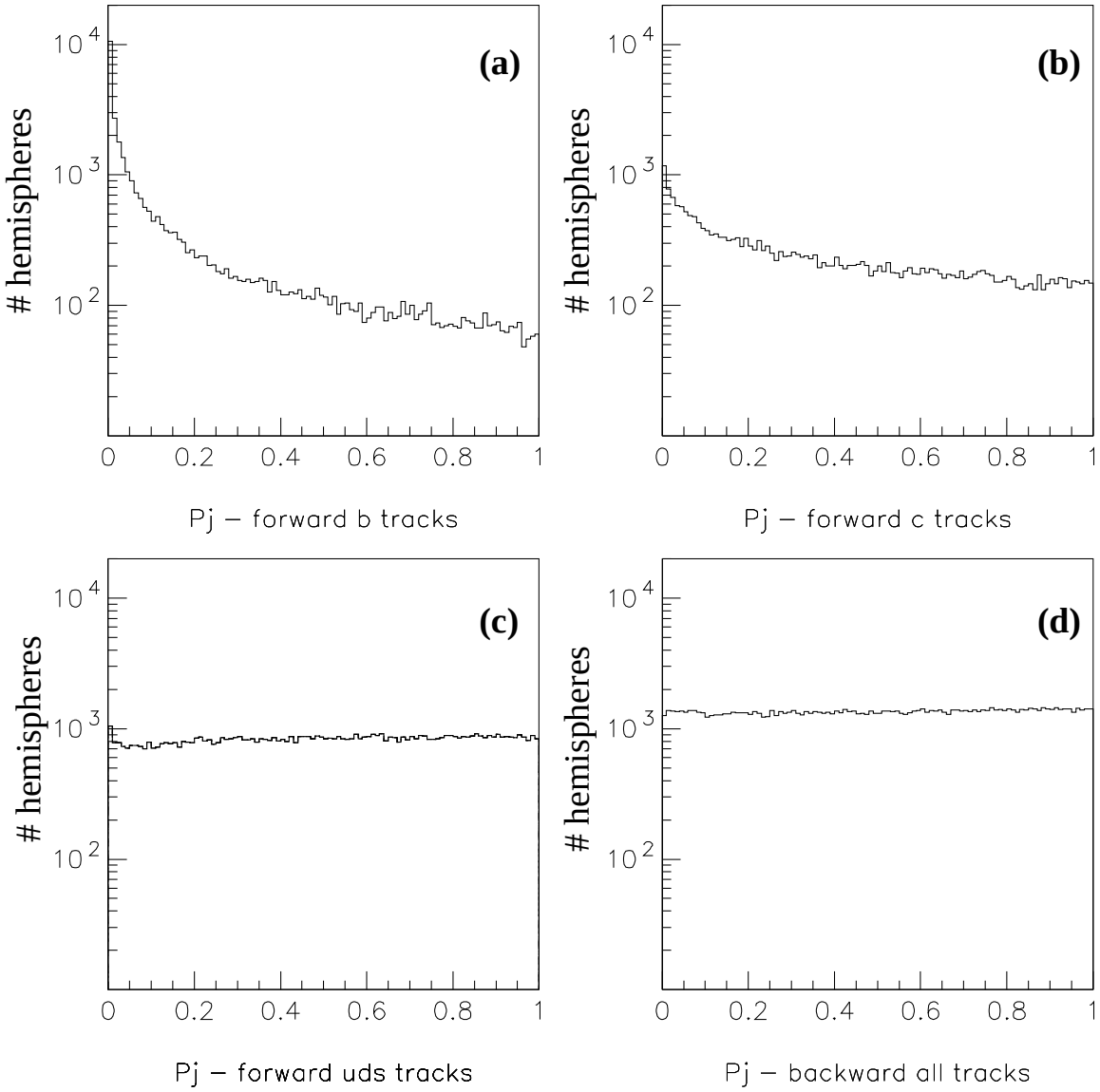

Figure B.1: Distributions of P_J for forward tracks in Z^0 hemispheres containing (a) b quarks, (b) c quarks, and (c) light quarks, and for (d) backward tracks (any flavor).

Ensembles of tracks containing lifetime information will tend to pile up at low values of P_J, whereas ensembles from the primary vertex will have a flat P_J distribution by construction. This is shown in Figure B.1, where the P_J's for the forward tracks in $Z^0 \to q\bar{q}$ thrust hemispheres are shown for $b\bar{b}$, $c\bar{c}$, and light-quark events, as well as for backward tracks of any flavor.

The detector resolution function was determined using backward tracks taken from Z^0 calibration data taken at the beginning of 1998. A good parameterization of the resolution function was found to be

$$f(x) = C_1 e^{-\frac{x^2}{2C_2^2}} + C_3 e^{-\frac{x}{C_4}} + C_5 e^{-\frac{x}{C_6}} + C_7 e^{-\frac{x}{C_8}} \tag{B.3}$$

where $x = |b/\sigma_b|$ and the C_i's are fit parameters. Resolution functions were determined for data and Monte Carlo, and independently for tracks with one SI hit and two SI hits. An example is shown in Figure B.2. The P_J distribution for backward tracks from 189 GeV events passing the pre-likelihood cuts of Section 4.1 is shown in Figure B.3, indicating that Equation B.3 models the detector resolution adequately.

Exploiting the tau lifetime is in principle a good way to separate real taus from

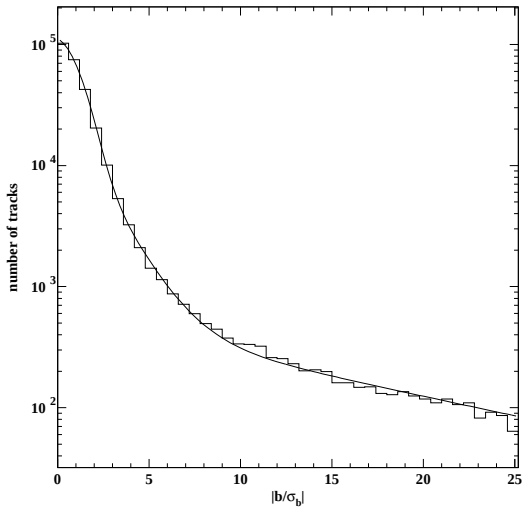

Figure B.2: Equation B.3 (curve) fitted to the distribution of $|b/\sigma_b|$ for backward tracks with 2 SI hits from 1998 Z^0 calibration data (histogram).

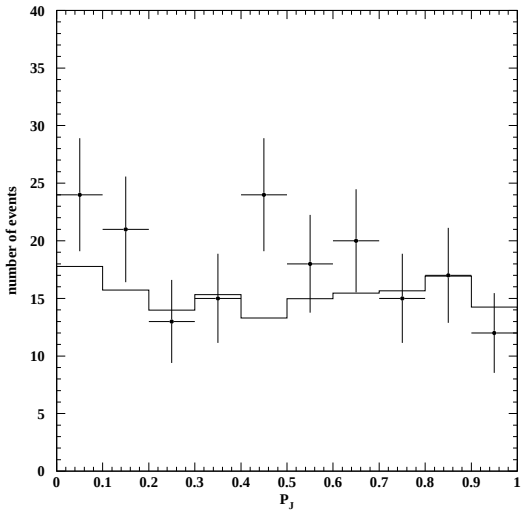

Figure B.3: Distribution of P_J for backward tracks from 189 GeV events passing the pre-likelihood selection of Section 4.1. The points are data, the histogram is MC.

both prompt electrons and muons and hadronic fake taus from jet fragmentation tracks, as tracks from these two background sources come from the primary vertex. For three-prong taus one could imagine trying to form a secondary vertex from the three tracks, however this is very difficult due to the high boost of the tracks. This leads one to consider impact parameter methods. Since the tau lifetime is only about 20% that of the average B hadron, one does not expect tau decay tracks to have very large impact parameters; however, for a tau *pair*, the ensemble approach of the joint probability tag allows both taus to contribute their lifetime information collectively. This makes this tag well-suited for purifying a tau-pair sample, as can be seen in Figure B.4, where P_J is shown for the tau pairs found in $h^0A^0 \to b\bar{b}\tau^+\tau^-$ events along with the "tau pairs" found in SM background events. The real tau pairs, containing lifetime information, peak up at $P_J = 0$ much more strongly than the background, thus motivating its inclusion in the likelihoods of Chapter 4.[2]

[2]In the actual likelihoods, the variable $\sqrt{P_J}$ is used in order to expand the sensitive region of the distribution.

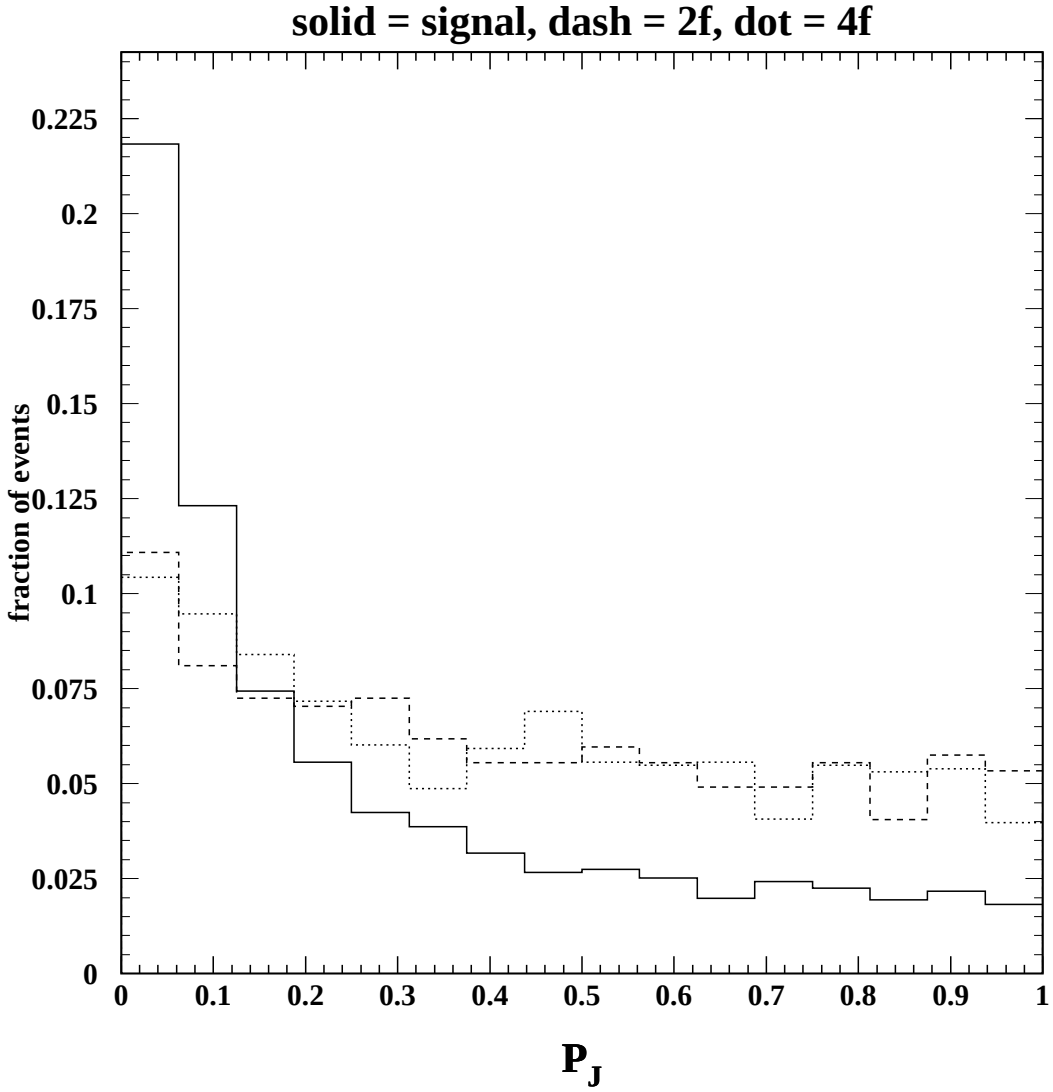

Figure B.4: Distribution of P_J for the tau pairs found in h^0A^0 signal events (solid), two-fermion background events (dashed) and four-fermion background events (dotted).

REFERENCES

[1] S. Glashow, *Nucl. Phys.* **22** (1961) 579.

[2] S. Weinberg, *Phys. Rev. Lett.* **19** (1967) 1264.

[3] A. Salam, *Elementary Particle Theory*, N. Svartholm, ed., Almquist and Wiksells, Stockholm (1968), 367.

[4] F.J. Hasert *et al.*, *Phys. Lett.*, **B46** (1973) 138.

[5] UA1 Collaboration, G. Arnison *et al.*, *Phys. Lett.*, **B122** (1983) 103.

[6] UA2 Collaboration, M. Banner *et al.*, *Phys. Lett.*, **B122** (1983) 476.

[7] UA1 Collaboration, G. Arnison *et al.*, *Phys. Lett.*, **B126** (1983) 398.

[8] UA2 Collaboration, P. Bagnaia *et al.*, *Phys. Lett.*, **B129** (1983) 130.

[9] P.W. Higgs, *Phys. Lett.* **12** (1964) 132.

[10] J.F. Gunion, H.E. Haber, G. Kane and S. Dawson, *The Higgs Hunter's Guide*, Addison-Wesley Publishing Company, Reading, MA (1990).

[11] M. Quirós, "Constraints on the Higgs Boson Properties from the Effective Potential," to appear in *Perspectives on Higgs Physics II*, G.L. Kane, ed., World Scientific.

[12] S. Glashow and S. Weinberg, *Phys. Rev.* **D15** (1977) 1958.

[13] M. Carena, M. Quirós, and C.E.M. Wagner, *Nucl. Phys.* **B461** (1996) 407.

[14] H. Haber, R. Hempfling, and A. Hoang, *Z. Phys* **C75** (1997) 539.

[15] R. Hempfling and A. Hoang, *Phys. Lett.* **B331** (1994) 99.

[16] R.-J. Zhang, *Phys. Lett.* **B447** (1999) 89.

[17] S. Heinemeyer, W. Hollik, and G. Weiglein, *Phys. Lett.* **B440** (1998) 296.

[18] S. Heinemeyer, W. Hollik, and G. Weiglein, *Eur. Phys. J.* **C9** (1999) 343.

[19] M. Carena, H.E. Haber, S. Heinemeyer, W. Hollik, C.E.M. Wagner, and G. Weiglein, *Nucl. Phys.* **B580** (2000) 29.

[20] E. Accomando *et al.*, *Higgs Physics* in *Physics at LEP2*, CERN 96-01, Vol. 1, (1996) 351.

[21] S. Myers and E. Picasso, *Sci. Am.* **263** (1990) 34.

[22] OPAL Collaboration, K. Ahmet *et al.*, *Nucl. Instr. and Meth.* **A305** (1991) 275.

[23] S. Anderson *et al.*, *Nucl. Instr. and Meth.* **A403** (1998) 326.

[24] P.P. Allport *et al.*, *Nucl. Instr. and Meth.* **A310** (1991) 155.

[25] T. Sjöstrand, *Comp. Phys. Comm.* **82** (1994) 74.

[26] S. Jadach, W. Płaczek, and B.F.L. Ward, *Physics at LEP2*, CERN 96-01, Vol. 2, 286.

[27] S. Jadach, B.F.L. Ward, and Z. Wąs, *Comp. Phys. Comm.* **79** (1994) 503.

[28] J. Fujimoto *et al.*, *Comp. Phys. Comm.* **100** (1997) 128.

[29] R. Engel and J. Ranft, *Phys. Rev.* **D54** (1996) 4244.

[30] G. Marchesini *et al.*, *Comp. Phys. Comm.* **67** (1992) 465.

[31] J.A.M. Vermaseren, *Nucl. Phys.* **B229** (1983) 347.

[32] OPAL Collaboration, G. Alexander *et al.*, *Z. Phys.* **C69** (1996) 543.

[33] F.A. Berends, R. Pittau, and R. Kleiss, *Comp. Phys. Comm.* **85** (1995) 437.

[34] P. Janot, *Physics at LEP2*, CERN 96-01, Vol. 2, 309.

[35] J. Allison *et al.*, *Nucl. Instr. and Meth.* **A317** (1992) 47.

[36] D.E. Groom *et al.*, *Eur. Phys. J.* **C15** (2000) 1.

[37] C. Peterson and T. Rögnvaldsson, "An Introduction to Artificial Neural Networks," *1991 CERN School of Computing*, CERN 92-02, 113.

[38] OPAL Collaboration, K. Ackerstaff *et al.*, *Eur. Phys. J.* **C2** (1998) 213.

[39] C. Baily, R. Coxe, D. Glenzinski, "$WW \to \tau\nu q\bar{q}$ Event Selection at $\sqrt{s} = 161$ GeV," OPAL TN393.

[40] L. Lönnblad, C. Peterson, and T. Rögnvaldsson, *Comp. Phys. Comm.* **81** (1994) 185.

[41] OPAL Collaboration, K. Ackerstaff *et al.*, *Phys. Lett.* **B389** (1996) 416.

[42] S. Bethke, Z. Kunszt, D. Soper and W.J. Stirling, *Nucl. Phys.* **B370** (1992) 310.

[43] OPAL Collaboration, G. Abbiendi *et al.*, *Phys. Lett.* **B453** (1999) 138.

[44] OPAL Collaboration, G. Alexander *et al.*, *Z. Phys.* **C52** (1991) 175.

[45] OPAL Collaboration, G. Abbiendi *et al.*, *Eur. Phys. J.* **C8** (1999) 217.

[46] R.M. Barnett *et al.*, *Phys. Rev.* **D54** (1996) 1.

[47] LEP Heavy Flavour Working Group, D. Abbaneo *et al.*, "Input Parameters for the LEP/SLD Heavy Flavour Results for Summer 1998 Conferences", LEPHF/98-01.

[48] OPAL Collaboration, G. Abbiendi *et al.*, *Eur. Phys. J.* **C7** (1999) 407.

[49] OPAL Collaboration, G. Abbiendi *et al.*, *Eur. Phys. J.* **C12** (2000) 567.

[50] OPAL Collaboration, K. Ackerstaff *et al.*, *Eur. Phys. J.* **C1** (1998) 425.

[51] OPAL Collaboration, K. Ackerstaff *et al.*, *Eur. Phys. J.* **C5** (1998) 19.

[52] OPAL Collaboration, G. Alexander *et al.*, *Z. Phys.* **C73** (1997) 189.

[53] P. Bock, "Determination of exclusion limits for particle production using different decay channels with different efficiencies, mass resolutions and backgrounds," Heidelberg Institute Preprint HD-PY96-05 (1996).

[54] R.D. Cousins and V.L. Highland, *Nucl. Instr. and. Meth.* **A320** (1992) 331.

[55] K. Tollefson and E.W. Varnes, *Annu. Rev. Nucl. Part. Sci.* (1999) 49.

[56] S. Katsanevas and S. Melachroinos, *Physics at LEP2*, CERN 96-01, Vol. 2, 328.

[57] OPAL Collaboration, K. Ackerstaff *et al.*, *Z. Phys.* **C75** (1997) 409.

[58] OPAL Collaboration, G. Abbiendi *et al.*, *Eur. Phys. J.* **C8** (1999) 255.

[59] J.M. Frère, D.R.T. Jones and S. Raby, *Nucl. Phys.* **B222** (1983) 11.

[60] A. Kusenko, P. Langacker, and G. Segrè, *Phys. Rev.* **D54** (1996) 5824.

[61] OPAL Collaboration, G. Abbiendi *et al.*, "Two Higgs Doublet Model and Model Independent Interpretations of Neutral Higgs Boson Searches," submitted to *Eur. Phys. J.*, CERN-EP-2000-092.

[62] OPAL Collaboration, P.D. Acton *et al.*, *Phys. Lett.* **B268** (1991) 122.

[63] L. del Pozo, "Jet Finding with a Cone Algorithm," OPAL TN170.

[64] J.F. Donoghue, F.E. Low, and S.Y. Pi, *Phys. Rev.* **D20** (1979) 2759.